

Charles University in Prague
Faculty of Mathematics and Physics

DOCTORAL THESIS



Mgr. Mykhailo Vorokhta

Investigation of magnetron sputtered Pt-CeO₂ thin film catalyst for fuel cell applications

Department of Surface and Plasma Science

Supervisor of the doctoral thesis: Prof. RNDr. Vladimír Matolín, DrSc.

Prague 2013

Acknowledgements

Here I would like to mention people who help me with this doctoral thesis. First of all I want to express my sincere appreciation and respect to my supervisor prof. RNDr. Vladimír Matolín, DrSc. who has guided me for research work and always made himself available to offer advice and constructive comments. Under his supervision our surface science group became one of the best groups in Czech Republic that gave me opportunity to work with highly qualified staff, and access to modern facilities.

I also would like to thank RNDr. Kateřině Veltruské, CSc. who has been always ready to help me with many technical and scientific problems during measurements. Further thanks to doc. Mgr. Iva Matolínová, Dr. who helped me with measuring at synchrotron Spring 8 and with data processing and to Ing. Natalie Tsud, PhD for her careful reading of the thesis.

Many thanks to my colleagues PhD students especially Mgr. Ivan Khalakhan and Mgr. Michal Vaclavů who always help me in solving of different problems connected with acquisition and processing of the data. Other persons who have helped me but whose names are not mentioned on this page I am thankful to all of you too.

Dedication

I would like to dedicate this thesis to my parents and to my wife Svitlana. I am deeply grateful to my parents for their support throughout the years of my study. Thanks to my wife who let me go study abroad and waited for our marriage almost 3 years. Your support always inspired me to work hard and finish this doctoral work in time.

I declare that I carried out this doctoral thesis independently, and only with the cited sources, literature and other professional sources.

I understand that my work relates to the rights and obligations under the Act No. 121/2000 Coll., the Copyright Act, as amended, in particular the fact that the Charles University in Prague has the right to conclude a license agreement on the use of this work as a school work pursuant to Section 60 paragraph 1 of the Copyright Act.

In..... date.....

signature

Název práce: *Studium katalyzátorů Pt-CeO₂ připravených magnetronovým naprašováním.*

Autor: *Mgr. Mykhailo Vorokhta*

Katedra / Ústav: *Katedra fyziky povrchů a plazmatu*

Vedoucí doktorské práce: *Prof. RNDr. Vladimír Matolín, DrSc.
matolin@mbox.troja.mff.cuni.cz*

Abstrakt:

Doktorská práce se zabývá studiem Pt dopovaných tenkých vrstev CeO₂ připravených magnetronovým naprašováním, u kterých bylo zjištěno, že představují velice aktivní katalyzátor pro palivové články s proton-vodivou membránou (PEMFC). Tenké vrstvy Pt-CeO₂ byly naprašovány na různé substráty (křemíkové a uhlíkové substráty, uhlíkové nanotrubky) a byly zkoumány převážně pomocí fotoelektronové spektroskopie buzené tvrdým rentgenovým zářením (HAXPES). Výsledky získané metodou HAXPES ukázaly, že příprava katalytických vrstev oxidu ceru dopovaných Pt na různých uhlíkových substrátech a nanotrubkách metodou magnetronového naprašování vede k růstu vysoce porézních vrstev Pt-Ce-O s platinou v iontovém stavu Pt²⁺, Pt⁴⁺. Získané výsledky také ukázaly, že mechanismus růstu vrstvy Pt-CeO₂ je silně ovlivněn interakcí atomů Ce se substrátem a jejich oxidací v kyslíkovém plazmatu. Vznik Ptⁿ⁺ stavů společně s porézním charakterem katalytických vrstev slouží k vysvětlení vysoké aktivity katalyzátorů na bázi Pt-CeO₂ pro palivové články PEMFCs.

Klíčová slova: *magnetronové naprašování, oxid ceru, Pt, XPS, SRPES.*

Title: *Investigation of magnetron sputtered Pt-CeO₂ thin film catalyst for fuel cell applications.*

Author: *Mgr. Mykhailo Vorokhta*

Department: *Department of Surface and Plasma Science*

Supervisor: *Prof. RNDr. Vladimír Matolín, DrSc.
matolin@mbox.troja.mff.cuni.cz*

Abstract:

This doctoral thesis focuses on magnetron sputtered Pt-doped CeO₂ thin films that were found to be very active catalysts in proton exchange membrane fuel cells (PEMFC). The films were prepared on different substrates (silicon wafers, carbon nanotubes and flat carbon substrates) and investigated mainly by means of Hard x-ray photoelectron spectroscopy (HAXPES). The HAXPES method showed that deposition of the Pt doped cerium oxide catalyst layers on carbon nanotubes and flat carbon substrates by magnetron sputtering leads to growth of a highly porous “Pt-Ce-O” solid solution film, where platinum is mostly in ionic states, Pt²⁺, Pt⁴⁺. The results obtained showed that the mechanism of film growth is strongly influenced by interaction of the Ce atoms with the substrate and their oxidation by oxygen containing RF plasma. The formation of Ptⁿ⁺ states together with the porous character of the catalyst films are used to explain the high activity of Pt-CeO₂ catalyst in PEMFCs.

Keywords: *magnetron sputtering, cerium oxide, Pt, XPS, SRPES.*

Preface

The presented thesis is based on experimental work that was already published or will be published soon in the following scientific papers:

1. V. Matolín, I. Matolínová, M. Vaclavů, I. Khalakhan, M. Vorokhta, R. Fiala, I. Pis, Z. Sofer, J. Poltieroová-Vejpravová, T. Mori, V. Potin, H. Yoshikawa, S. Ueda, K. Kobayashi: Platinum-Doped CeO₂ Thin Film Catalysts Prepared by Magnetron Sputtering. *Langmuir* 26 (15) (2010) 12824-12831.
2. Matolínová, R. Fiala, I. Khalakhan, M. Vorokhta, Z. Sofer, H. Yoshikawa, K. Kobayashi, V. Matolín: Synchrotron radiation photoelectron spectroscopy study of metal-oxide thin film catalysts: Pt–CeO₂ coated CNTs, *Appl. Surf. Sci.*, 258 (2012) 2161-2164
3. V. Matolín, R. Fiala, I. Khalakhan, J. Lavkova, M. Vaclavů, M. Vorokhta: Nanoporous Ptⁿ⁺–CeO_x catalyst films grown on carbon substrates. *Int. J. Nanotechnol.* 9 (8/9) (2012) 680-694.
4. M. Vorokhta, I. Khalakhan, I. Matolínová., M. Kobata, H. Yoshikawa, K. Kobayashi, V. Matolín: Nanostructured Pt-CeO₂ thin film catalyst grown on graphite foil by magnetron sputtering, *Appl. Surf. Sci.* 267 (2013) 119-123.
5. M. Vorokhta, I. Matolínová, M. Dubau, S. Haviar, I. Khalakhan, K. Ševčíková, T. Mori, H. Yoshikawa, V. Matolín: Interaction of sputter deposited CeO_x thin films with silicon oxide substrate, will be submitted (2013).

The following is a list of papers in which Mgr. Mykhailo Vorokhta is a co-author:

6. V. Stetsovych, F. Pagliuca, F. Dvořák, T. Duchoň, M. Vorokhta, M. Aulická, J. Lachnitt, S. Schernich, I. Matolínová, K. Veltruská, T. Skála, D. Mazur, J. Mysliveček, J. Libuda, V. Matolín: Epitaxial cubic Ce₂O₃ films via Ce-CeO₂ interfacial reaction, *J. Phys. Chem. Lett.*, 4 (6) (2013) 866-871.
7. S. Bruyère, A. Cacucci, V. Potin, I. Matolínová, M. Vorokhta, V. Matolín: Deposition of Pt and Sn doped CeO_x layers on silicon substrate, *Surf. Coat. Technol.*, In press (2013).
8. I. Khalakhan, M. Dubau, S. Haviar, J. Lavková, I. Matolínová, V. Potin, M. Vorokhta, V. Matolín: Growth of nano-porous Pt-doped cerium oxide thin films on glassy carbon substrate, *Ceram. Intern.*, 39 (2013) 3765-3769.
9. I. Khalakhan, M. Vorokhta, M. Chundak and V. Matolín: Au-CeO₂ nanoporous films/carbon nanotubes composites prepared by magnetron sputtering, *Appl. Surf. Sci.* 267 (2013) 150-153.
10. S. Haviar, M. Dubau, I. Khalakhan, M. Vorokhta, I. Matolínová, V. Matolín, V. Valeš, J. Endres, V. Holý, M. Buljan and S. Bernstorff: X-ray small-angle scattering from sputtered CeO₂/C bilayers, *J. Appl. Phys.*, 113 (2013) 024301 (1-7).
11. P. Studenyak, M. Kranjčec, V. Yu. Izai, A.A. Chomolyak, M. Vorokhta, V. Matolín, C. Cserhati, S. Kökényesi: Structural and temperature-related disordering studies of Cu₆PS₅I amorphous thin films, *Thin Solid Films*, 520 (2012) 1729-1733.
12. Y. Lykhach, T. Staudt, M. Vorokhta, T. Skála, V. Johánek, K.C. Prince, V. Matolín, J. Libuda: Hydrogen spillover monitored by resonant photoemission spectroscopy, *J. Catal.* 285 (2012) 6-9.
13. R. Fiala, I. Khalakhan, I. Matolínová, M. Vaclavů, M. Vorokhta, Z. Sofer, S. Huber, V. Potin, V. Matolín: Pt-CeO₂ Coating of Carbon Nanotubes Grown on Anode Gas Diffusion Layer of the Polymer Electrolyte Membrane Fuel Cell, *J. Nanosci. Nanotechnol.* 11 (2011) 5062–5067.

14. I. Matolínová, V. Johánek, J. Mysliveček, K.C. Prince, T. Skála, M. Skoda, N. Tsud, M. Vorokhta, V. Matolín: CO and methanol adsorption on (2x1) Pt(110) and ion-eroded Pt(111) model catalysts, *Surf. Interface Anal.*, 43 (10) (2011) 1325-1331.
15. V. Matolín, I. Khalakhan, I. Matolínová, M. Vaclavů, K. Veltruska, M. Vorokhta: Pt^{2+,4+} ions in CeO₂ rf-sputtered thin films, *Surf. Interface Anal.* 42 (6-7) (2010) 882-885.

Contents

1. Introduction.....	1
1.1. Motivation.....	1
1.2. Goals, objectives and structure of the thesis.....	2
2. Background.....	4
2.1. Polymer Electrolyte Membrane Fuel Cell (PEMFC).....	4
2.1.1. Work principle of PEMFC.....	4
2.1.2. Types of PEMFC	5
2.1.3. Carbon nanotubes in PEMFC.....	6
2.2. Catalysts for fuel cells.....	7
2.2.1. CeO_2 as a catalyst and catalyst support.....	8
2.2.2. $Pt-CeO_2$ as catalyst for fuel cell applications.....	9
2.2.3. CeO_2 and Ce_2O_3 studied by core-level photoelectron spectroscopy.....	10
3. Theoretical description of the used experimental techniques.....	12
3.1. Thin film deposition.....	12
3.1.1. Magnetron sputtering.....	12
3.1.2. Pulsed Laser Deposition (PLD).....	14
3.2. Photoelectron Spectroscopy (PES).....	15
3.2.1. Synchrotron Radiation Photoelectron Spectroscopy (SRPES)	19
3.3. Scanning Electron Microscopy (SEM).....	20

4. Experimental equipment.....	23
4.1. Thin film deposition equipment.....	23
4.2. PES equipment.....	26
4.3. Scanning Electron Microscope.....	29
5. Results.....	30
5.1. Magnetron sputtered CeO_2 layers doped by different concentration of platinum	30
5.2. Investigation of sputtered $Pt-CeO_2$ films deposited on CNTs.....	37
5.3. $Pt-CeO_2$ thin film catalyst grown on flat carbon substrates.....	48
5.4. Interaction of sputter deposited CeO_x thin films with silicon oxide.....	58
5.5. $Pt-CeO_2$ thin films prepared by PLD.....	68
6. Summary and conclusions.....	73
Bibliography.....	76
List of Tables.....	82
List of Abbreviations.....	83

1. Introduction

1.1. Motivation

Recently, concern about harmful exhaust emissions from motor vehicles has been increasing. The limited resources of crude oil fuel have stimulated extensive search for new sources of energy. Chernobyl and Fukushima disasters have shown people the risks of atomic energy. Hence authorities of many developed countries are pushed to find alternative energy renewable sources such as fuel cells that can reduce environmentally harmful emissions. There are many types of fuel cells but probably the most widely used is polymer electrolyte membrane fuel cell (PEMFC) where hydrogen and/or methanol are used as a fuel. This type of fuel cell is expected to be a key element of the future technology due to operation at relatively low temperatures (~ 80 °C) and high power density. However, the main problem of using PEMFC is its high cost. For example, the cost of an 80-kW automotive polymer electrolyte membrane fuel cell system in volume production (500,000 units/year) based on 2012 technology and operating on direct hydrogen is projected to be \$47 per kW [1]. The goal is about \$35 per kW to compete with internal combustion engines. Main part of the price of the FC belongs to expensive *Pt* and *PtRu* catalysts that are most often used in fuel cell applications. Thus development of new catalysts that can replace expensive *Pt* in FC is a primary objective in many scientific and industrial laboratories around the world, among which is also our laboratory at Department of Surface and Plasma Science at Charles University in Prague. In our laboratory a great deal of investigation has been devoted in recent years to ceria based catalysts that were stated to be very active catalysts for fuel cell applications. Our group obtained a lot of significant results by studying reactivity of CeO_2 (111) and *Pt/CeO*₂ (111) model catalysts grown on copper. It motivated us to start investigations of real ceria based catalysts. The real catalysts were mainly prepared by magnetron

sputtering. It was found that the $Pt-CeO_2$ thin films deposited by magnetron sputtering on carbon nanotubes (CNTs) show extremely high activity in PEMFC [2]. However, mechanism of such activity was not completely clear. It was very important to ascertain possible processes that lead to such high catalytic activity of the $Pt-CeO_2$ catalyst prepared by magnetron sputtering. It was necessary to investigate the catalyst composition, morphology and stoichiometry and find whether they are interconnected.

1.2. Goals, objectives and structure of the thesis

The aim of the work was to investigate chemical interaction between atoms that occurs inside the magnetron sputtered $Pt-CeO_2$ thin film catalyst as well as chemical interactions between the film and a substrate on which it is deposited. Photoelectron spectroscopy (PES) is one of the most powerful analytical techniques used in field of heterogeneous catalysis. It provides detailed information on the electronic structure and chemical composition of the catalysts. Hence the $Pt-CeO_2$ system was investigated mainly by PES using both ordinary X-ray sources (XPS) and its more sophisticated modification, synchrotron light (SRPES). The $Ce\ 3d$, $O\ 1s$ and $Pt\ 4f$ photoemission core levels were analyzed showing stoichiometry of the catalyst film. Scanning electron microscopy (SEM) was used to monitor the catalyst morphology. The combination of PES and SEM techniques allows us to find the relation between stoichiometry and surface structure of the catalyst and explain its high activity in fuel cells.

The content in the thesis is divided into 6 chapters. It starts from the short introduction (*Chapter 1*). The *Chapter 2* gives a brief overview of PEMFCs and shows the major challenges to their widespread commercialization. Theoretical aspects of the main experimental techniques are given in the *Chapters 3*. Descriptions of the used experimental equipment are presented in the *Chapter 4*. The *Chapter 5* presents the main results of the work. This chapter is divided in five main parts. In the first part, the magnetron sputtered CeO_2 layers doped with different concentrations of Pt were investigated by SRPES method. It is shown that Pt is dispersed uniformly inside the CeO_2 film in the ionic state. It increases the reducibility of CeO_2 leading to the high activity of the sputtered $Pt-CeO_2$ thin film

catalyst. In the second part the results and discussions derived from $Pt-CeO_2$ deposited on different types of carbon nanotubes (CNTs) are considered. It is shown that the catalyst deposited on CNTs by magnetron sputtering shows unusual stoichiometry and surface structure. In the third part the catalysts prepared on different flat carbon substrates were investigated. This experiment helped to understand completely processes which take place during the magnetron sputtering of the $Pt-CeO_2$ thin films on CNTs. As the $Pt-CeO_2$ thin film catalyst is suitable for using in planar μ FCs that can be directly co-fabricated on silicon integrated circuit wafers using processes common in circuit fabrication, in the fourth part the catalysts deposited on different silicon substrates were investigated. It was shown that the catalyst film is very reactive and strongly interacts even with the silicon surface covered by thick layer of SiO_2 . In order to understand better the mechanism of plasma assisted growth of the Pt doped ceria films, in the last fifth part pulsed laser deposition method was used as a reference technique to prepare the $Pt-CeO_2$ layers. The investigations showed that the PLD prepared catalyst layers are non-porous, however also contain ionic platinum. In the last *Chapter 6* summary and conclusions of the thesis are presented.

2. Background

2.1. Polymer Electrolyte Membrane Fuel Cell (PEMFC)

2.1.1. Work principle of PEMFC

A fuel cell is an electrochemical device that produces electricity as result of electrochemical reaction between fuel (hydrogen or methanol) and oxidant (oxygen or air). As it was already mentioned PEMFC is the most promising type of fuel cells in future technologies. Work principle and basic scheme of PEMFC is presented in *Fig. 2.1.1*. It consists of two electrodes, the anode and the cathode, which are separated by polymer electrolyte membrane (PEM). As the electrodes thin porous carbon layers are often used. Each of the electrodes is covered by a catalyst film to accelerate the electrochemical reaction. The electrodes attached to PEM are forming so-called membrane electrode assembly (MEA). A gas diffusion layer (GDL) is closely connected to the porous electrodes to supply gaseous reactants, oxygen and hydrogen.

On the anode, H_2 molecules diffuse through GDL to the anode catalyst where dissociate on two protons and two electrons (hydrogen oxidation reaction, HOR):



The protons are conducted through PEM to the cathode, while the electrons are forced to go through an external electrical circuit (supplying power) because the membrane is electrically insulating. On the cathode catalyst, oxygen molecules react with the arriving electrons and protons to form water (oxygen reduction reaction, ORR):



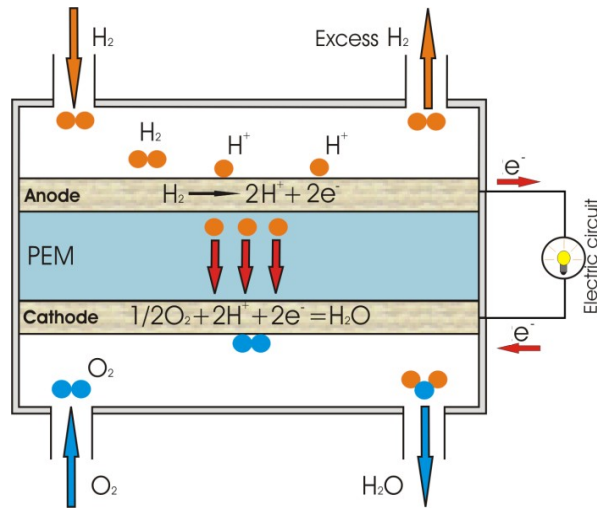


Figure 2.1.1. Basic scheme of PEMFC

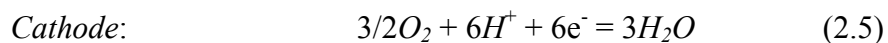
Now, if summarize Equations (2.1) and (2.2), we obtained overall fuel cell reaction:



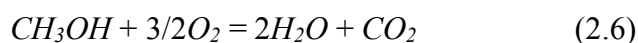
It can be seen that the product of fuel cell operation is water that makes them so-called “clean” source of electrical energy.

2.1.2. Types of PEMFC

It should be mentioned that usage of hydrogen as a fuel has a significant barrier of widespread use of PEMFCs due to difficulties with H_2 storage. Hence a great deal of work has been done on development of PEMFC that is fed by methanol. This type of FC is called direct methanol fuel cell (DMFC). Direct methanol fuel cell technology is relatively new compared with that of fuel cells powered by hydrogen; nevertheless this technology is developing very quickly. It has almost the same construction as the hydrogen FC. DMFCs use methanol/water solution as fuel and work near room temperature. Electrochemical reactions that take place on the electrodes of DMFC are:



If summarize Equations (2.4) and (2.5), we obtained overall fuel cell reaction:



We can see that DMFC produces CO_2 in addition to water unlike the hydrogen FC which produces only water.

In recent years a new planar concept of micro fuel (μ -DMFC) is proposed [3-5]. In *Fig. 2.1.2* the basic scheme of this fuel cell is presented. The μ -DMFC is supposed to be co-fabricated on the same support as the electric circuit (usually silicon). The possibility of co-fabricating a power source on the same substrate as the electric circuit offers many advantages, including a reduction in size and weight, and lower cost. The important problem of planar type fuel cells is the ohmic resistance due to increasing length of interconnections and the collector adhesion. Hence, metals which are difficult to oxidize, such as gold, should be used in there. The second main problem is absence of suitable active catalysts, or better to say catalyst preparation techniques. The standard wet-process techniques of powder catalysts are incompatible with the μ FC technology. In this case catalyst should be prepared by using some deposition techniques. However, thin film catalysts deposited by sputtering usually have a relatively low specific surface area. Thus they should be prepared as nanoporous structures or deposited on a nanoporous substrate.

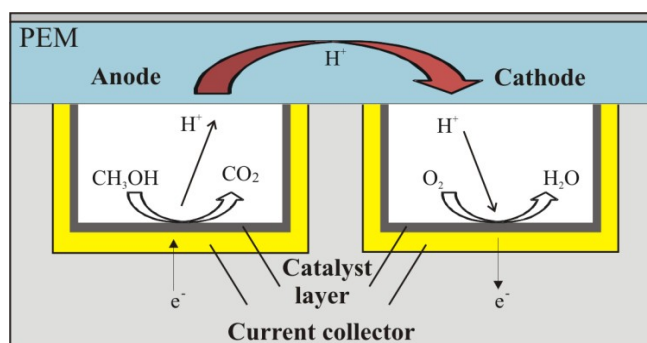


Figure 2.1.2. Basic scheme and work principle of planar silicon-based μ -DMFC

2.1.3. Carbon nanotubes in PEMFC

In order to have a better electron transport from the catalyst surface to the external circuit the catalyst in PEMFC is usually supported by carbon powder. However, even with the most advanced conventional electrodes, there is still a

significant portion of the catalyst that is isolated from the external circuit and/or the PEM. Carbon nanotubes (CNTs) show unique mechanical and electrical properties such as excellent thermal and electrical conductivity, high electrochemical and thermal stability, perfect corrosion resistance and high mechanical strength. All this make CNTs an ideal material for use in fuel cell applications to improve performance and decrease size of PEMFC [6, 7]. CNTs can be grown directly on GDL by chemical vapor deposition (CVD) technique and further coated by the catalyst. The grown CNTs make perfect electrical contact between the catalyst and external circuit. Another way is to put CNTs on GDL by the sedimentation method. The use of multiwall carbon nanotubes (MWCNTs) as a platinum support for PEMFCs was investigated as a way to reduce the cost of fuel cells through an increased utilization of platinum [8]. It was demonstrated that use of CNTs can substantially increase the utilization efficiency of the *Pt* catalyst.

2.2. Catalysts for fuel cells

As mentioned above, catalyst is the most important part of a fuel cell. So far *Pt* particles on porous carbon supports or CNTs are the most effective catalyst used in PEMFCs. Nearly all hydrogen fed PEMFCs use *Pt* catalyst on both the anode and cathode sides, i.e. for HOR and ORR. However, *Pt* on the anode side can be poisoned (deactivated) by the carbon monoxide (*CO*) present in hydrogen fuel or formed during the methanol oxidation (in case of DMFC). To overcome this problem, *Pt* based alloys such as *PtRu* is used due to its higher *CO* tolerance [9].

The high cost of current *Pt* and *PtRu* catalysts is hindering the widespread commercialization of PEMFCs. Nowadays, one the main goals of PEMFC catalyst design is to reduce amount of used *Pt* by increasing its activity. Another possible way is a development of new *Pt* free catalysts active enough to replace expensive *Pt* catalyst in the PEMFCs [10].

There are many possibilities how to increase the performance of platinum catalysts. One way to increase reaction rate is an optimization of the size and shape of the platinum particles. By decreasing the particles size we increase the total surface area that is exposed to the reactants [11]. The *Pt* particle shape is also important because high-index facets of the particle have a large density of atomic

steps that show higher catalytic activity than equivalent surface area of low-index facets [12].

A second way how to increase an efficiency of *Pt* usage is to combine *Pt* with other materials. It can be obtained by alloying *Pt* with other metals (*Ni*, *Fe*, *Co*...) or by dispersing *Pt* over suitable oxide catalyst supports (*CeO₂*, *TiO₂*, *WO₃*...) [13-17]. An interaction that may occur at interface between metal phase and support is called metal-substrate interaction (MSI). MSI depends strongly on used materials and size of the deposited particles (smaller metallic particles gives stronger MSI).

2.2.1. *CeO₂* as a catalyst and catalyst support

Cerium is a metal that belongs to the lanthanide group and has the valence orbital electron configuration $4f^1 5d^1 6s^2$. In nature there are two oxidation states of cerium, Ce^{+3} and Ce^{+4} , which are commonly occurring in two oxides, Ce_2O_3 and CeO_2 , respectively. The difference between the two oxidation states is that Ce^{3+} has one electron in the *4f* orbital, while Ce^{4+} has empty the *4f* orbital [18].

CeO₂, usually called ceria, has a fluorite crystal structure which is shown in *Fig. 2.2.1*. In this structure, each Ce^{4+} cations is coordinated by eight equivalent nearest-neighbor oxygen anions and each O^{2-} anion being coordinated by four cerium cations.

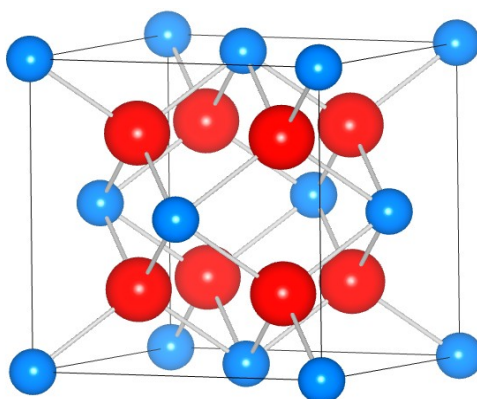


Figure 2.2.1. The crystal structure of *CeO₂* (red spheres represent O^{2-} anions and small blue spheres Ce^{4+} cations.)

Ceria cations can reversibly switch between Ce^{4+} and Ce^{3+} oxidation states releasing and retaking oxygen atoms. This ability, called oxygen storage capacity (OSC), and the high oxygen mobility give rise to its wide application in catalysis [19]. However, OSC of pure CeO_2 deactivates at high temperatures due to sintering of CeO_2 particles [20].

CeO_2 doped by noble metals often reveals higher catalytic activity and it is widely used as a catalyst in different processes like elimination of CO and NO_x from automotive exhaust gases [21], water-gas shift reactions [22], oxidation of ethanol [23], and decomposition of methanol [24]. What makes CeO_2 more active for oxidation reactions is the increase of oxygen mobility, which is the result of introduction of defects sites by addition of dopants in the CeO_2 lattice. An introduction of some small cations into CeO_2 lattice strongly enhances the reduction of Ce^{4+} to Ce^{3+} which, in turn brings an increase in oxygen mobility resulting in higher OSC. On the other hand, if there are metal nanoparticles on the CeO_2 , MSI results from electron transfer from nanoparticles to the support which, in turn results in higher OSC, too [15].

2.2.2. $Pt-CeO_2$ as a catalyst for fuel cell applications

Modification of crystal structure of pure ceria by Pt doping can significantly increase the OSC. Moreover Pt atoms catalytic activity is influenced by the ceria support as well. Experiments show that the activity of $Pt-CeO_2$ is directly related to structure of the ceria support. Growth of ceria crystallite size leads to a deactivation of the catalyst [25]. There are many preparation techniques of $Pt-CeO_2$ catalyst which mostly belong to “wet” techniques when the catalyst is prepared by incipient wetness impregnation with aqueous solutions of the metal salts and further calcinations at high temperature [26-28]. Recently, such prepared $Pt-CeO_2$ materials have been investigated as anode catalyst for development of DMFC [26, 28, 29]. It was shown that $Pt-CeO_2$ is a very promising cheap catalyst for fuel cell applications and can be a potential candidate to replace expensive Pt catalyst. The catalyst was also tested in the DMFC cathode for enhancement of the ORR activity. It was suggested that the ORR activity at the interface between Pt and cerium oxide was improved by the oxygen storage property of CeO_2 . Investigation of the time stability

of ORR activity on $Pt-CeO_2$ cathode showed relatively long time stability at high fuel cell performance [30].

Recently, very active $Pt-CeO_2$ thin film catalyst was prepared by magnetron sputtering. By testing the catalyst on a PEMFC anode it was shown that layers containing nearly 100% concentration of cationic platinum Pt^{2+} , Pt^{4+} revealed very high specific power (electrical power per amount of Pt) [31]. High activity and low cost of the $Pt-CeO_2$ catalyst prepared by magnetron sputtering make it a very promising material for both conventional PEMFC and planar μ -DMFCs.

As it was already mentioned, the CO poisoning of Pt in the FC anode is a serious problem of the development of long life time FC systems. CO tolerance of $Pt-CeO_2/C$ anodes has been actively investigated. It was reported that $Pt-CeO_2$ catalyst reveals improved CO tolerance of Pt in the electrochemical oxidation reaction of methanol. More details about the CO tolerance of $Pt-CeO_2$ can be found in [32].

2.2.3. CeO_2 and Ce_2O_3 studied by core-level photoelectron spectroscopy

Photoelectron spectroscopy makes possible to follow the reduction and oxidation (switching between Ce^{4+} and Ce^{3+} states) of ceria surface simply by measuring the Ce $3d$ core-level photoelectron spectrum.

In the simplest description CeO_2 is regarded as a typical example of the Ce compound consisting of Ce^{4+} ($4f^0$) cations, while Ce_2O_3 is formally considered to consist of Ce^{3+} cations that have partially occupied $4f$ band ($4f^1$) [33-36]. Experimental data of Ce $3d$ XPS of CeO_2 exhibit three $3d_{3/2}$ - $3d_{5/2}$ spin-orbit-split doublets as shown in *Fig. 2.2.2(a)*. This is in a strong contrast with spectrum of Ce_2O_3 that consists of two $3d_{3/2}$ - $3d_{5/2}$ spin-orbit-split doublets (*Fig. 2.2.2(b)*). For CeO_2 the Ce $3d$ f^1 doublet with main peak at 882.4 eV should be fitted by an asymmetric feature accordingly to [37], while the other two features are symmetric. The doublets represent different $4f$ configurations in the photoemission final state and arise from the Ce $4f$ hybridization in both the initial and the final states [35, 38]. Indeed, in the final state of the photoemission a $3d$ core electron is escaped. Then an attractive core-hole potential is exerted on $4f$ state, and $4f$ level is pulled down. It makes possible an electron transfer from O $2p$ valence band (ligand) to the Ce $4f$

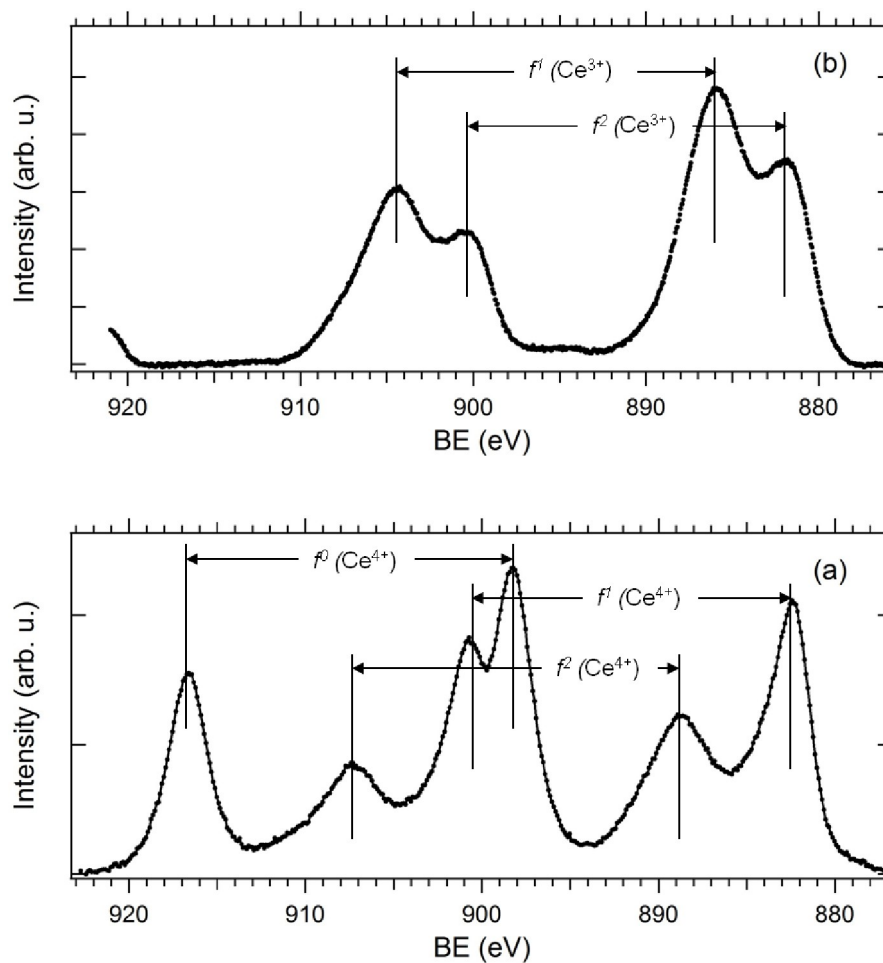


Figure 2.2.2. *Ce 3d* XPS spectra obtained for CeO_2 (a) and Ce_2O_3 (b).

level. Thus in case of CeO_2 there are three possible final states: $4f^0$ configuration when no electrons transfer occurs, $4f^1$ configuration when one electron transfer occurs and $4f^2$ configuration when two electrons transfer occurs (Fig. 2.2.2(a)). The *Ce 3d* spectrum of Ce_2O_3 shows only two peaks which are states of $4f^1$ and $4f^2$ configurations. There is no $4f^0$ component in the ground state (there is one electron on the *Ce 4f* level) therefore $4f^0$ final state cannot occur in the *Ce 3d* spectrum (Fig. 2.2.2(b)).

3. Theoretical description of the used experimental techniques

3.1. Thin film deposition

3.1.1. Magnetron sputtering

Magnetron sputtering is a coating technique widely used in both industrial and laboratory applications. In the conventional sputtering process, a target (or cathode) is bombarded by ions of working gas generated in glow discharge plasma which is situated in front of the target. The sputtering ions are accelerated by a negative voltage applied to the cathode. The bombardment process causes removal, i.e. sputtering, of target atoms, which then condense on a substrate as a thin film [39]. The conventional sputtering process usually gives low deposition rates and needs very high cathode voltage and working gas pressure to sustain plasma. To overcome these problems the magnetron sputtering configurations use magnetic field from permanent magnets situated near the target to confine electrons in the vicinity of the target. The magnets are arranged in a way that one pole is positioned at the central axis of the target and second pole is formed by a ring magnet around the outer edge of the target. This arrangement creates magnetic field with configurations that is shown in *Fig. 3.1.1*. It can be seen that there are crossed electric and magnetic fields that force electrons to circulate along the magnet field lines. These circulations increase the traveling way of electrons that leads to substantial increase of ionizing electron-atom collisions increasing the plasma density. This, in turn, leads to increased ion bombardment of the target giving higher deposition rate. The increased ionization efficiency achieved in the magnetron allows the discharge to be

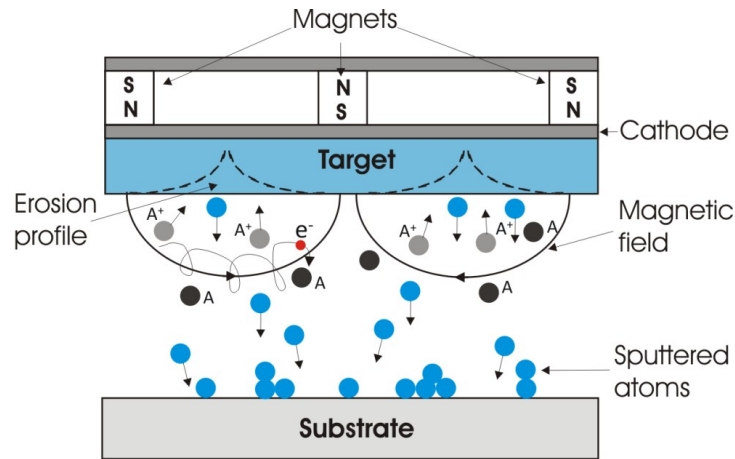


Figure 3.1.1. Cross-sectional scheme of RF-magnetron sputtering process.

maintained at lower operation pressures (typically 10^{-1} Pa) and lower cathode voltage (typically 500 V). Depending on a type of sputtered materials there are two types of magnetron operation: DC and RF-sputtering. Normally, DC power sources are used in cases when the sputtered target has good electrical conductivity (for example, metals). Obviously, in this case there is the electron-ion recombination process on the target when the incident ions take electrons from the target to become neutral atoms. But if the target is made of insulating material very soon its surface will be charged positively. This charge creates retarding electrical field decreasing sputtering efficiency. To overcome this problem, RF (radio frequency; usually 13.56 MHz) power supply is used for sputtering an insulating material. If a high-frequency power source is applied, relatively light electrons respond instantaneously to the rapidly varying field unlike the heavier ions which are inertially confined. The RF field alternately opens and closes the electron trap allowing electrons to escape and recharge the target surface when the trap is open.

There are two types of sputtering depending on a working gas used in magnetrons. In non-reactive magnetron sputtering an inert gas (typically *Ar*) is used, whilst in reactive magnetron sputtering a chemically reactive gas (O_2 , N_2 ,...) is inserted to the system.

3.1.2. Pulsed Laser Deposition (PLD)

Pulsed laser deposition (PLD) is a thin film deposition technique where a high power pulsed laser beam is focused inside a vacuum chamber to vaporize a material that is deposited as a thin film. This process can occur in ultra high vacuum or in the presence of a background gas, such as oxygen which is commonly used when depositing oxide films. The target is usually rotated in order to avoid repeated ablation from the same spot on the target. Another possibility is the target rastering under a fixed-position of the laser beam.

A basic set-up for PLD is quite simple relative to many other deposition techniques and it is schematically shown in *Fig. 3.1.2*. In a chamber, an elementary or composite target is struck at angle of 45° by a focused pulsed laser beam. The atoms and ions ablated from the target are deposited on a substrate. Mostly, the substrate is attached with the surface parallel to the target surface at a target-to-substrate distance of typically 2-10 cm. By adjusting a number of laser pulses and time of deposition, the layer of desired thicknesses can be created.

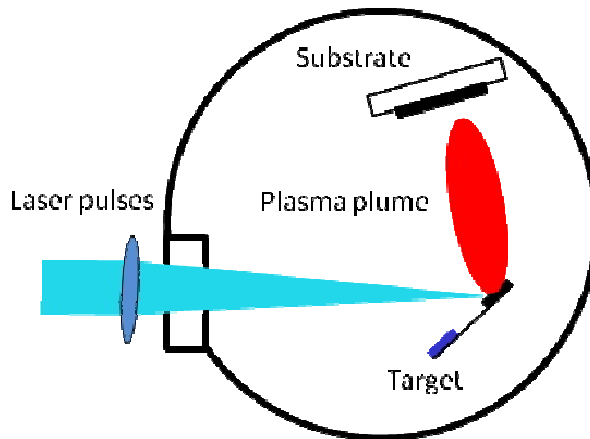


Figure 3.2.1. Schematic diagram of a typical PLD set-up.

The physical phenomena of laser-target interaction and film growth are quite complex. When the laser pulse is absorbed by the target, energy is first converted to electronic excitation and then into thermal, chemical and mechanical energy resulting in evaporation, ablation, plasma formation and even exfoliation. The ejected species

expand into the surrounding vacuum in the form of a plume containing many energetic species including atoms, molecules, electrons, ions, clusters, particulates and molten globules, before depositing on the typically hot substrate. More information about PLD can be found in [40, 41].

3.2. Photoelectron spectroscopy (PES)

In this thesis, all prepared samples were studied mainly by using synchrotron radiation PES technique with photon energy of about 6 keV. Laboratory XPS system was used when it was necessary to calculate the *Pt* concentration in the film or to see changes of stoichiometry depending on the information depth.

PES is based on the photoelectric effect which occurs when high energy photons (from tens of eV up to tens of keV) bombard a material with the consequent emission of electrons (photoemission). *Fig. 3.2.1* shows main components of modern PES equipment. In this technique, the sample surface is irradiated with a monochromatic photon source. The photoelectrons are then analyzed by an analyzer

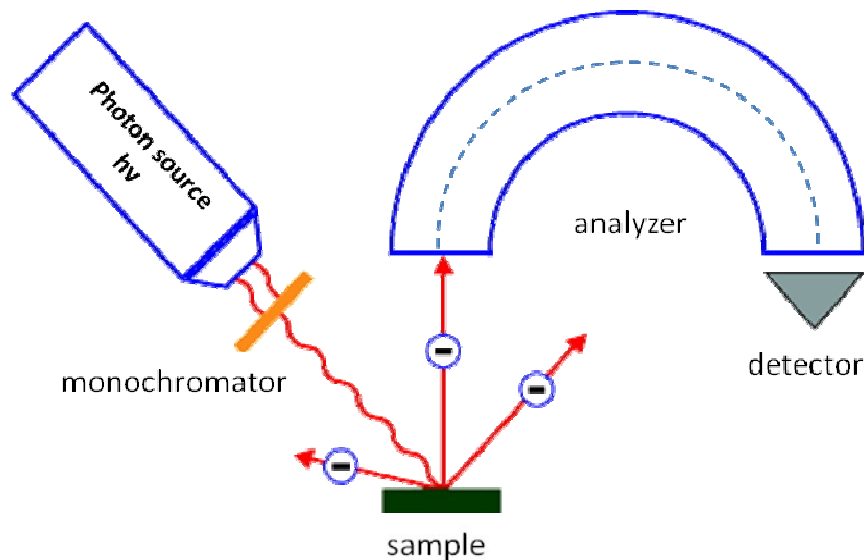


Figure 3.2.1. Principal scheme of PES equipment.

with respect to their kinetic energy E_k . The electrons can be emitted from both deep core levels and shallow weakly-bound valence states; they are contributing to the photoelectron spectrum. The spectrum displays all accessible energy levels as a distribution of photoelectrons versus their kinetic energies. The typical wide spectrum of the sputtered CeO_2 film is shown in Fig. 3.2.2. The kinetic energy E_k of the photoelectrons emitted from a sample is given by following equation:

$$E_k = h\nu - E_B - \Phi \quad (3.1)$$

where $h\nu$ is the energy of the incident photons, E_b - the binding energy of the electron in a particular level relative to the Fermi level (E_F) and Φ is the work function of the sample. For a conducting sample which is in electrical contact with the spectrometer the work function of the spectrometer Φ_s should be used instead of Φ in Equation 3.1 because E_F of the sample becomes equal to E_F of the spectrometer. The work function of the spectrometer, Φ_s , is usually determined by measuring E_F of a gold sample that is in electrical contact with the spectrometer. The $Au 4f$ level is also used as a reference to calibrate the spectrometer. The position of the $Au 4f$ peaks should be at $E_B=84.0$ eV ($4f_{7/2}$) and 87.7 eV ($4f_{5/2}$) below E_F [42]. An insulating sample can be uncertainly surface charged, and in this case the $C 1s$ peak of surface carbon at energy of 284.6 eV or other peak of known E_b is used as a reference for charge correction.

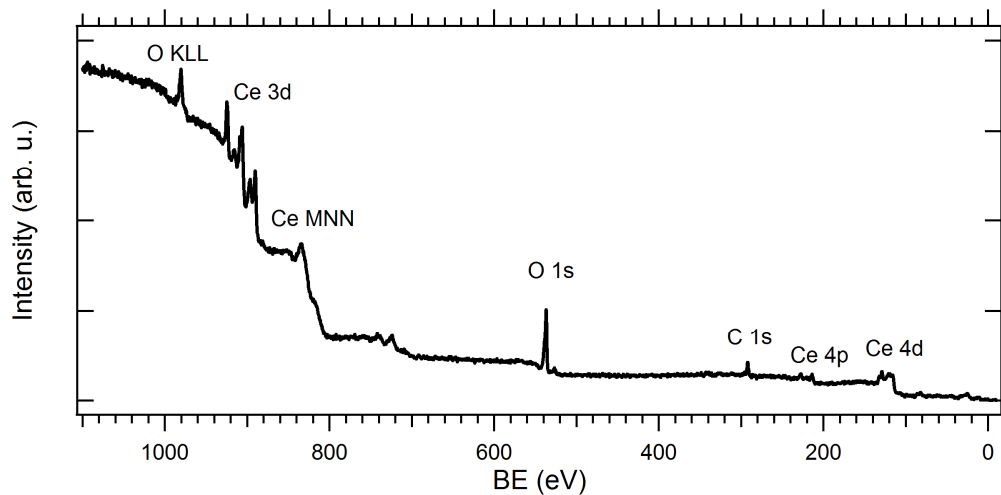


Figure 3.2.2. PES wide spectrum of the sputtered CeO_2 film

The photoelectron peaks, as shown in *Fig. 3.2.2*, are labeled according to the quantum numbers of the level from which the electron originates using the nomenclature nl_j where n is the principal quantum number, l is the angular momentum quantum number and j is the total momentum quantum number. The angular momentum quantum number is associated with the orbital letters (s, p, d, and f). The total momentum quantum number j is determined as a sum of the angular momentum quantum number l and the spin momentum number s which can be equal to $1/2$ or $-1/2$. Therefore, in case of s levels when $l=0$, we have singlets, whilst all other levels with $l>0$ give rise to doublets. The doublet states are different in energy because the unpaired electron left in an orbital after photoionisation can have its spin and orbital angular momentum vectors either parallel or anti-parallel. This is known as spin-orbit splitting (or $j-j$ coupling). The energy difference between the two doublet components, which can be in range of electron volts (sometimes tens of electron volts), increases with atomic number Z , for a given subshell (constant n , l), and decreases as l increases for constant n . The relative intensities of the components are given by the ratio of their degeneracies $2j+1$, thus, for example, for p electrons ($l=1$) the relative intensities are 1:2 [43].

Besides the photoelectron peaks additional peaks called Auger peaks can be distinguished in the spectrum. Indeed, after creation of a hole in the core level the excited ion tends to relax through two possible decay mechanisms: X-ray fluorescence and the Auger decay (*Fig. 3.2.3*). The Auger process includes an electron transition from a higher level to fill the photoelectron vacancy at a lower level resulting in the Auger electron emission. It can be seen in *Fig. 3.2.3 (c)* where the schematic of the Auger process is shown. The initial photohole was created in the K level (in Auger Electron Spectroscopy (AES) energy levels are denoted by the X-ray notation, K, L, M etc.). The relaxation happened via $L_2 \rightarrow K$ transition and electron emission from L_3 level. The final state is therefore a doubly ionized state with two vacancies in the levels involved in the process. The kinetic energy of the Auger electron depends only on the binding energies of involved levels and it is independent on the energy of the incident beam:

$$E_k(\text{KL}_2\text{L}_3) \approx E_B(\text{K}) - E_B(\text{L}_2) - E_B(\text{L}_3) \quad (3.2)$$

where $E_B(\text{K})$, $E_B(\text{L}_2)$, $E_B(\text{L}_3)$ are energies of the levels involved in Auger process.

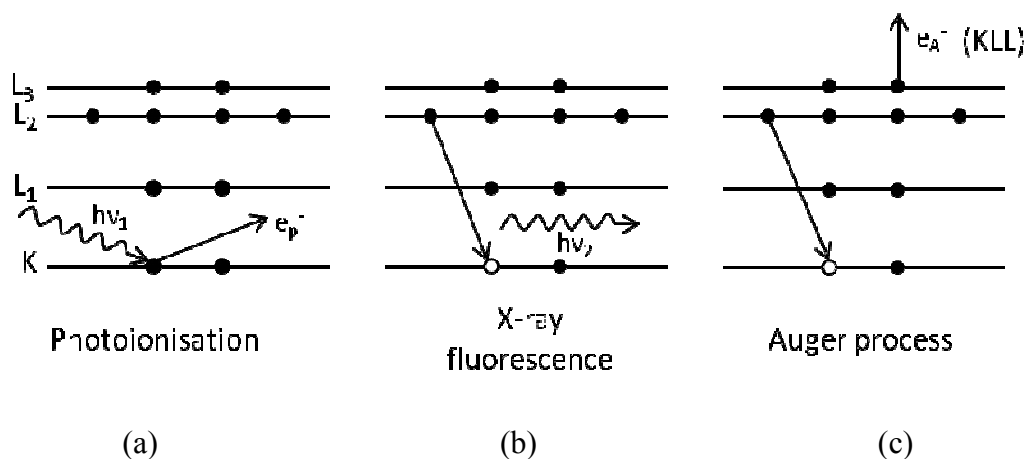


Figure 3.2.3. Drawing of the processes involved in X-ray photoemission: photoionisation (a), X-ray fluorescence (b) and Auger electron emission (c).

By using PES technique it is possible to obtain two different types of information: qualitative and quantitative. Qualitative information can be obtained from positions of photoelectron peaks in the spectra and from their shifts due to different chemical environments. Indeed each atom has its own unique electron configuration resulting in unique peak positions in the PES spectrum. When an element is in some chemical compound its chemical state can be different because its electronic configuration is influenced by other elements. It gives rise to the shifts in the PES peak positions called “chemical shifts” that are used in chemical state analysis.

Quantitative information comes from the relation between the intensity of the photoelectron peaks and the element concentration. In the simple case of a homogeneous solid the relative atomic concentration of any chosen element, C_A , is obtained from:

$$C_A = \frac{\frac{I_A}{S_A}}{\sum_n \frac{I_n}{S_n}} \quad (3.3)$$

where C_A is usually expressed as atomic %. The n is number of elements which give intensities (peak areas) of I_A, \dots, I_n measured with relative sensitivity factors S_A, \dots, S_n [43].

Additional peaks due to the so called electron *shake-up* and *shake-off* processes sometimes appear on the high binding energy side of a photoelectron peak.

These features correspond to photoelectrons emitted from an atom in which valence electrons go into an excited (*shake-up*) or ionized (*shake-off*) state as consequence of the sudden perturbation caused by the photoelectron ejection. The presence of these types of peaks may be useful for chemical state determinations.

Photoelectrons that lose part of their kinetic energy during transportation in solids to the surface form background of the spectrum. For quantitative analysis this background has to be removed by using suitable method. There are many different procedures how to subtract the spectrum background; it can be linear background, Shirley background, Tougaard background etc. [44].

There are different photon sources which can be used in PES. The common laboratory source utilises characteristic X-rays produced by electron bombardment of different materials (Al, Mg, Ag, Cr...) with and without monochromatization. Gas discharged lamps also can be used. Wider energy choice offers the use of the monochromatic radiation produced by synchrotrons. Hence, depending on a type of source of the radiation there are two main PES modifications: X-ray Photoelectron Spectroscopy (XPS) and Synchrotron Radiation Photoelectron Spectroscopy (SRPES).

Laboratory XPS system is very convenient technique for quick chemical analysis. In common XPS machine for surface analysis X-ray source with dual Al/Mg anode is usually installed. The anode material is bombarded by electrons with energy up to 15 keV. The electron bombardment causes X-ray radiation from the anode that consists of the broad Bremsstrahlung radiation and the more intensive and narrow characteristic lines. Usually only the most intensive $K\alpha_{1,2}$ lines are used as a X-ray source, whilst the Bremsstrahlung radiation and weaker satellite lines are being suppressed by using an Al window.

3.2.1. Synchrotron Radiation Photoelectron Spectroscopy (SRPES)

PES excited by synchrotron radiation is usually called SRPES. It is undoubtedly the most universal light source that can be used in PES.

Synchrotron is a circular accelerator of electrons which irradiate light by passing through different magnetic devices. Electrons are forced to circulate in a storage ring by magnetic and electric fields at nearly the speed of light providing high-intensity, ultra-bright radiation from the infrared to hard X-rays range. The

radiation beams are collected by in-vacuum optical systems and propagate through beamlines to reach experimental stations where an array of different analytical and processing techniques is available.

When velocity of the electrons v is low, i.e. $v \ll c$ (c : velocity of light), the angular distribution of the emitted radiation from an electron is the same as the classical dipole radiation (spherical on a long distance). In case of high velocities ($v/c \sim 1$) the angular distribution of the radiation becomes strongly asymmetric; electrons emit photons mostly in the direction of their motion (a very narrow cone tangential to the electron path) [45]. The photons are emitted as a continuous spectrum with an intensity maximum at a critical wavelength, λ_c , which is directly proportional to the radius of storage ring and inversely proportional to the cube of the electron energy [43]. The synchrotron radiation is also polarized; polarization vector lies in the plane of the circulating electrons.

There are four generations of synchrotrons that have been built over the world. In the second generation the electron beam in a storage ring was deflected only by standard magnets called bending magnets. However, it was impossible to obtain high photon flux with this method. Hence, so-called undulators and wigglers were developed and used in further synchrotron generations. An undulator is a periodic magnetic structure (up to 100 magnets) typically several metres long which creates a sinusoidal magnetic field along the path of an electron. The undulator can produce relatively monochromatic radiation, which is up 10^4 times higher than intensity from a single bending magnet. More details about synchrotrons and the synchrotron radiation can be found in [46].

The advantages of synchrotron light are the high photon intensity (orders of magnitude higher than characteristic X-ray sources at the same energy), the ability to tune the excitation energy by using monochromators in a wide range, the narrow X-ray beam, and the fact that radiation is polarised.

3.3. Scanning Electron Microscopy (SEM)

The SEM is a microscope that uses a focused beam of electrons to produce images of a sample. The focused electron beam with energy typically up to 30 keV is scanned over the sample along parallel lines. The incident electrons interact with

electrons of the sample producing various signals that contain information about the sample including surface morphology, chemical composition, and crystalline structure of sample materials. These signals are collected, and in combination with position of the beam form a 2D image of the sample surface. Each image pixel on the display corresponds to a point on the sample. Intensity of the pixel is related to the signal intensity captured by a detector at the corresponding point. SEM is considered as relatively rapid, inexpensive and basically non-destructive approach in surface analysis.

When the electron strike the surface some of them are backscattered (and have energy similar to the incident beam), other will excite secondary electrons with energy <50 eV. The incident beam will also excite characteristic X-rays and visible light (cathodoluminescence). By using different types of detector each of these signals can be detected and used to create images at different SEM detection contrasts: backscattered electron (BSE) and secondary electron (SE). The X-rays can be detected by using energy dispersive X-ray detectors (Energy Dispersive X-ray Spectroscopy (EDXS)). A simplified schematic drawing showing different signals produced when the electron beam interacts with a solid surface is shown in *Fig. 3.3.1*. The region over which the incident electrons interact with the sample is

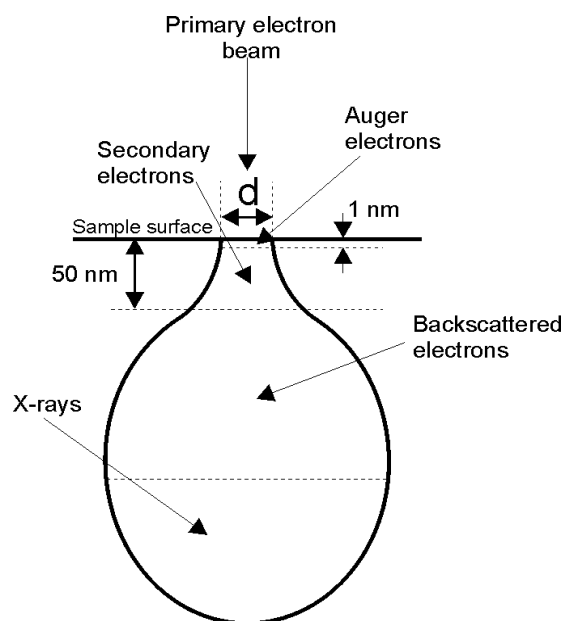


Figure 3.3.1. Schematic drawing showing different types of signal produced when the electron beam interacts with a solid sample.

known as interaction volume. The interaction volume has a pear-like shape. Backscattered and secondary electrons give information from tens up to hundreds of nanometres. X-rays are usually originates from much bigger depth of 1 μm or so

The SEM can produce high-resolution images of the sample surface, revealing details less than 1 nm in size. The SEM resolution directly depends on the electron spot size; the smaller spot size, the better image resolution. The spot size depends on the gun source size and aberrations in the focusing lenses and apertures (each optical component has some inaccuracy). SEMs that contain a field emission electron gun give much better resolution than that with a hot cathode. The image resolution also depends on the detection mode (or contrast). The SE detection mode is the most common and useful working mode for examining surface structure and gives the best resolution image of any of the scanning signals (resolve surface structures smaller than 10 nm). The BSE is good for examining a sample that consists of two or more different elements which differ significantly in their atomic numbers. Elements with higher atomic number will produce more backscattered electrons and will therefore appear brighter than low atomic number elements.

4. Experimental equipment

All thin film catalytic systems studied in the thesis were prepared by using sputtering equipment at Department of Surface and Plasma Science at Charles University in Prague. The films were deposited by using specially constructed deposition equipment consisted of two magnetrons. Some reference *Pt-CeO₂* films were prepared by means of PLD equipment at the Institute of Physics of the Academy of Science of the Czech Republic. PES measurements were performed at an ultra high vacuum XPS spectrometer at Department of Surface and Plasma Science at Charles University in Prague and at the undulator beamline BL15XU of the Spring-8 synchrotron facility in Japan. In this chapter a detail description of these equipments is given.

4.1. Thin film deposition equipment

The nonreactive RF magnetron sputtering was used to prepare *CeO₂* thin films. A basic scheme of the magnetron deposition of *CeO₂* can be seen in *Fig. 4.1.1* (DC magnetron is turned off). Sputtering was performed perpendicularly by using a 5.08 nanometer (2 inch) diameter *CeO₂* target installed on TORUS 2" UHV commercial magnetron from Kurt J. Lesker Company. The target was situated at distance of 90 millimeters from substrates. Sputtering was carried out in *Ar* atmosphere with total pressure of 6×10^{-1} Pa. For obtaining highly pure catalyst films the sputtering chamber was evacuated up to 5×10^{-4} Pa before starting deposition. The substrates were attached to specially designed sample holder at a rotating carousel. A shutter was mounted in front of the holder with a hole in the form of a 90° sector. This construction allowed preparation of several samples with different deposition parameters without opening the chamber. RF power was supplied by

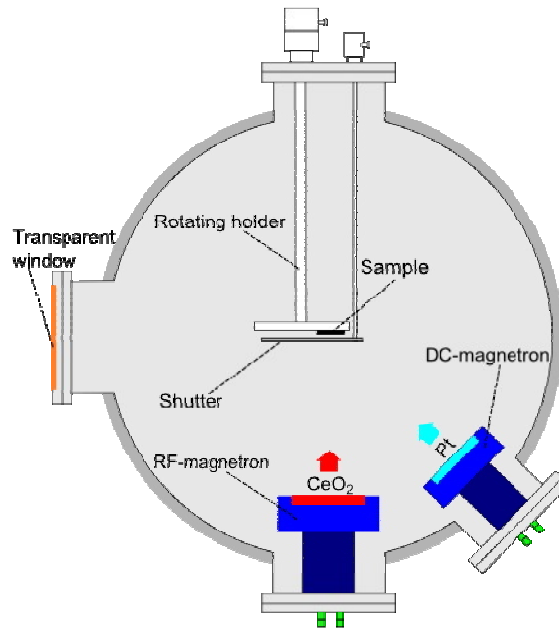


Figure 4.1.1. Schematic drawing of magnetron deposition of CeO_2 and $Pt-CeO_2$.

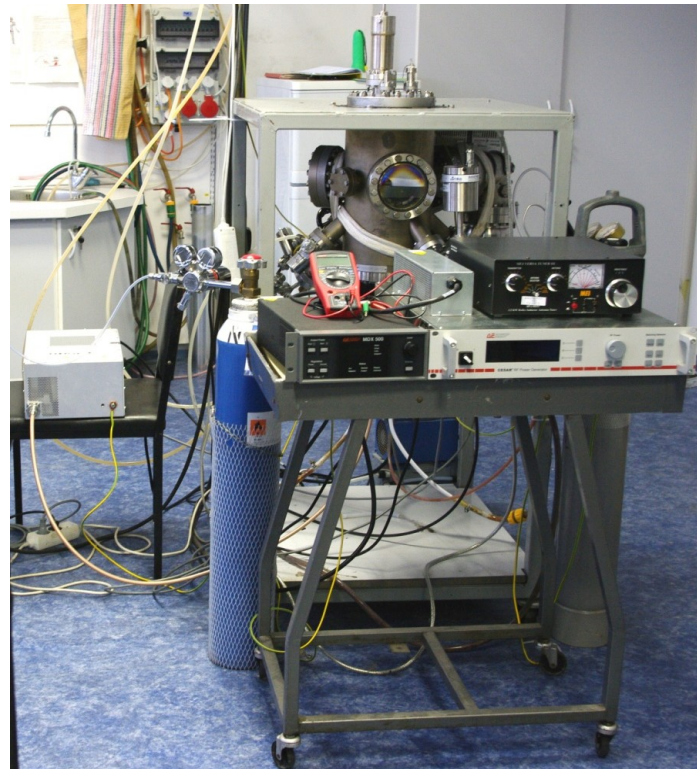


Figure 4.1.2. Magnetron set-up used for CeO_2 and $Pt-CeO_2$ depositions.

means of Cesar 136 RF Generator (13.56 MHz). The RF power generator was connected to MFJ-962D Antenna Tuner for sensing power transmission to the plasma and power reflection back to the source. By changing tuner settings it was possible to achieve a minimum power reflection. The applied RF power was 100 W giving the deposition rate of 1 nm/min. It was possible to obtain different deposition rates by changing the RF power. The deposition rate was calibrated using AFM measurements of a created step between the surface of the reference CeO_2 film deposited on the silicon wafer and the silicon surface.

The Pt -doped CeO_2 thin films were in most cases prepared by means of two magnetrons working simultaneously, as shown in *Fig. 4.1.1*. However, it was also possible to put a piece of Pt directly on the CeO_2 target and use only one magnetron for the catalyst preparation. But in this case it was very difficult to control Pt concentration in the film, while Pt adding by using the second DC magnetron (designed by Department of Macromolecular Physics at the Charles University in Prague) tilted by 45° relative to the CeO_2 target allowed continuous changing of Pt concentration simply by changing power on the DC magnetron. Distance from the DC magnetron to the substrate was 200 mm. DC power was supplied by MDX 500 DC power supplier. When applied DC power was 10 W, the Pt concentration in the $Pt-CeO_2$ thin film was about 5 %. The Pt concentration was determined by using XPS measurements. Appearance of the described magnetron sputtering equipment can be seen in *Fig. 4.1.2*.

The PLD prepared Pt -doped CeO_2 thin films were deposited by using special equipment at the Institute of Physics of the Academy of Science of the Czech Republic. A frequency-quadrupled Nd:YAG laser providing 90 mJ of 266 nm laser light in a 6 ns pulse was used to ablate the composite $Pt-CeO_2$ target with a 2.8 J cm^{-2} fluence on the target. The laser was always operated at the repetition rate of 10 Hz and the samples were grown as a result of 5200 laser shots. The target-to-substrate distance was kept fixed at 55mm in all the experiments. The film deposition was carried out in a vacuum chamber evacuated by oil-free turbo pumping to a base pressure of 2×10^{-4} Pa.

4.2. PES equipment

The ultra high vacuum XPS spectrometer used in the work is shown in *Fig. 4.2.1*. The spectrometer consists of two vacuum chambers separated by a gate valve. The smaller chamber called “fast entry” was used for sample insertion and quick evacuation up to pressure of 10^{-6} Pa by using combination of a turbo and rotary pumps. The chamber is equipped by a long sample transfer, which permits inserting the sample in the main chamber sustaining the UHV conditions. To prepare samples *in situ*, i.e. without exposure to the air, by sputtering a magnetron was mounted on the fast entry chamber.

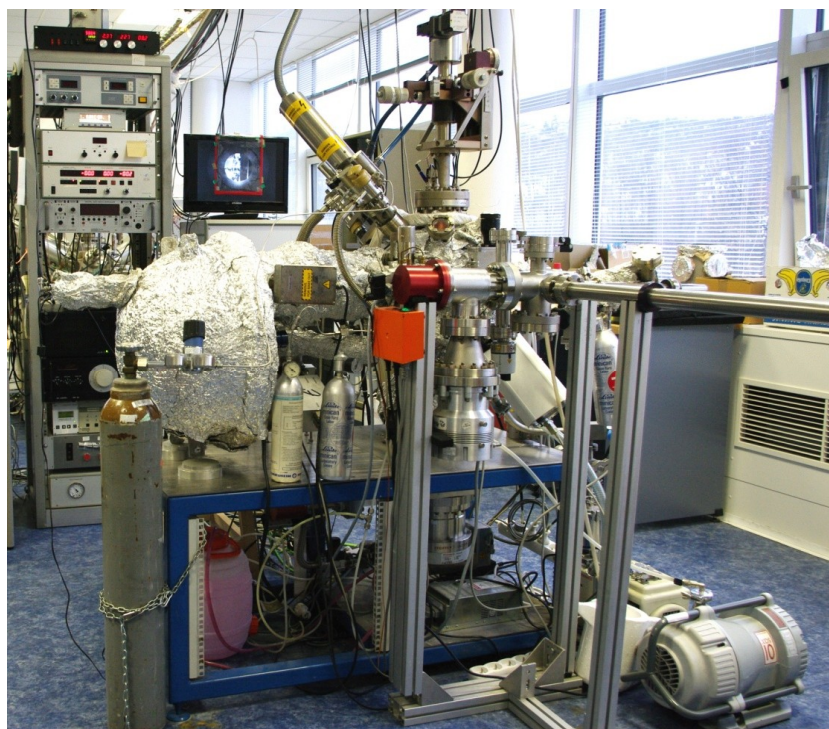


Figure 4.2.1. Experimental XPS spectrometer.

The main UHV chamber, with pressure of 5×10^{-8} Pa reached by means of a dry scroll and a turbo pumps, was equipped by a hemispherical electron energy analyser and a dual *Mg/Al* X-ray source. For XPS measurements only *Al* $K\alpha_{1,2}$ anode was chosen (1486.6 eV) because lower photon energy of the *Mg* $K\alpha_{1,2}$ X-ray source

(1253.6 eV) would lead in principle to higher but more inclined non linear *Ce 3d* spectrum background and consequently to lower peak fitting precision. It should be mentioned that energy of the main satellite line *Al K α_3* is 9.6 eV higher than the *Al K $\alpha_{1,2}$* lines and has intensity 7.8% of them.

The experimental chamber was equipped with the hemispherical electron energy analyser Phoibos 150, supplied by SPECS, with mean radius of 150 mm. The analyser was equipped with the nine channeltron electron detector MCD 9. Photoelectrons are coming into the transfer optic with the acceptance angle of 44°. The transfer optics allows setting of the electron pass energy by changing voltages on the electrodes. After passing through the transfer optics electrons come to the entrance slit, go through radial electric field produced by the hemispherical electrodes and finally arrive to the detector. All this system is controlled by the computer. In our case the analyser was always used in the constant pass energy mode with pass energy of 20 eV.

Total energy resolution of the spectrometer ΔE_{tot} depends both on the geometrical parameters of the analyser and on the angular divergence of the incoming photoelectrons:

$$\Delta E_{tot} = \sqrt{\Delta E_{hv}^2 + \Delta E_{anal}^2} \quad (4.1)$$

where ΔE_{hv} is energy resolution of the X-ray source; ΔE_{anal} - energy resolution of the analyser. The constant pass energy mode with pass energy of 20 eV that was used in our measurements produced ΔE_{tot} on the order of 1 eV.

The SRPES measurements were performed at the undulator beamline BL15XU of the SPring-8 synchrotron facility producing photons at energy around 6 keV. Because of the fact that the high photon energy of few keV belongs to the hard X-ray range, the abbreviation HAXPES (Hard X-ray Photoemission Spectroscopy) is usually used for this technique.

The synchrotron radiation of the BL15XU beamline generated by the undulator was monochromatized by a *Si* (111) double crystal monochromator and a *Si* 333 channel-cut post-monochromator. As result monochromatized X-rays with energy of 5950.3 eV was obtained. Energy width of X-rays was < 60 meV, whilst the total energy resolution of the spectrometer was estimated to be 280 meV. The brilliance of X-rays from the undulator source was efficient to detect small concentrations of detected elements, however the X-ray damage was sometimes

troublesome. Minimizing X-ray exposure time at the fixed point on the sample was important to prevent the X-ray damage on easily-decomposable samples.

The experimental equipment of the BL15XU beamline of synchrotron SPring-8 used for the HAXPES measurements is shown in *Fig 4.2.2*. It consists of the two separated chambers. The smaller chamber equipped with load lock and sample transfer system was used for quick sample loading (up to six samples in one loading). All HAXPES experiments on samples prepared *ex situ* were performed in the main UHV experimental chamber with base pressures around 5×10^{-7} Pa. The spectra were taken at the grazing photon incidence and normal photoelectron emission geometry. The experimental chamber was equipped with the hemispherical VG Scienta R4000 10 keV electron analyser. The analyser mean radius was 200 mm and it was equipped with the detection system based on a 40 mm diameter multi-channel plate (MCP) detector monitored by a FireWire CCD camera. The 2D image can be seen in real time on the computer screen or on an external monitor, which allows complete control over the experimental conditions and easy adjustment, for example, intensity optimisation [47].

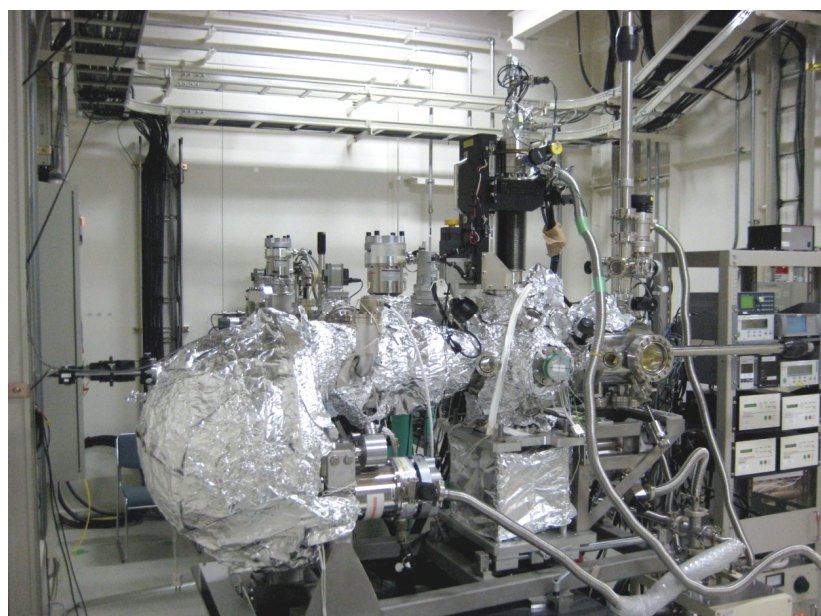


Figure 4.2.2. Hard X-ray photoelectron analyzer at beamline BL15XU of the SPring-8 synchrotron facility

4.3. Scanning Electron Microscope

Morphology of the $Pt-CeO_2$ thin films was investigated by means of TESCAN – MIRA scanning electron microscope, which is shown in *Fig. 4.3.1*. This SEM has a modern optics with a high brightness Schottky electron emitter for high-resolution. It is equipped with SE, BSE and EDXS detectors giving possibility to obtain images at the different contrasts. The microscope operating pressure was 1×10^{-2} Pa.



Figure 4.3.1. Scanning electron microscope used for the morphology studying of the $Pt-CeO_2$ thin film catalyst.

5. Results

CeO_2 and $Pt-CeO_2$ thin films deposited by magnetron sputtering on different substrates were investigated in this work. For PES spectra analysis of all Ce 3d spectra a Shirley type background was used, whilst for all Pt 4f spectra we used a linear background. In order to compare spectra from different substrates, they were normalized to the same spectrum area. All measured PES spectra were processed by using data processing KoLXPD software [48].

5.1. Magnetron sputtered CeO_2 layers doped with different concentrations of platinum

In this study, 30 nm thick CeO_2 layers doped with two different concentrations of Pt were prepared by magnetron sputtering and investigated by HAXPES method. The films were deposited on the Si (100) covered with a natural oxide layer (amorphous SiO_2) pre-cleaned in the ultrasonic bath. The Pt concentration in the low Pt -doped layer was about 5.6% relative to a total amount of Ce and O atoms. This value was calculated from areas of the Ce 3d, O 1s, and Pt 4f XPS peaks which were corrected by corresponding sensitivity factors. However, it should be mentioned that using of O 1s XPS peak area for calculation of Pt concentration can distort the real concentration value because it contains signals from different oxygen containing surface adsorbates. Thus in this work we prefer to use Pt/Ce ratio rather than absolute Pt concentration. The Pt/Ce ratio of the low doped film was 0.18. The second $Pt-CeO_2$ substrate with high concentration of Pt had the Pt/Ce ratio of 0.88. The reference 30 nm thick non-doped CeO_2 layer was also prepared.

The HAXPES *Ce 3d* spectra of the prepared films are presented in *Fig. 5.1.1*. The *Ce 3d* spectrum of the pure *CeO₂* layer in *Fig. 5.1.1(a)* consists of the three $3d_{5/2}$ - $3d_{3/2}$ spin-orbit-split doublets (f^0 , f^1 and f^2) characteristics of Ce^{4+} (*CeO₂*) states. As was described in *Subsection 2.2.3* these doublets represent different *4f* configurations in the photoemission final state and arise from the *Ce 4f* hybridization in both the initial and the final states. The *Ce 3d* spectrum of the low *Pt*-doped film in *Fig. 5.1.1(b)* shows two additional small $3d_{5/2}$ - $3d_{3/2}$ spin-orbit-split doublets characteristic of Ce^{3+} state with main peak energies at 885.4 and 881 eV (dotted lines). The same doublets can be seen in the *Ce 3d* spectrum of the high *Pt*-doped *CeO₂* film (*Fig. 5.1.1(c)*). We can observe that reduction of the *Pt-CeO₂* film is increasing when increasing *Pt* concentration. Moreover, it can be noticed that intensity of two $3d_{5/2}$ - $3d_{3/2}$ spin-orbit-split doublets, $f^1(Ce^{4+})$ and $f^2(Ce^{4+})$, are changing relative to $f^0(Ce^{4+})$ with increase of *Pt* concentration. It is well visible when compare $f^0(Ce^{4+})/f^1(Ce^{4+})$ and $f^0(Ce^{4+})/f^2(Ce^{4+})$ ratios of all prepared films that are presented in *Table 5.1.1*. In case of the pure *CeO₂* intensities of the $f^0(Ce^{4+})$ and $f^2(Ce^{4+})$ characteristics differ a little, whilst in case of the *Pt*-doped layers the $f^2(Ce^{4+})$ characteristic is more than twice higher than the $f^0(Ce^{4+})$ one. Even in the case of the low *Pt*-doped *CeO₂* film where the film reduction is almost not visible the decreasing of intensity of the $f^2(Ce^{4+})$ characteristic relative to the $f^0(Ce^{4+})$ can be well noticed. To explain such a behavior the differences in electron configuration of *Pt* doped *CeO₂* should be addressed; it will be discussed later.

Sample	$f^0(Ce^{4+})/f^1(Ce^{4+})$	$f^0(Ce^{4+})/f^2(Ce^{4+})$
<i>CeO₂/Si</i>	0.8	1.3
<i>Pt-CeO₂/Si (Pt low)</i>	1.01	2.2
<i>Pt-CeO₂/Si (Pt high)</i>	1.11	2.4

Table 5.1.1. The $f^0(Ce^{4+})/f^1(Ce^{4+})$ and $f^0(Ce^{4+})/f^2(Ce^{4+})$ ratios of the catalyst doped with different concentration of *Pt*.

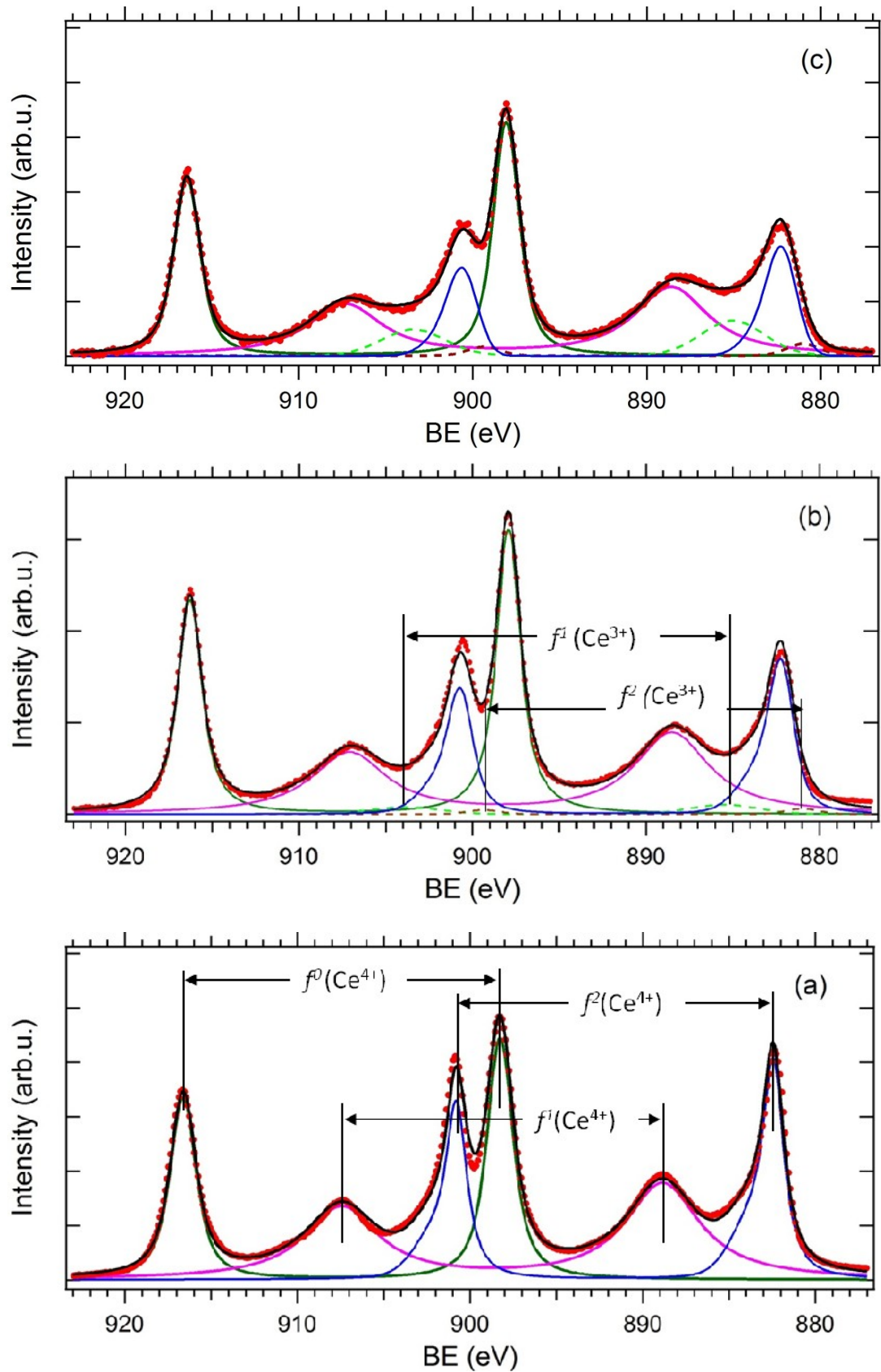


Figure 5.1.1. HAXPES $Ce\ 3d$ spectra of the CeO_2 films deposited on the Si wafer and doped with different concentrations of Pt : CeO_2 layer (a), CeO_2 film doped with low concentration of Pt (b), and CeO_2 film doped with high concentration of Pt (c).

In Fig. 5.1.2 corresponding $O 1s$ HAXPES spectra are shown. Only one peak at 529.6 eV is seen for the non-doped CeO_2 layer. It is attributed to oxygen anions bound to Ce^{4+} cations in the stoichiometric ceria. In the case of the Pt -doped CeO_2 films two additional peaks appear. It was recently found that water molecules partially dissociate on defects or step edge sites of cerium oxide. The OH group produced by the water dissociation fills the oxygen vacancy while the H atom bonds to a surface oxygen atom [49-52]. Therefore, the peak at 531.4 eV (marked $O-Ce^{3+}$) can be assigned to OH hydroxyl groups which are bound to the oxygen vacancies on the $Pt-CeO_2$ surface [53-56]. It indicates the presence of the small amount of Ce^{3+} cations seen in corresponding $Ce 3d$ spectra (Fig. 5.1.1(b, c)). The peak at 530.3 eV does not belong to pure CeO_2 and is called " $Pt-Ce-O$ ". We can see that this peak increases with the increasing Pt amount in the film. It was assigned to the mixed oxide because its binding energy does not correspond to any of Pt oxides [57]. It

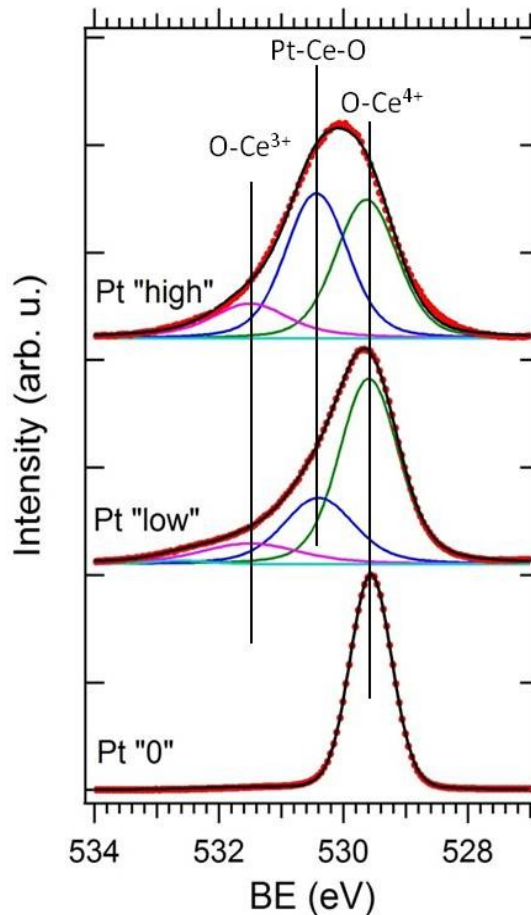


Figure 5.1.2. HAXPES $O 1s$ spectra of none and Pt -doped CeO_2 films deposited on the Si wafer.

should be mentioned that there is no any reference on the position of this peak in literature. Therefore the fitting procedure included peak energy fixing of the known “ $O-Ce^{4+}$ ” and “ $O-Ce^{3+}$ ” components, allowing to adjust the parameters of third one “ $Pt-Ce-O$ ”. As result one peak at about 530.3 eV that is assigned to the mixed oxide of Pt and Ce atoms was obtained.

An evolution of the Pt $4f$ core-level HAXPES spectra depending on Pt concentration in the CeO_2 layer is shown in Fig 5.1.3. The both spectra exhibit two Pt $4f_{7/2}$ - $4f_{5/2}$ doublets. The intensive Pt $4f_{7/2}$ - $4f_{5/2}$ doublet at 74.5-77.8 eV corresponds to Pt^{4+} state. The Pt^{4+} peak can be assigned to the “ $Pt-Ce-O$ ” mixed oxide according to the O $1s$ spectra. Because of not seeing any more peaks in the O $1s$ spectra that can indicate formation of another Pt oxide, the small Pt $4f_{7/2}$ - $4f_{5/2}$ doublet with main peak energy at 73.5 eV in the both spectra is assigned to formation of a small amount of $Pt-Ce$ alloy. It can be seen that the Pt $4f$ shape is the same in both cases and does not depend on Pt concentration. However, we have to remember that spectra in Fig. 5.1.3 are normalized to same area and in real situation the bottom spectrum is 4 times smaller than the top one. It means that the amount of $Pt-Ce$ alloy is proportional to

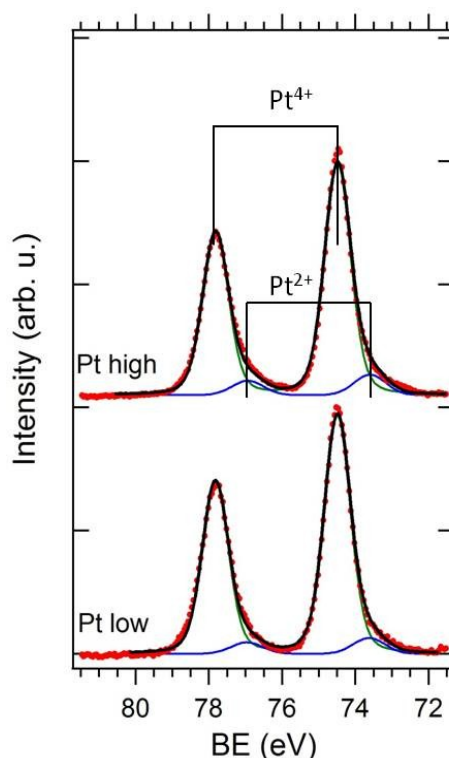


Figure 5.1.3. HAXPES Pt $4f$ spectra of the none- and Pt -doped CeO_2 films deposited on the Si wafer.

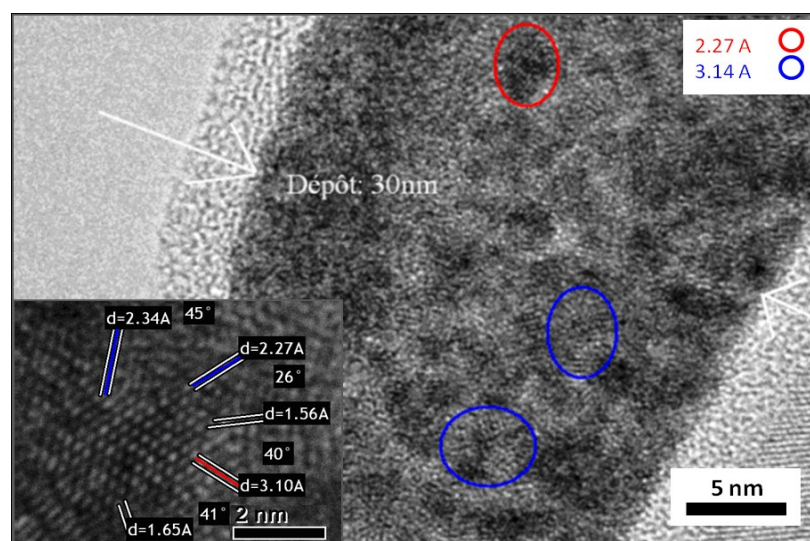


Figure 5.1.4. HRTEM micrograph of the high *Pt* doped CeO_2 film

concentration of *Pt*. The confirmation of the presence of *Pt-Ce* alloy in the *Pt-CeO₂* layers can be found on a high resolution transmission electron microscopy (HRTEM) micrograph which is shown in *Fig. 5.1.4.* taken from Ref. [58]. This picture shows typical structure of the *Pt-CeO₂* thin film deposited on the silicon wafer. We can see a nano-crystalline structure formed by crystallites ranging in 2-5 nm. Brighter crystals exhibit plane distance of 0.31 nm (blue circles) which correspond to d_{111} plane distance of CeO_2 . The darker crystals (red circles) are *Pt* richer (determined by X-ray Energy Dispersive Spectroscopy) and show the plane distance of 0.23 nm, mainly. This value can be observed in *Pt-Ce* alloy [52, 59] and/or metallic *Pt* [60]. However, *Pt 4f* HAXPES spectra do not show traces of metallic *Pt*, therefore we have to conclude that the plane distance of 0.23 nm corresponds to the *Pt-Ce* alloy. Moreover, according to crystallographic database plane distance of such *Pt* rich crystallite (inset picture) measured at different angles corresponds to $CePt_5$.

According to presented results we can conclude that the *Pt-CeO₂* films consist mainly of Pt^{4+} and Ce^{4+} ions. Nevertheless, the presence of *Pt* in the film caused appearance of small amount of Ce^{3+} ions. In literature the formation of Ce^{3+} ions after the *Pt* deposition on the stoichiometric CeO_2 film at room temperature is explained by purely electronic metal-oxide interactions between *Pt* aggregates and CeO_2 surface leading to electron transfer from *Pt* particles to ceria support [15]. In

our case the CeO_2 layer is continuously and uniformly doped by Pt and there are no Pt metal aggregates. It is suggested that Pt^{4+} ions are dispersed inside the bulk substituting Ce^{4+} ions in the CeO_2 lattice. This suggestion can explain the relative increase of the $Ce^{4+} f^d$ and f^2 spin-orbit-split doublet intensities respect to f^0 in the Ce 3d HAXPES spectra that was mentioned above. Indeed, the dispersed Pt^{4+} ions can modify the electronic structure of CeO_2 that can lead to decrease of probability of the electron transfer from O 2p valence band (ligand) to the Ce 4f level after photoemission. This in turn will lead to increase of probability of realization of the f^0 final state in PES. Dependence of Ce 3d satellite intensities on different electronic valence band configurations of Ce compounds is well described in [42]. There were also calculated the oxygen vacancy formation energies (E_{vac}) for the non-doped ceria and the Pt -doped ceria [61]. E_{vac} of 2.99 eV and 0.96 eV per vacancy were found for the non-doped and Pt -doped systems, respectively. It was shown that the dopant lowers the reduction energy more than three times. Therefore, we suggest that in our case some amount of oxygen vacancies responsible for formation of Ce^{3+} states can be created next to the embedded Pt ions even at room temperature.

In order to visualize what was said above a schematic model of the fluorite structure of ceria doped by Pt consisted of a twelve-layer stacking sequence of (111) planes is presented in *Fig. 5.1.5*. In this model the real sizes of the atoms and the distances between are not kept to real size them trying to make it more transparent. You can see that Pt^{4+} ions substitute the Ce^{4+} ions in the CeO_2 lattice forming the “ $Pt-Ce-O$ ” mixed oxide. The oxygen vacancies are created next to Pt ions inside and on surface of the $Pt-CeO_2$ film. This model explains why $Pt-CeO_2$ is more reduced in case of high Pt doping. We do not show in this model the alloy of Pt and Ce because its amount in the film is very small. However, we should remember that there is a small amount of $Pt-Ce$ crystallites. It should be also mentioned that this model is based on only the experimental results from this work and some suggestions. There can be also an interaction between Pt and Ce atoms leading to reduction of Ce^{4+} ions, the same as it is in the case of metallic Pt on ceria. Therefore, only precise theoretical calculations can give complete answer.

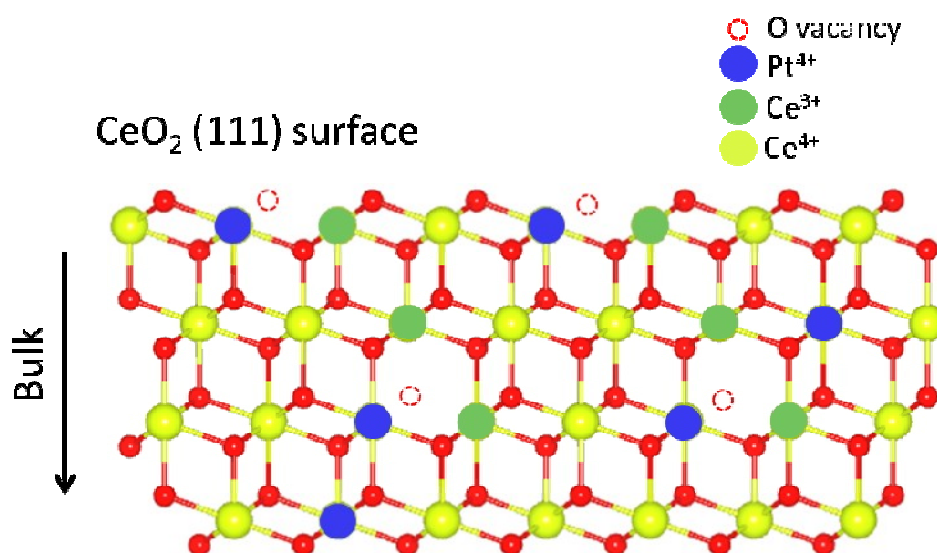


Figure 5.1.5. Side view of the stacking sequence of (111) crystallographic planes of the CeO_2 fluorite structure with oxygen vacancies, Ce^{3+} and Pt^{4+} cations (the section made along (1-10) crystallographic plane).

The conclusion of this study is that the sputtered $Pt-CeO_2$ catalyst on the reference silicon wafer shows formation of the “ $Pt-Ce-O$ ” mixed oxide. Pt ions are dispersed uniformly inside the CeO_2 film increasing its reducibility that can explain the high activity of the sputtered $Pt-CeO_2$ thin film catalyst. However, this statement needs further investigation by other techniques as well as by using calculation methods. There is also formation of small amount of $Pt-Ce$ alloy that can make some influence on the activity of the catalyst as well.

5.2. Investigation of sputtered $Pt-CeO_2$ films deposited on CNTs

The aim of this study was to investigate the $Pt-CeO_2$ thin film catalyst deposited by magnetron sputtering on different types of CNTs. It was very important to know whether there is some interaction between the $Pt-CeO_2$ layer and the substrate.

The 30 nm thick *Pt* doped *CeO₂* layers were deposited on the reference *Si* (100) covered with a natural oxide layer (amorphous *SiO₂*) pre-cleaned in the ultrasonic bath, commercial MWCNTs (Sigma Aldrich) and CNTs synthesized by CVD technique. The MWCNTs were dispersed in N,N-dimethylformamide (DMF) at a concentration of 1mg/30 ml and then deposited onto a GDL (GDL Alfa Aesar, Toray carbon paper, TGP-60), by sedimentation from the suspension. The CVD-CNTs were synthesized by CVD technique using *CH₄* as carbon precursor, *H₂/Ar* carrier gas and *Pd* nanoparticles as a catalyst. The *Pd* nanoparticles were synthesized directly on the GDL. The synthesis procedure for typical *Pd* nanoparticles used *PdCl₂* as *Pd* source, ethanol as reduction reagent and polyvinylpyrrolidone (PVP) as surfactant. The reaction mixture was put in ultrasonic bath and heated under reflux condenser for 2 hours. In order to stabilize *Pd* nanoparticles the GDL covered by PVP was dried, and then transfer to CVD deposition system. The CVD reactor was heated up to 700 °C with temperature increase rate of 5°C/min in the mixed atmosphere of *H₂* (30 sccm) and *Ar* (400 sccm). After reaching the final temperature the CNTs were grown in 100 sccm of *CH₄* mixed with 400 sccm of *Ar* for 2 hours. Then the reactor was cooled to room temperature in 400 sccm of *Ar*. All substrates were covered by cerium oxide and *Pt* simultaneously by using magnetron co-sputtering from *CeO₂* and *Pt* targets in argon atmosphere. The amount of *Pt* was chosen to be the same as in the *Pt* low concentration layer in *Section 5.1* with *Pt/Ce* ratio of 0.18.

Chemical state and composition of the catalysts were investigated by combination of laboratory XPS system with *Al K α* X-ray source and HAXPES with photon energy of 5956 eV. Morphology of the thin films was investigated by means of SEM at 10 keV electron beam energy. The catalysts prepared on the CNTs by magnetron sputtering exhibited surprisingly highly porous surface structure that is shown in *Fig. 5.2.1(a, b)*. Due to such surface structure a large part of the active catalyst surface is buried inside the film pores. However, the high energy of escaping electrons, which results in high inelastic mean free path of photoelectrons, makes HAXPES technique particularly suitable for investigation of buried species inside the pores. The *Pt-CeO₂* film on the reference silicon substrate showed a smooth surface morphology without any visible surface features (*Fig. 5.2.1(c)*).

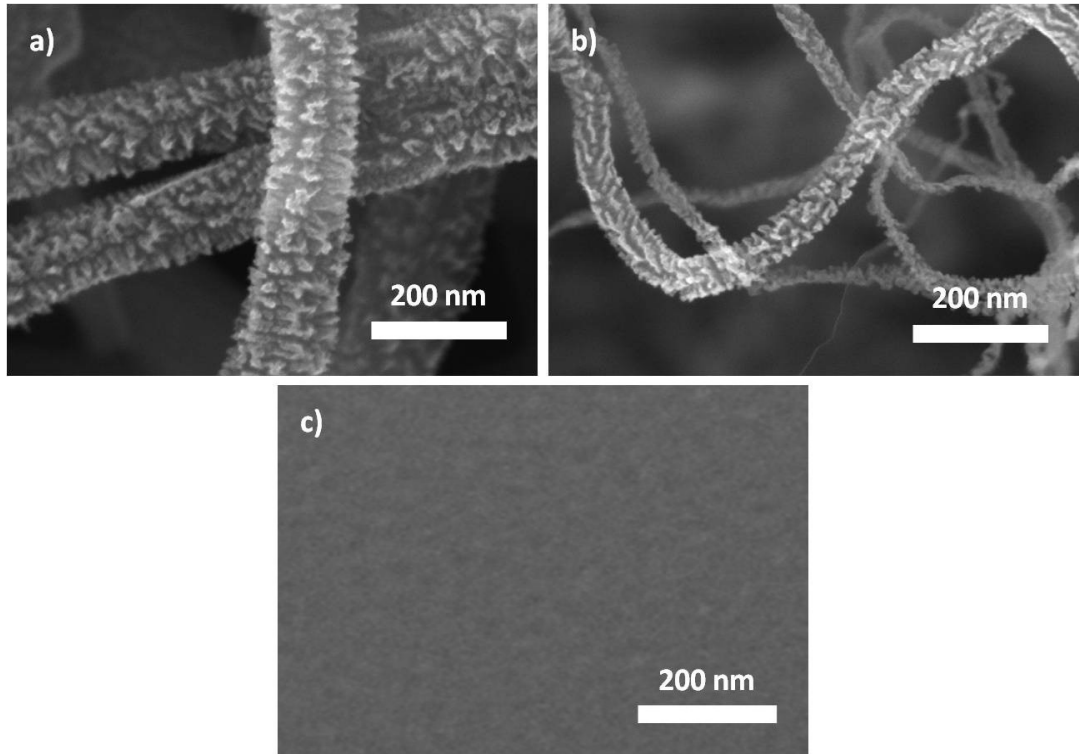


Figure 5.2.1 SEM of the $Pt-CeO_2$ thin film deposited on $MWCNTs$ (a), $CVD-CNTs$ (b) and the reference silicon wafer (c)

Fig. 5.2.2 shows the $Ce\ 3d$ spectra of the Pt doped cerium oxide film deposited on Si and the $CNTs$, respectively. The spectra are presented and fitted in the same way as described in *Section 5.1*. As was shown there, the high-resolution $Ce\ 3d$ core level HAXPES spectrum of the $Pt-CeO_2$ film deposited on the silicon substrate consists of three $3d_{5/2}-3d_{3/2}$ spin-orbit-split doublets f^0 , f^1 and f^2 that belong to stoichiometric CeO_2 and two small doublets of reduced ceria (dotted lines) where Ce atoms are in Ce^{3+} oxidation state (*Fig. 5.2.2(a)*) [38]. The CNT supported films (*Fig. 5.2.2(b, c)*) show the presence of strong Ce^{3+} -derived states at 885.6 and 880.8 eV (dotted lines). As in previous section, this strong Ce^{3+} states can be assigned to formation of oxygen vacancies on the $Pt-CeO_2$ surface or to purely electronic $Pt-Ce$ interactions. However, as you will see later the $Pt-Ce$ interactions does not play any substantial role in formation of the Ce^{3+} states while the surface oxygen vacancies is the main reason. The presence of strong Ce^{3+} -derived states at 885.6 and 880.8 eV indicates very high concentration of oxygen vacancies.

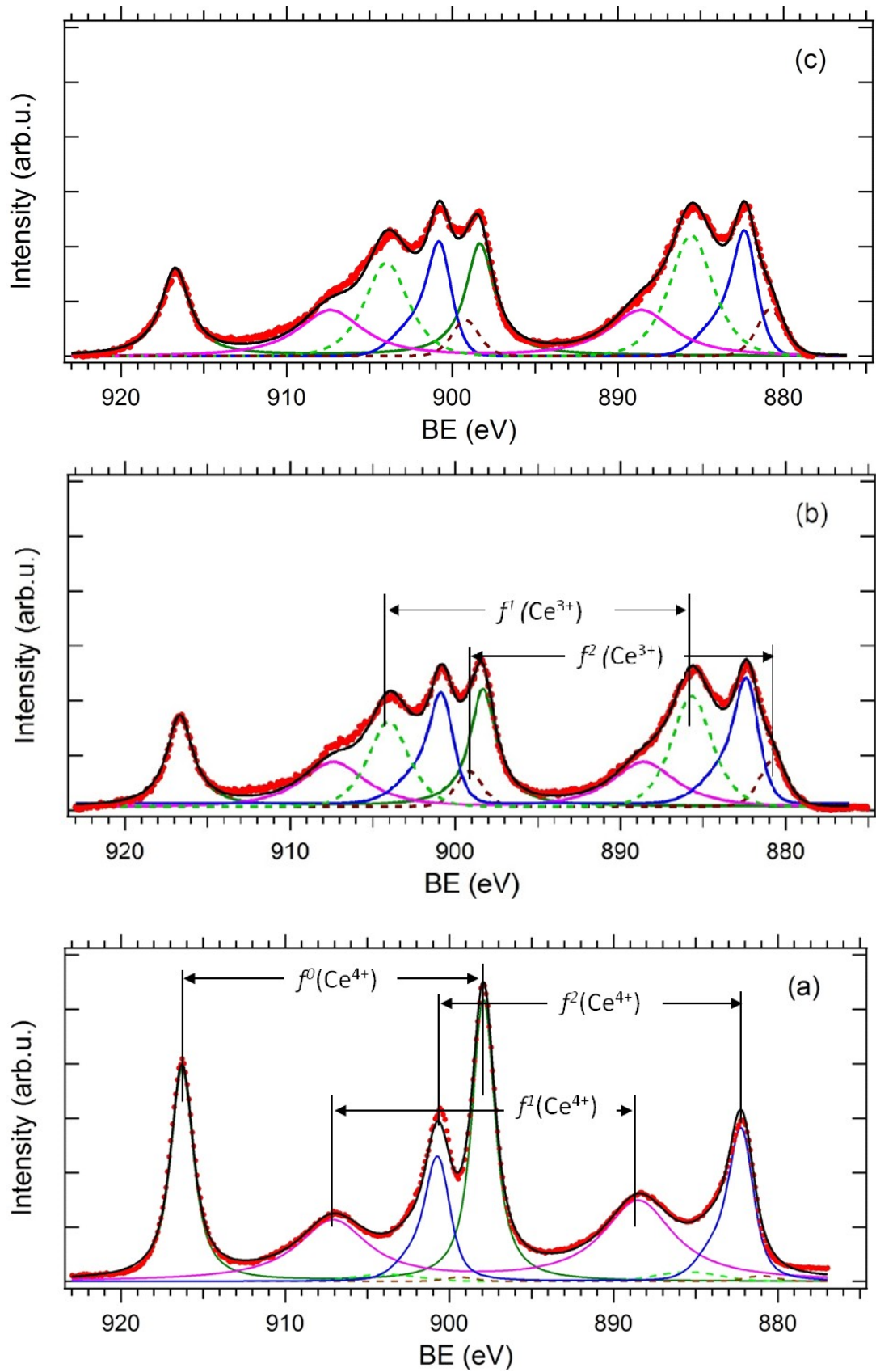


Figure 5.2.2. *Ce 3d* HAXPES spectra of the *Pt-CeO₂* films deposited on the *Si* wafer under normal (ND) incidence (a), *MWCNTs* (b), and *CVD-CNTs* (c).

In Fig. 5.2.3 are plotted corresponding *O 1s* core level HAXPES spectra of the *Pt-CeO₂* film deposited on the reference silicon substrate, *MWCNTs*, and *CVD-CNTs*. An intensive peak at about 529.6 eV which corresponds to the oxygen from *CeO₂* (*O-Ce⁴⁺*) is well seen in all spectra. As we know from Section 5.1 the peak at 530.3 eV corresponds to the “*Pt-Ce-O*” mixed oxide, while the peak appearing at 531.4 eV (marked *O-Ce³⁺*) can be assigned to formation of hydroxyl groups *OH* which are bonded to the *Ce³⁺* ions on the *Pt-CeO₂* surface. The presence of the strong peak at 531.4 eV in case of the *Pt-CeO₂* on the *CNTs* indicates presence of high concentration of the surface oxygen vacancies corresponding for the formation of *Ce³⁺* ions in agreement with the corresponding *Ce 3d* spectra. The peak at 533 eV belongs to molecular water that adsorbs on the extensive surface of the porous catalyst [53-56].

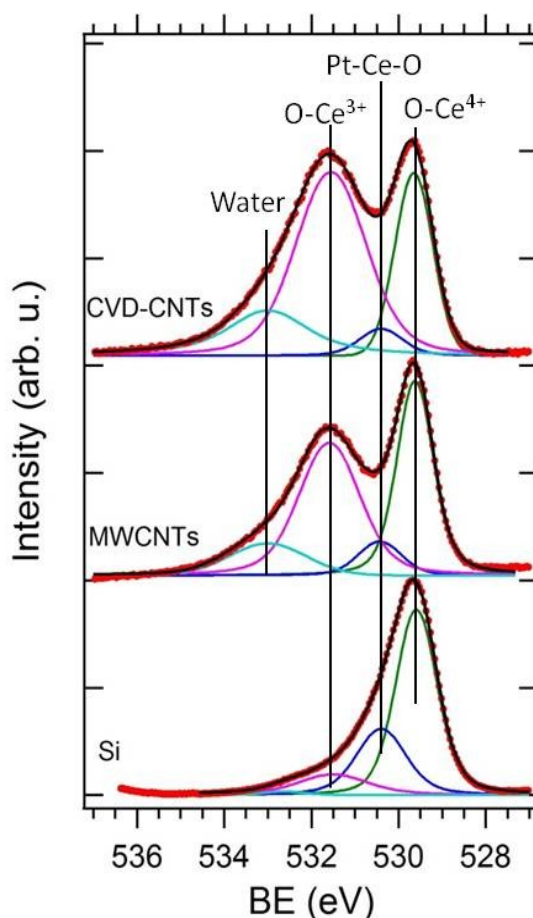


Figure 5.2.3. *O 1s* HAXPES spectra of *Pt-CeO₂* films deposited on the *Si* wafer, *MWCNTs* and *CVD-CNTs*.

In Fig. 5.2.4 we plotted the *Pt 4f* core level HAXPES spectra of the *Pt-CeO₂* thin film catalyst deposited on the reference silicon substrate, *MWCNTs* and *CVD-CNTs*. As it was shown in the previous section the catalyst film on the silicon wafer (Fig. 5.1.5(a)) exhibits two doublets: an intensive *Pt 4f_{7/2-4f_{5/2}}* doublet at 74.4-77.7 eV corresponding to *Pt⁴⁺* state of the “*Pt-Ce-O*” mixed oxide and a small *Pt 4f_{7/2-4f_{5/2}}* doublet with main peak energy at 73.3 eV assigned to formation of a small amount of *Pt-Ce* alloy. In case of the *Pt-CeO₂* catalyst on the CNTs the situation is completely different. The *Pt-CeO₂* film on the *CNTs* show four *Pt 4f_{7/2-4f_{5/2}}* doublets with main peak energies at 71.2, 72.3, 73.35 and 74.4 eV (Fig. 5.2.4(b, c)). As in the case of the catalyst deposited on the reference substrate, the small doublets at 74.4-77.7 and 73.5-76.9 eV can be assigned to “*Pt-Ce-O*” mixed oxide and *Pt-Ce* alloy. The state

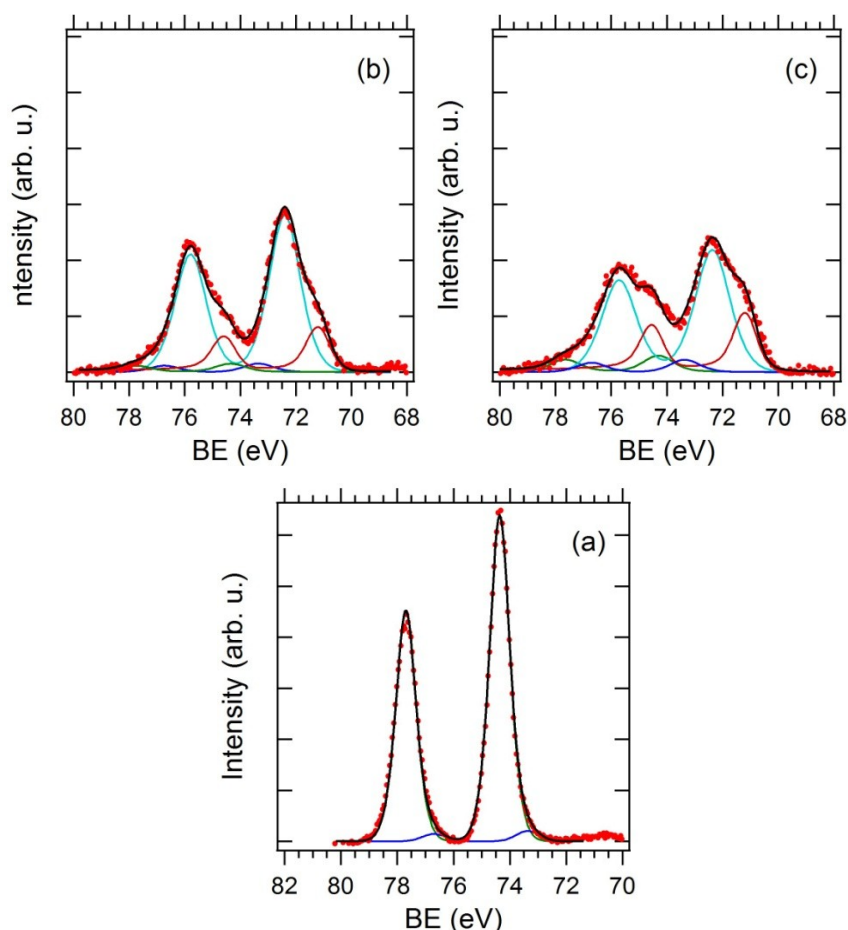


Figure 5.2.4. *Pt 4f* HAXPES spectra of the *Pt-CeO₂* films deposited on the *Si* wafer (a), *MWCNTs* (b) and *CVD-CNTs* (c).

with the main peak energy at 71.2 eV is supposed to be metallic Pt (Pt^0), while doublet with the main peak energy at 72.3 eV corresponds to Pt^{2+} state [62]. It can be seen that the Pt^0 peak in case of the *CVD-CNT* sample is quite intensive.

In order to check whether the porous surface structure of the $Pt-CeO_2$ catalyst on the *CNTs* is caused by Pt presence a reference 30 nm thick non-doped CeO_2 film was deposited and investigated on the same substrates. SEM measurements showed that the CeO_2 film deposited on the both kinds of *CNTs* have completely the same porous surface morphology as in case of $Pt-CeO_2$ (not shown).

The HAXPES $Ce\ 3d$ spectra of the reference CeO_2 film deposited on the *Si* wafer, *MWCNTs* and *CVD-CNTs* are presented in *Fig. 5.2.5*. As can be expected the non-doped CeO_2 film on the reference silicon substrate showed three $3d_{5/2}$ - $3d_{3/2}$ spin-orbit-split doublets (f^0 , f^1 and f^2) that belong to stoichiometric CeO_2 (*Fig. 5.2.5(a)*). The CeO_2 layer deposited on the *CNTs* gave almost the same $Ce\ 3d$ HAXPES spectra as in case of the $Pt-CeO_2$ film on the *CNTs* where the strong Ce^{3+} states are well seen (*Fig. 5.2.5(b, c)*). We can see that the presence of low concentration of Pt does not make any influence on reduction of ceria when compare $Ce\ 3d$ spectra of the non-doped CeO_2 film to $Ce\ 3d$ spectra of the $Pt-CeO_2$ film. The experiment without Pt partially answers the previous question about oxide reduction whether it is because of the vacancy formation or the charge transfer from Pt to Ce .

The SEM and HAXPES measurements of the reference CeO_2 film showed that the high porosity and reduction of the $Pt-CeO_2$ catalyst on *CNTs* is not caused by Pt doping but some other processes. One possible explanation of the huge reduction of the CeO_2 and $Pt-CeO_2$ films on the *CNTs* is a general effect of formation of defects and oxygen vacancies at oxide edges and steps on extended surfaces [63]. However, it was not clear why the both non-doped and doped ceria on the *CNTs* grew with highly porous structure. In order to explain it the main two differences between the flat *Si* substrate (wafer) and *CNTs* should be considered: their shape and material they are made of. By considering the cylindrical shape of *CNTs*, we came to conclusion that there can be an influence of different deposition angles. Indeed, in the case of the flat silicon substrate normal deposition (ND) is used while in the case of cylindrical substrates such as the *CNTs* a substantial part of the film grew at grazing incidence angle, i.e. at glancing angle deposition conditions (GLAD). Generally, GLAD deposition results in the formation of columnar nanostructured thin film due to the effect of ballistic shadowing between columns, while a normal

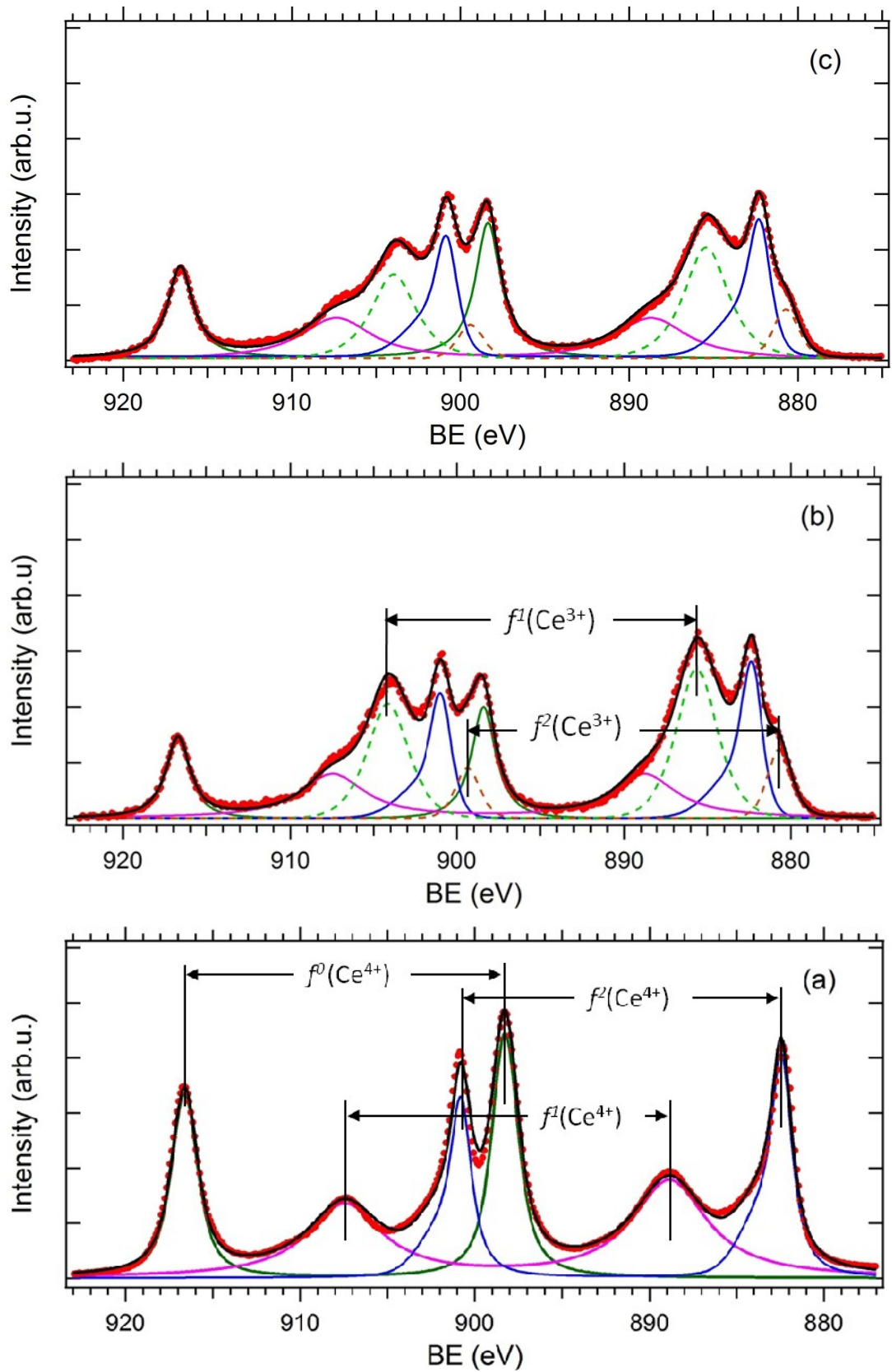


Figure 5.2.5. *Ce 3d* HAXPES spectra of the non-doped CeO_2 films deposited on the *Si* wafer (a), *MWCNTs* (b) and *CVD-CNTs* (c).

incidence deposition leads to the formation of dense films [64-67]. Therefore, it seems reasonable to expect a variation in the film morphology depending on the deposition angle as well as on the film thickness.

In order to support the suggestion about the deposition angle influence the *Pt-CeO₂* thin films were grown simultaneously on the *Si* wafer substrates placed in direction parallel and perpendicular to the sputtering target, i.e., at ND and GLAD conditions. The grazing angle of deposition was determined from the deposition distance and size of the circular sputtering target and it was smaller than 6 deg. The SEM images of the ND and GLAD samples are shown in *Fig. 5.2.6*. We can see substantial difference in surface morphology. The ND sample reveals homogeneous surface, whilst the GLAD sample surface is composed of grains that can be easily seen in the picture. The increase of the surface roughness suggests that grazing deposition leads to the formation of columnar, probably porous, structure of the film in agreement with previously published results [64-67]. However, if we compare *Fig. 5.2.1* and *Fig. 5.2.6*, it can be seen that the GLAD surface structure on the silicon substrate is still not as rough as that on the *CNTs*. It means that GLAD is obviously not the only single reason of growing such porous structures on the *CNTs*.

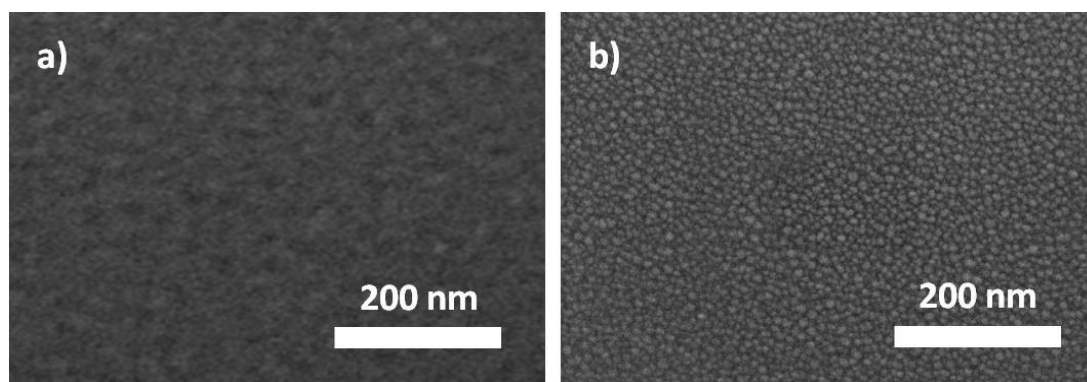


Figure 5.2.6. SEM image of the *Pt-CeO₂* films deposited on the *Si* substrate at (a) normal and (b) glancing angle depositions.

The *Ce 3d* and *Pt 4f* spectra of the *Pt-CeO₂* film prepared at GLAD condition are presented in *Fig. 5.2.7*. They show that GLAD on the *Si* wafer caused appearance of *Ce³⁺* and *Pt²⁺* sites which corresponded to a partial reduction of the *Pt-CeO₂*

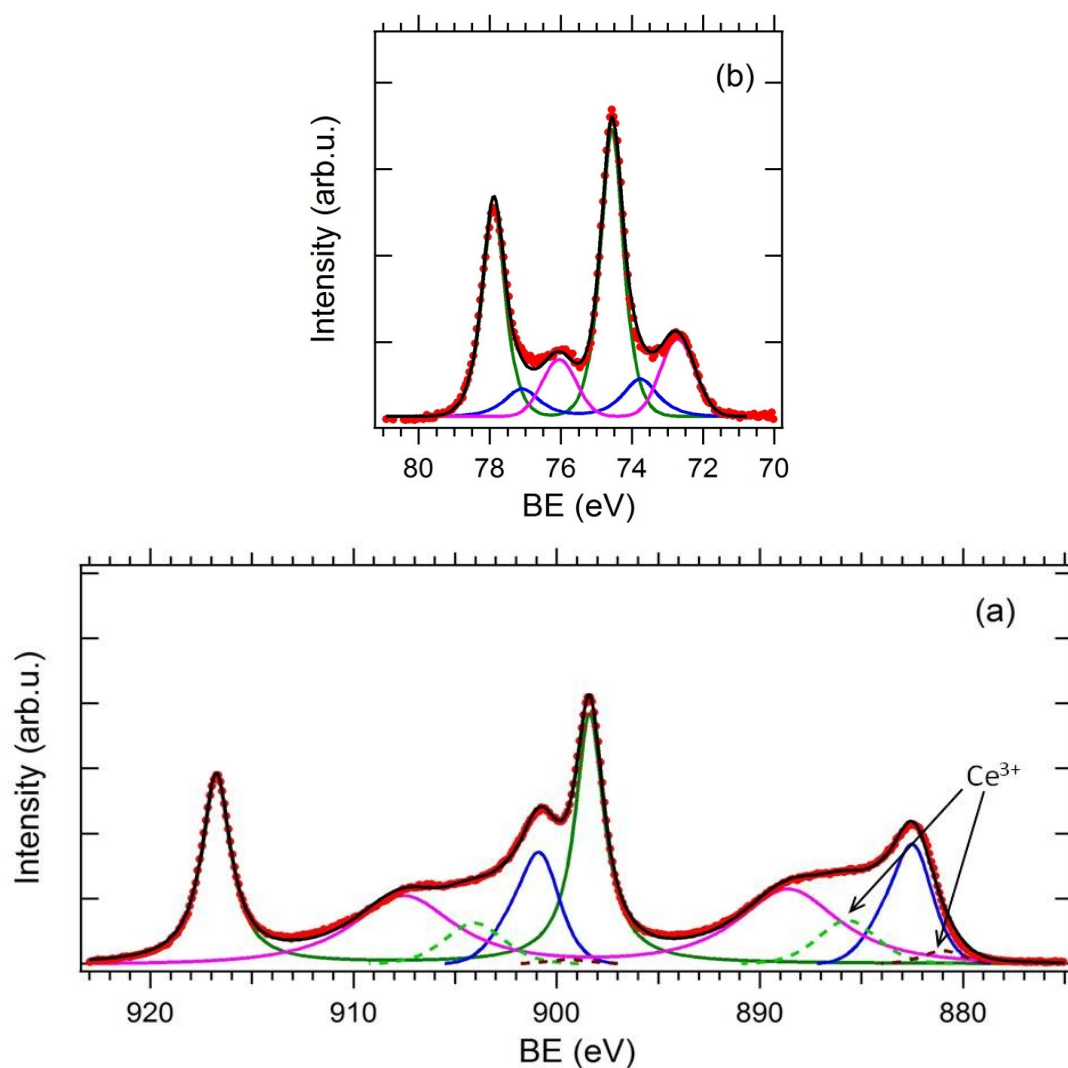


Figure 5.2.7. *Ce 3d* (a) and *Pt 4f* (b) HAXPES spectra of the *Pt-CeO₂* films deposited on the *Si* wafer under GLAD incidence.

film. These spectral features are the same as in case of the catalyst deposition on the *CNTs*, however less intensive. It should be mentioned that in the spectrum we do not see the peak of metallic *Pt* which was seen in *Fig. 5.2.4*.

By using areas of corresponding peaks the Ce^{3+}/Ce , Pt^{2+}/Pt and Pt^0/Pt concentration ratios were determined and presented in *Table 5.2.1* for all samples investigated in this experiment. The peak areas were calculated by the fitting program. The Ce^{3+} *3d* areas were obtained by summing areas of all Ce^{3+} peaks. We can see that the degree of reduction of cerium oxide increases in order $ND \rightarrow GLAD \rightarrow MWCNTs \rightarrow CVD - CNTs$.

Sample	Ce^{3+}/Ce	Pt^{2+}/Pt	Pt^0/Pt
<i>Pt-CeO₂/Si</i> , ND	0.03	0	0
<i>Pt-CeO₂/Si</i> , GLAD	0.06	0.19	0
<i>Pt-CeO₂/MWCNTs</i>	0.27	0.66	0.24
<i>Pt-CeO₂/CVD-CNTs</i>	0.34	0.55	0.32

Table 5.2.1. The Ce^{3+}/Ce , Pt^{2+}/Pt and Pt^0/Pt concentration ratios of the catalyst on the different substrates.

According to presented results we can conclude that nonporous film consists almost of Pt^{4+} and Ce^{4+} ions while Pt^{2+} and Ce^{3+} ions appear when the film porosity is increasing. Appearing of Ce^{3+} ions are associated with the formation of oxygen vacancies on the catalyst surface. As can be seen from *Table 5.2.1* an increase of the Ce^{3+} state concentration is accompanied by an increase of the Pt^{2+} state concentration. Therefore, it is suggested that Pt^{2+} ions also have some relation to the oxygen vacancies. Indeed, in case of the porous *Pt-CeO₂* catalyst on the *CNTs* there is an extensive catalyst surface which contains a lot of oxygen vacancies (the strong signals of Ce^{3+} ions in the *Ce 3d* and *OH* groups in the *O 1s* spectra). It is supposed that *Pt* atoms can segregate on the extensive surface of the porous film and stay there mostly in Pt^{2+} oxidation state or even form there metallic platinum particles. These suggestions are supported by the work of other authors [68]. It was shown that *Pt* dispersed over *CeO₂* by combustion method stay there mostly in Pt^{2+} and Pt^{4+} oxidation states and proposed that Pt^{2+} ions can be situated on the surface of *CeO₂* crystallites. On the other hand, Ce^{3+} cations could strongly interact with Pt^{2+} cations forming *Pt-O-Ce* bonds on the surface of reduced cerium oxide. This state is not visible in the corresponding *O 1s* spectra (*Fig. 5.2.3*), we see only signal of the mixed oxide formed by Pt^{4+} and Ce^{4+} ions. However it can be hidden by the strong “*O-Ce³⁺*” state. Formation of such *Pt-O-Ce* bonds on the reduced cerium oxide was observed by Hatanaka et al. [69], while the platinum oxide was spread out on the stoichiometric *CeO₂*. Therefore, the observed increase of the Pt^{2+}/Pt ratio for *CNTs* can be also explained by formation of Pt^{2+} and Ce^{3+} rich *Pt-O-Ce* clusters on the surface of the reduced cerium oxide inside the porous structure of the catalyst film.

The conclusion of this study is the *Pt-CeO₂* thin film catalyst deposited on *CNTs* shows the surprisingly porous surface morphology. The film is strongly reduced because contains a lot of the surface oxygen vacancies. The large surface of

the catalyst is one of possible reasons of its high catalytic activity. The *Pt* atoms are mostly in Pt^{2+} and Pt^0 states which means that the Pt^{2+} state is probably an active state that can be responsible for the high activity of the catalyst. However, this statement needs further investigation by other techniques. Calculations should be done in order to confirm this hypothesis. Another problem is that GLAD is not the only factor responsible for the porous growth of the catalyst film on *CNTs*. An interaction between sputtered *Pt-CeO₂* film and the surface of *CNTs* can not be excluded.

5.3. *Pt-CeO₂* thin film catalyst grown on flat carbon substrates

In previous section the study of the platinum-doped *CeO₂* catalyst deposited on the *CNTs* by magnetron sputtering was reported. It was shown that the catalyst films prepared by this method exhibited highly porous structure providing a large active surface of the catalyst. It was mentioned that the structure and stoichiometry of the catalyst film beside the dependence on angle of deposition should depend on a type of substrate. Thus further experiment was done when different flat carbon substrates were covered by the *Pt-CeO₂* catalyst using magnetron sputtering. The flat substrates were chosen to exclude the effect of GLAD and to investigate only the catalyst-substrate interaction. Therefore catalyst substrates as commercial graphite foil (C-foil), highly ordered pyrolytic graphite (HOPG), and glassy carbon plate (GC) were used. All of them were purchased from Alfa Aesar. C-foil was checked by AFM. The AFM measurements clearly showed hexagonal shallow atomically flat terraces of the hexagonal graphite structure. The depth of the craters was estimated to be 0.3 nm. These types of carbon substrates were chosen because carbon in a variety of forms is widely used as an electrode material and/or heterogeneous catalyst support in the field of electrocatalysis [70-73].

All substrates were covered simultaneously by 10 nm thick *Pt-CeO₂* thin films using magnetron co-sputtering from *CeO₂* and *Pt* targets in argon atmosphere. Chemical states and composition of the catalyst were investigated in the same way as in case of the *CNTs* by combining the laboratory XPS system with Al *K α* anode and

HAXPES with photon energy of 5956 eV. Morphology of the thin films was investigated by means of the SEM at 10 keV electron beam energy. The *Pt* concentration was the same as in the previous experiments with the *Pt/Ce* ratio of 0.18.

The SEM images of the carbon substrates coated by the *Pt-CeO₂* catalyst are presented in *Fig. 5.3.1*. It can be seen that all samples show porous surface morphology. Moreover, they reveal almost the same porous surface structure as in case of the coated *CNTs*, see *Section 5.2 (Fig. 5.2.1)*. High porosity of the films is given by a growth of well separated catalyst islands that have fractal like structure. The size of these islands is about 15 nm across and more that 50 nm lengthways, the islands are separated by about 25 nm wide gaps. If one looks at the images more precisely some differences between them can be noticed. We can see that the catalyst structure on the *GC* looks more fine-grained than the structures on the *C-foil* and *HOPG*.

The high-resolution *Ce 3d* core level HAXPES spectra obtained from the prepared samples are shown in *Fig. 5.3.2*. The spectra revealed strong *Ce³⁺* states

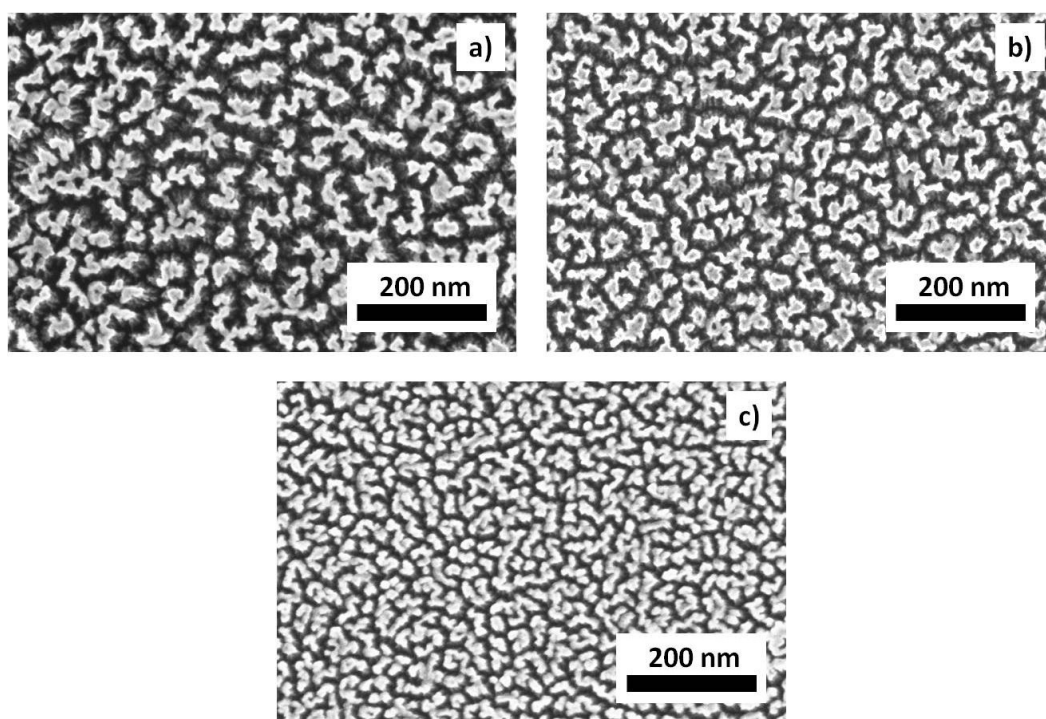


Figure 5.3.1. SEM images of the 10 nm thick *Pt-CeO₂* thin film deposited on the *C-foil* (a), *HOPG* (b), and *GC* (c).

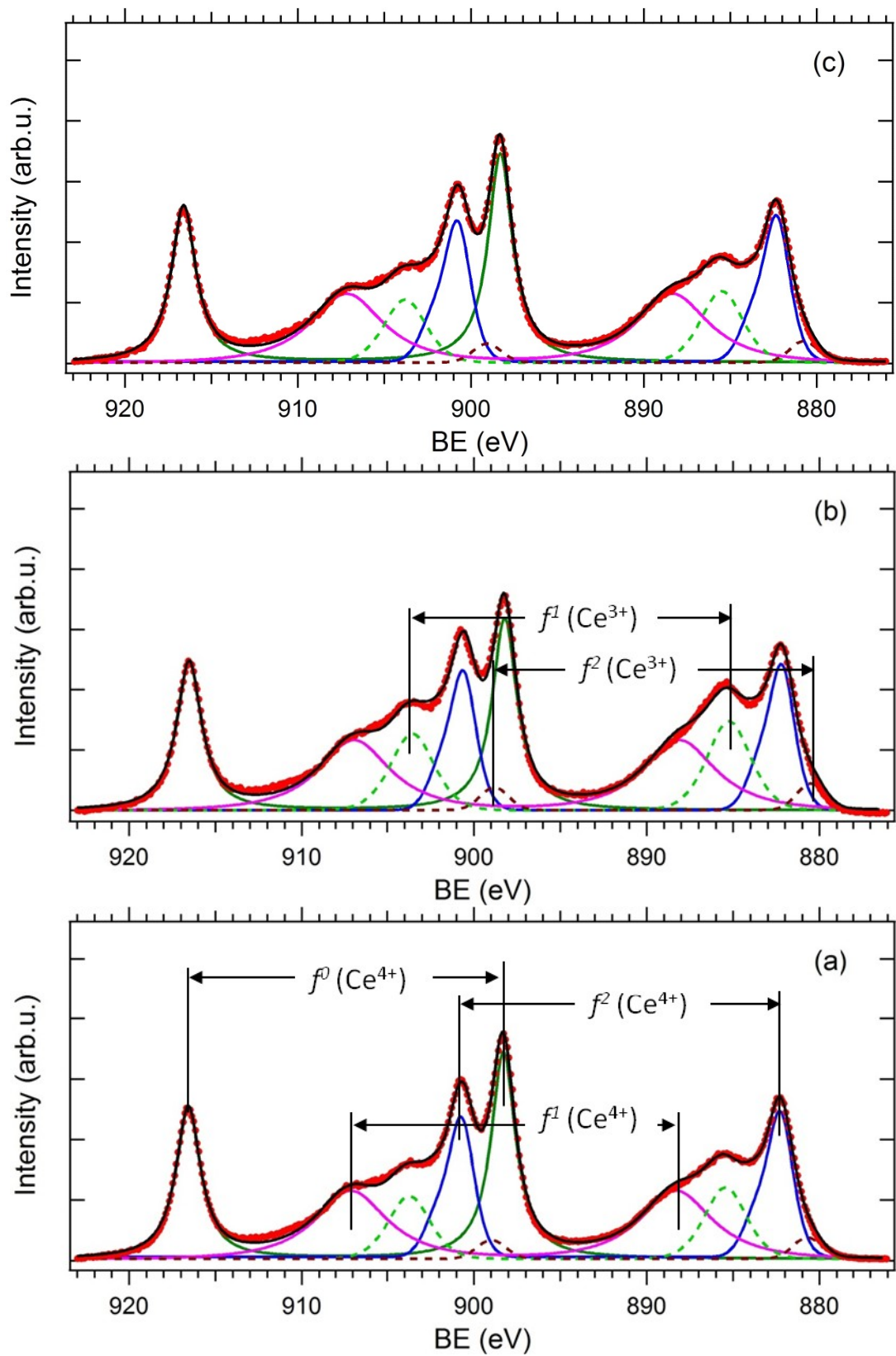


Figure 5.3.2. $Ce\ 3d$ HAXPES spectra of the 10 nm thick $Pt-CeO_2$ thin film deposited on the *C-foil* (a), *HOPG* (b), and *CG* (c).

corresponded to a partial reduction of cerium oxide. We can see that the film reduction was almost the same for all carbon substrates and just a little bit smaller than in case of the *CNTs* covered by *Pt-CeO₂* (see *Fig. 5.2.2*). Using the areas of the HAXPES peaks, the Ce^{3+}/Ce ratios were calculated and presented in *Table 5.3.1*.

The *O 1s* core level HAXPES spectra are shown in *Fig. 5.3.3*. Similarly to the *O 1s* spectra of the catalyst deposited on the *CNTs* (see *Fig. 5.2.3*), they consist of the main peak at about 529.5 eV corresponding to the oxygen from *CeO₂* (*O-Ce⁴⁺*) and the peak at 531.4 eV that can be assigned to the hydroxyl groups *OH* which are bonded to the oxygen vacancies on the *Pt-CeO₂* surface. The peak marked “*Pt-Ce-O*” corresponds to formation of the mixed oxide. The very small peak at about 533 eV

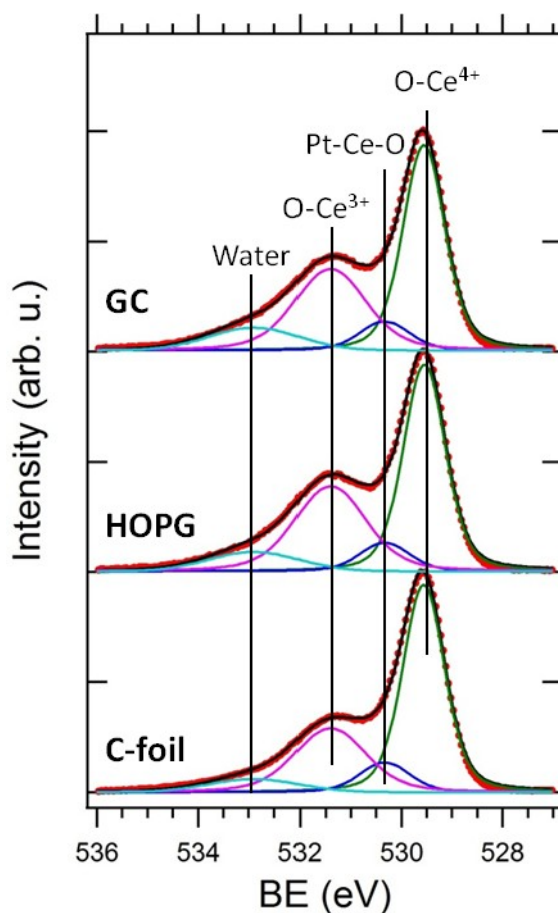


Figure 5.3.3. *O 1s* HAXPES spectra of the *Pt-CeO₂* thin film catalyst deposited on *C-foil* (a), *HOPG* (b), and *GC* (c).

belongs to molecular water adsorbed on the extensive surface of the porous catalyst. On all spectra the peak at 531.4 eV indicates, as expected, high concentration of oxygen vacancies in agreement with the *Ce 3d* spectra.

In Fig 5.3.4 the *Pt 4f* core-level HAXPES spectra measured on the *Pt-CeO₂* deposited on the different substrates are shown. According to our previous analysis of the *Pt 4f* HAXPES spectra (see Fig. 5.2.4), *Pt 4f_{7/2}-4f_{5/2}* doublets with main peak energies at 71.1, 72.5, and 74.3 eV can be assigned to *Pt⁰* (metal), *Pt²⁺* and *Pt⁴⁺*,

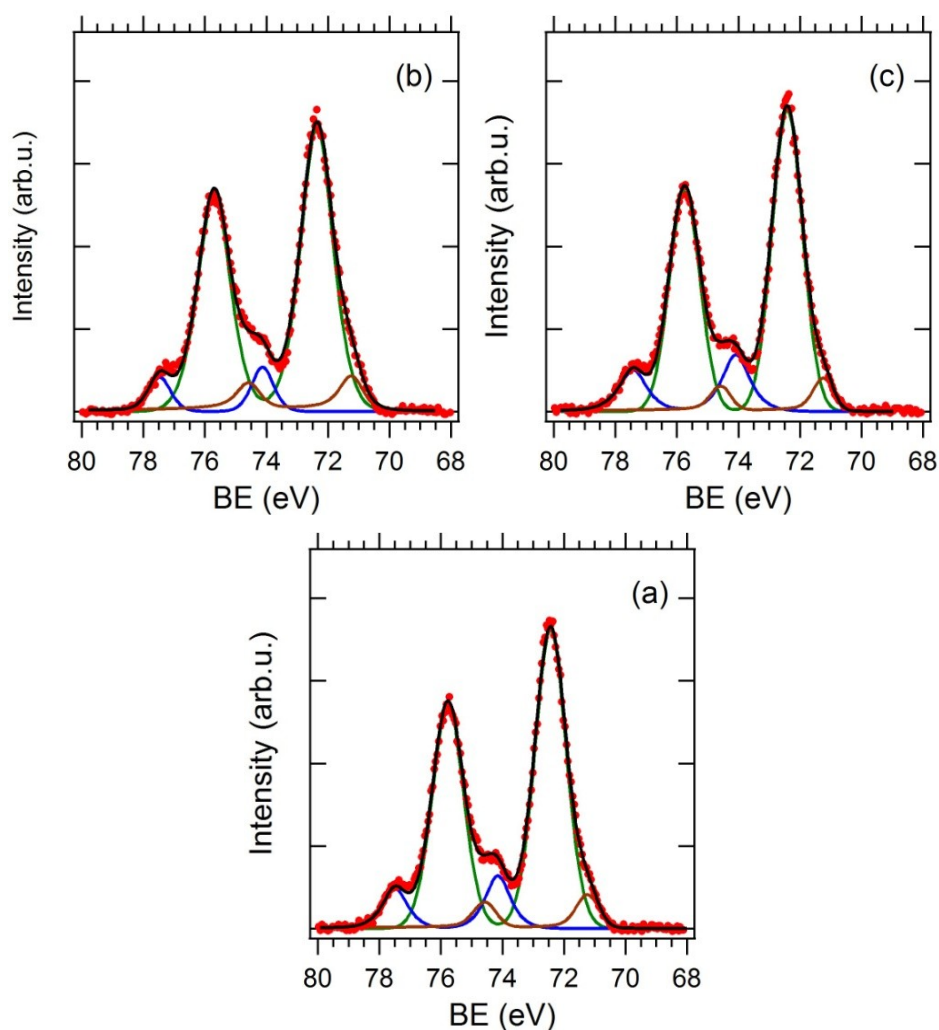


Figure 5.3.4. *Pt 4f* HAXPES spectra of the 10 nm thick *Pt-CeO₂* thin film deposited on *C-foil* (a), *HOPG* (b), and *GC* (c).

respectively. We can see that all carbon substrates show as in case of the CNTs strong Pt^{2+} peak and two small peaks for Pt^{4+} and Pt^0 . By using areas of the HAXPES peaks the Pt^{2+}/Pt and Pt^0/Pt ratios were calculated and presented in *Table 5.3.1*.

	Ce^{3+}/Ce	Pt^{2+}/Pt	Pt^0/Pt
<i>C-foil</i>	0.17	0.79	0.07
<i>HOPG</i>	0.21	0.82	0.09
<i>GC</i>	0.17	0.78	0.07

Table 5.3.1. The Ce^{3+}/Ce , Pt^{2+}/Pt and Pt^0/Pt concentration ratios of the catalyst on the different carbon substrates.

The presented results show that the catalyst film deposited on the all used flat carbon substrates revealed almost identical surface morphology and stoichiometry. Indeed, the ratios in *Table 5.3.1* are almost the same for different carbon substrates. Only in case of the catalyst on HOPG we see slightly different values. It means that the same processes leading to growth of the reduced porous films should take place on all carbon substrates during the $Pt-CeO_2$ film growth. In order to study the dependence of morphological and stoichiometric changes on the film thickness a 30 nm thick $Pt-CeO_2$ film was deposited on *C-foil*. In *Fig. 5.3.5* the SEM image of the catalyst film is shown using the same magnification as it was done for the 10nm thick films in *Fig. 5.3.1*. The change in the surface morphology after increasing the deposited thickness from 10 nm to 30 nm is noticeable by comparing this image and *Fig. 5.3.1(a)*. *Fig. 5.3.5* inset illustrates the film morphology obtained by the SEM of the film edge of the tilted sample and shows the columnar character of the catalyst deposition. The vertical structures are composed of bonded vertical nanorods forming together into a characteristic island structure. It can be seen that the heights of elemental nanorods are slightly dispersed and more than 30 nm in length due to the fact that the thickness of porous films is always higher than the effective thickness of the deposits as determined from the deposition rate obtained for non porous layers.

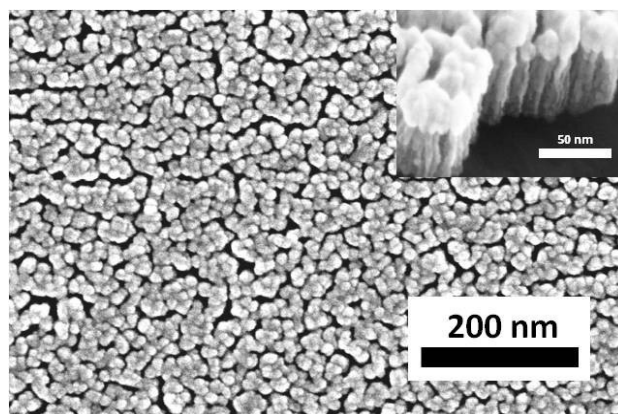


Figure 5.3.5. SEM images of the 30 nm thick $Pt-CeO_2$ thin film deposited on the C -foil.

The HAXPES $Ce\ 3d$ spectrum obtained from the 30 nm catalyst film deposited on C -foil is shown in Fig. 5.3.6(a). Comparison of this spectrum to the spectrum measured on the 10 nm $Pt-CeO_2$ film on graphite foil (Fig. 5.3.2(a)) shows a considerable decrease of the Ce^{3+} state intensity. Furthermore, when this sample was measured by the more surface sensitive laboratory XPS system with $Al\ K\alpha$ anode a very small Ce^{3+} signal was seen (Fig. 5.3.6(b)). It means that the catalyst film is more reduced in deeper parts towards the interface while top part of the film consists mainly of stoichiometric $Pt-CeO_2$. The Ce^{3+}/Ce ratios were calculated using areas of XPS and HAXPES $Ce\ 3d$ peaks and presented in Table 5.3.2. The same tendency can be seen in Fig. 5.3.7 where $Pt\ 4f$ spectra measured by HAXPES and XPS are presented. We can see that increase of the thickness caused disappearance of the metallic Pt^0 peak from the HAXPES spectrum. More surface sensitive XPS showed substantial increase of Pt^{4+} state intensity and decrease of Pt^{2+} state one. It can be clearly seen from the calculated Pt^{2+}/Pt and Pt^{4+}/Pt ratios in Table 5.3.2.

The HAXPES and XPS results showing dependence of Pt^{2+}/Pt and Ce^{3+}/Ce ratios on the film thickness point out that the films are more reduced in deeper parts, i.e. closer to the interface. Furthermore, the structure and stoichiometry are very similar to those obtained on the $CNTs$ and very different from those on the silicon substrate. In order to explain this behavior we can suppose that sputtered particles impinging the substrate are mainly neutral Ce , O and Pt atoms. On the reference silicon substrate adsorbed Ce and Pt atoms are oxidized by very active oxygen giving

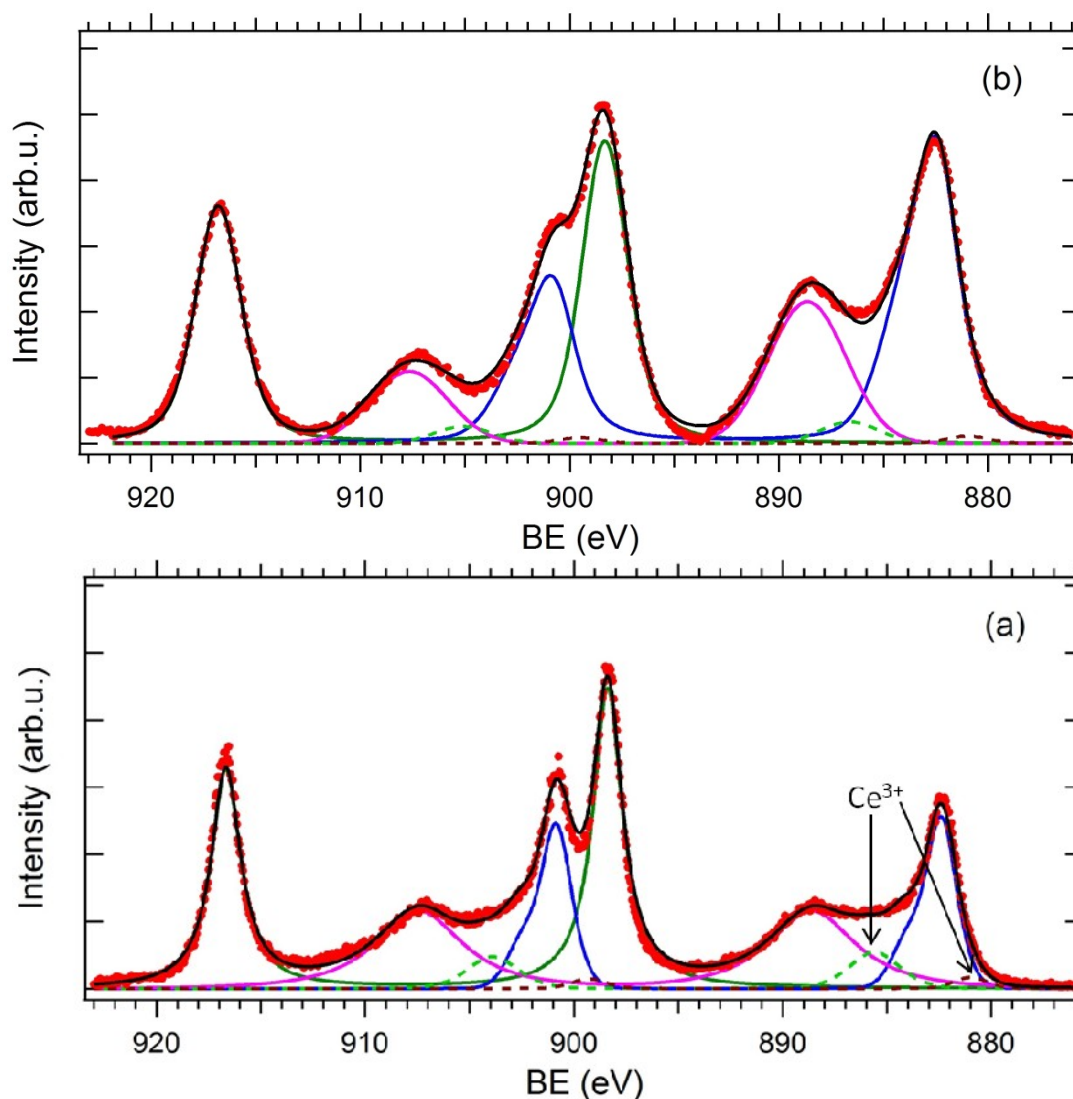


Figure 5.3.6. *Ce 3d* HAXPES (a) and XPS (b) spectra obtained from the 30 nm thick *Pt-CeO₂* thin film deposited on *C-foil*

the stoichiometric *Pt-CeO₂* film. On the other hand, the mechanism of catalyst film growth on carbon seems to be more complicated. There are many different growth mechanisms of columnar structures reported in literature. In most of them the initial surface roughness develops in fractal geometry which, due to atomic shadowing and limited surface diffusion, leads to extensive porosity [74-76]. However, in our case there is another effect which should be taken into account and which can explain both the formation of the porous structure and the film reduction. The film reduction closer to the interface in case of carbon substrates means that at the earlier stage of

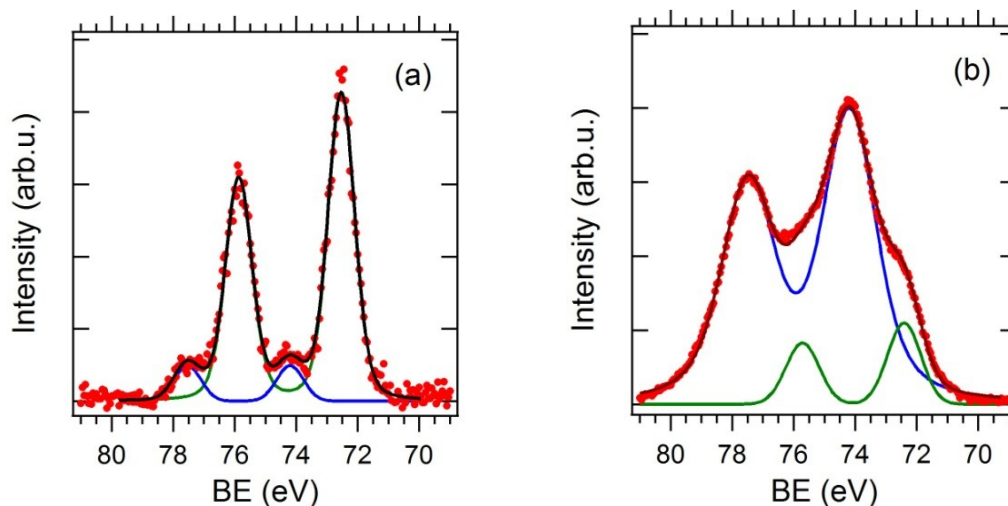


Figure 5.3.7. *Pt 4f* HAXPES (a) and XPS (b) spectra obtained from the 30 nm thick *Pt-CeO₂* thin film deposited on *C-foil*

	Ce^{3+}/Ce	Pt^{4+}/Pt	Pt^{2+}/Pt
HAXPES	0.08	0.11	0.89
XPS	0.01	0.72	0.28

Table 5.3.2. Ce^{3+}/Ce and Pt^{2+}/Pt concentration ratios for the 30 nm thick *Pt-CeO₂* film deposited on *C-foil* calculated by using HAXPES and XPS spectra.

the film growth there should be a lack of oxygen. The lack of oxygen can be caused by the process of oxygen plasma etching. The carbon surface is etched by oxygen plasma generated by the magnetron. A large amount of oxygen atoms interact with the carbon surface forming *CO* and/or *CO₂* molecules with their further desorption, while some remaining oxygen together with the *Ce* and *Pt* atoms form the reduced *Pt-CeO_x* layer. Explanation of the porous growth can be based on a suggestion that initially there is formation of 3 dimensional *Ce-Pt-O* nuclei distributed on the carbon surface creating something like a mask, while uncovered spaces between these nuclei are etched by oxygen plasma. Consequently, due to higher accessibility of impinging cerium atoms to 3D structures, pillars of cerium oxides are grown resulting in the porous columnar structure of the film.

In order to prove the above hypothesis the *Pt-CeO₂* film covering the carbon substrate was dissolved out in *HCl* acid. It was found that the bare graphite surface

(where no $Pt-CeO_2$ was seen by XPS) revealed very similar surface morphology to that of $Pt-CeO_2$ coating structure. This means that the deposit is copying the substrate structure engraved by the plasma. Furthermore, the non treated graphite foil was exposed to pure oxygen plasma in order to investigate the plasma interaction with the carbon substrate. The SEM image of this plasma treated surface is shown in *Fig. 5.3.8*. We can see that the surface morphology after plasma treatment is similar to that obtained during the magnetron deposition of $Pt-CeO_2$ on graphite. For further investigation a part of clean carbon surface was masked by a droplet of varnish and such sample was placed into oxygen plasma. After removing the varnish, formation of a step between non-etched (masked by varnish) and etched carbon surface was observed. The amount of material etched away during the treatment depended on plasma parameters and it was in range of nanometers per minute.

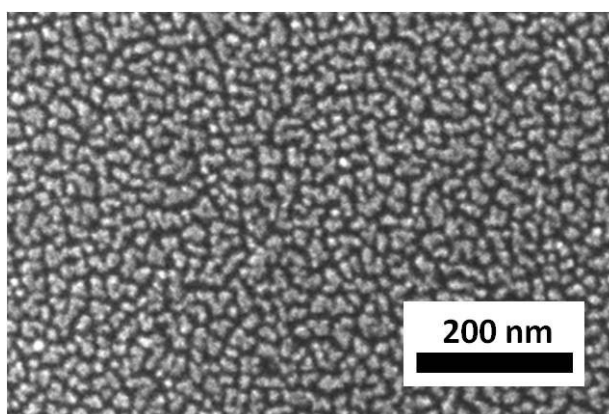


Figure 5.3.8. SEM image of the oxygen plasma treated *C-foil*.

Based on the experimental results we can conclude that the catalyst with high porous surface morphology can be prepared on different carbon surfaces. Therefore it is possible to cover other materials by a carbon film using different techniques and to grow on them the porous $Pt-CeO_2$ catalyst. It can be used, for example, in the planar silicon based on-chip μ -FC, where highly active catalysts with large surface area are required.

5.4. Interaction of sputter deposited CeO_x thin films with silicon oxide

Mobile electronic devices, including those for communication, microsensors and micro-electromechanical systems (MEMS), are increasingly considered as an integral part of modern society. Their proliferation is significantly accelerated by a remarkable progress in the development of smart devices for everyday use. However, such systems also require rapid development of suitable energy storage, despite all efforts to reduce their power consumption. Hence, microfabricated silicon-based FCs represent a highly attractive new type of power source with outstanding potential [77, 78]. RF-magnetron sputtering is technologically the most suitable method of preparation of such systems. As was mentioned in previous sections the ionic Pt^{n+} -doped nanoporous CeO_2 films deposited by magnetron co-sputtering is a very perspective catalyst for fuel cell applications. As we mentioned above, this catalyst can be prepared on a flat carbon covered substrate. It is also possible to deposit this catalyst directly on nanoporous silicon without using carbon; however the film growth is strongly influenced by the interaction of Ce atoms with the substrate and their oxidation by oxygen containing RF plasma. Therefore, it was very important to investigate carefully an interaction of reactive magnetron sputtered cerium oxide with silicon substrate.

In the previous experiments the native-oxide covered $Si (001)$ wafer was considered to be a truly chemically inert reference substrate because neither the $Ce 3d$ nor $Pt 4f$ HAXPES spectra indicated any film-substrate chemical interaction between the $Pt-CeO_2$ thin film and the $Si (100)$ substrate. However, in those experiments the film thicknesses was around 30 nm and it was very difficult to register some film- Si substrate interaction even using HAXPES. Therefore, further experiment was done where only 1 and 3 nm thick CeO_x films were deposited on two different types of silicon substrate. The only CeO_x was investigated instead of $Pt-CeO_x$ because we expected that the small concentration of Pt did not influence an interaction between the CeO_x film and the silicon substrate.

Cerium oxide thin films 1 and 3 nm thick were deposited simultaneously on the SiO_2 oxide substrate grown on the Si wafer by thermal annealing in air mimicking bulk silicon oxide and on the $Si (100)$ covered by thin native SiO_2 oxide pre-cleaned in the ultrasonic

bath, hereafter named $b\text{-SiO}_2$ and $n\text{-SiO}_2$, respectively. The $b\text{-SiO}_2$ substrate was prepared by heating at 1150 °C for 50 minutes. HAXPES measurements showed that no Si signal was detected confirming that oxide thickness was higher than 35 nm by considering inelastic mean free path of Si 2s emitted electrons 11.5 nm [79] and the depth detection limit as a three time multiple of this value.

The HAXPES $Ce\ 3d$ spectra of 1 and 3 nm thick cerium oxide films deposited on $b\text{-SiO}_2$ substrate are presented in *Fig. 5.4.1*. $Ce\ 3d$ spectrum consists of the three $3d_{5/2}\text{-}3d_{3/2}$ spin-orbit-split doublets characteristic (f^0 , f^1 , and f^2) of Ce^{4+} (CeO_2) states and two doublets (f^1 and f^2) of Ce^{3+} (Ce_2O_3). Detailed description of the $Ce\ 3d$ spectra fitting procedure is described in *Section 2.2.3*. For better clarity all Ce^{4+} and Ce^{3+} doublets are summarized in total Ce^{4+} (blue line) and Ce^{3+} (green line) spectra. The figure clearly shows that the film 3 nm thick is only slightly reduced (*Fig. 5.4.1(b)*) whilst 1 nm film is reduced substantially (*Fig. 5.4.1(a)*). Moreover the 1 nm ceria spectrum reveals two f^1 (Ce^{3+}) doublet at 885.2 eV and 886.8 eV. It should be noted that such split of the f^1 (Ce^{3+}) states is not observed in the case of reduced pure cerium oxide [37, 80]. It suggests that in this case we are observing three Ce^{3+} components instead of two typical for reduced cerium oxide [37].

In *Fig. 5.4.2* corresponding $O\ 1s$ spectra together with that of the pure $b\text{-SiO}_2$ sample are plotted. We can distinguish 4 peaks. The peak at 532.75 eV corresponds to SiO_2 (marked $O\text{-}Si^{4+}$) because it is a unique peak of the $b\text{-SiO}_2$ $O\ 1s$ spectrum (denoted as “0 nm”). 1 nm thick cerium oxide film shows 3 additional peaks. One of them (529.75 eV) can be associated to oxygen bounded to Ce^{4+} cations in stoichiometric ceria. The peak appearing at 531.3 eV corresponds to $O\text{-}Ce^{3+}$ bond of reduced cerium oxide [37]. We should note that appearance of this peak is typical for ex situ prepared reduced ceria or for reduced ceria exposed to water, i.e. oxygen bound to Ce^{3+} is supplied by hydroxyl groups. The new peak observed after cerium oxide deposition at 530.6 eV does not belong to pure cerium oxide CeO_x and is called “ $O\text{-}Si\text{-}Ce$ ”. Areas of the $O\text{-}Si^{4+}$ and $O\text{-}Si\text{-}Ce$ $O\ 1s$ peaks and areas of the Ce^{4+} , Ce^{3+} doublets of the $Ce\ 3d$ spectra are plotted in *Table 5.4.1*. We can see that the $O\text{-}Si\text{-}Ce$ peak intensity decreased with increasing thickness which showed that this species were located at the CeO_x/SiO_2 interface and photoemission signal was

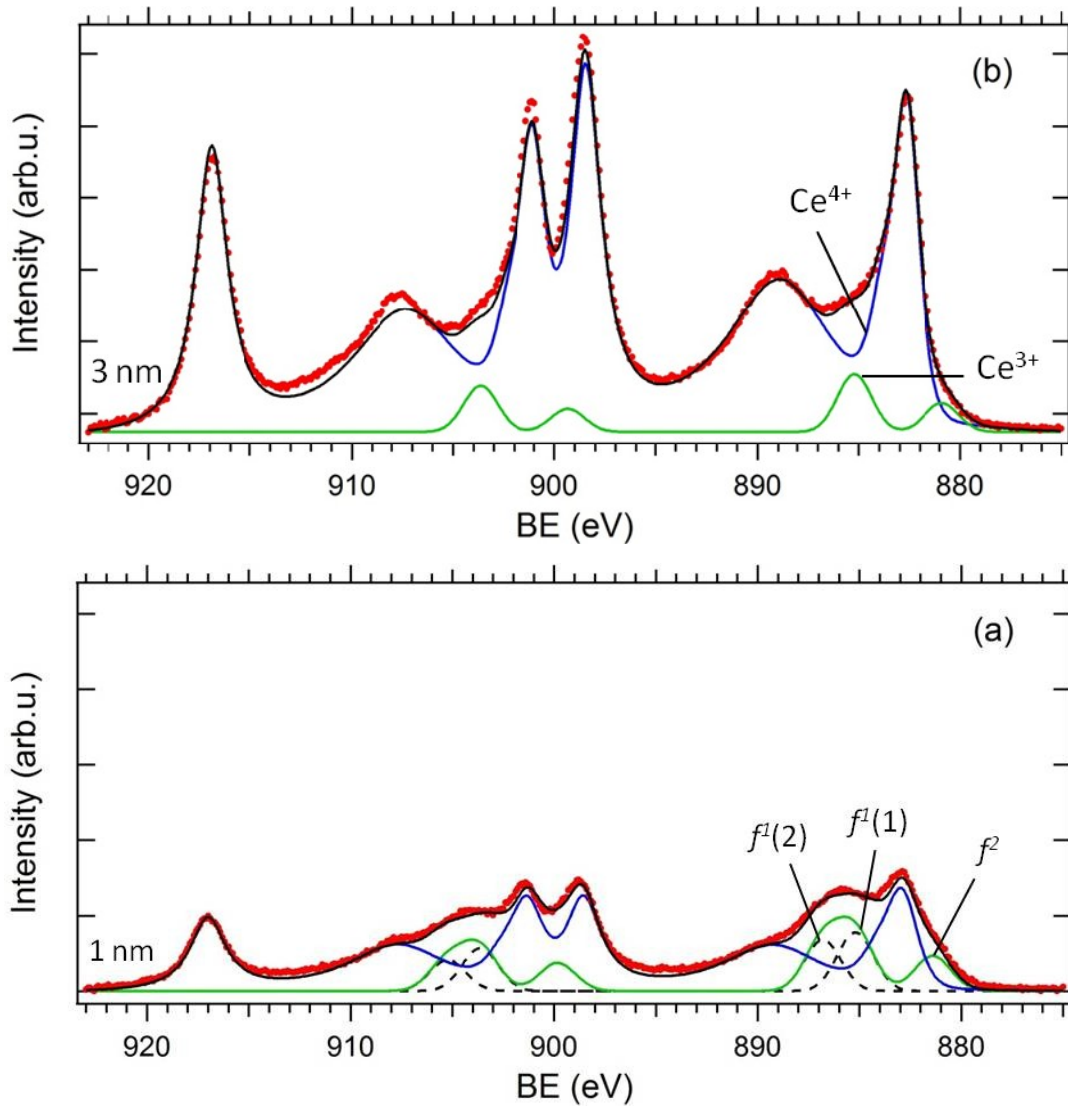


Figure 5.4.1. HAXPES Ce 3d spectra of the 1 nm thick (a) and 3 nm thick (b) cerium oxide thin films grown on b-SiO₂ substrate.

attenuated by the growing CeO_2 overlayer. Therefore we can associate this peak with an interfacial $O-Si-Ce$ mixed oxide. In principle this state might also be associated with reduced silicon oxide SiO_x ($x < 2$) however it does not seem possible because $O 1s$ BE of silicon suboxides is generally higher than 532 eV [81-83]. Similarly the $O-Si^{4+}$ intensity decreased with increasing film thickness due to CeO_2 growth, see Table 5.4.1.

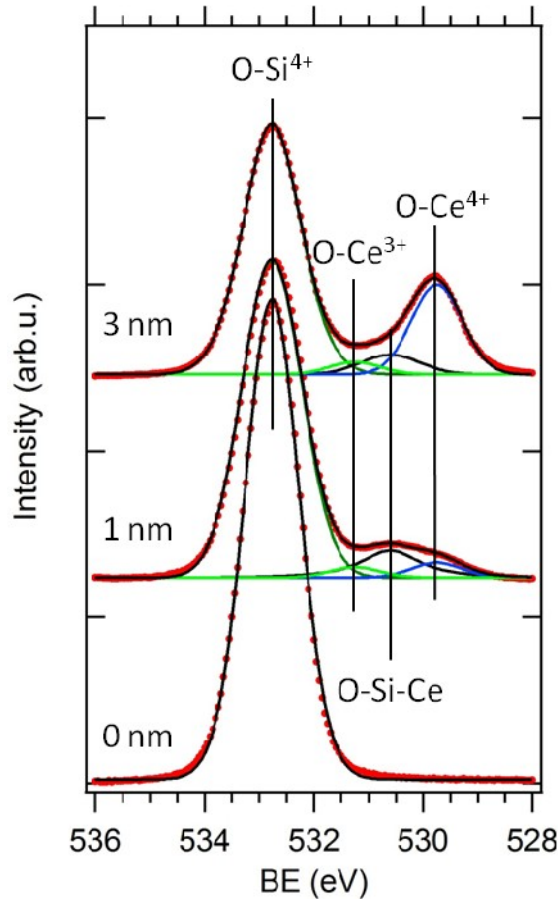


Figure 5.4.2. HAXPES $O 1s$ spectra of the 3 and 1 nm thick cerium oxide thin films grown on $b\text{-SiO}_2$ substrate. 0 nm denotes spectrum obtained for the non-coated substrate.

	Ce^{4+}	Ce^{3+}	$O\text{-Si}^{4+}$	$O\text{-Si-Ce}$
1 nm	20458	7343	26283	2745
3 nm	66775	4519	20407	1667

Table 5.4.1. Areas of the Ce^{4+} and Ce^{3+} $Ce 3d$ peaks and of the $O\text{-Si}$ $O 1s$ peaks measured from 1 and 3 nm thick CeO_2 film on the $b\text{-SiO}_2$ substrate.

If we compare the Ce^{3+}/Ce^{4+} concentration ratios determined for both thicknesses using values shown in Table 5.4.1, 0.36 and 0.06 respectively, we can see that the concentration ratio decreased six times, i.e. the thinner film was more reduced. The similar relative decrease reveals also $O\text{-Si-Ce}$ peak intensity, see in Fig. 5.4.2 and Table 5.4.1. This similar decrease of intensity, together with substantial

disappearance of the Ce^{3+} "extra" state at 886.8 eV in *Fig. 5.4.1*, confirm the hypothesis that *O-Si-Ce* mixed oxide is formed at the *Si/SiO₂* - cerium oxide film interface providing *Ce 3d* " Ce^{3+} extra" peak and *O 1s* "*O-Si-Ce*" peak, respectively. The mixed oxide should be cerium silicate, e.g. Ce_2SiO_5 and $Ce_2Si_2O_7$, [84, 85] or $CeSiO_3$ [86]. Two doublets f^1 (1) and f^2 in *Fig. 5.4.1*, typical for reduced cerium oxide, are due to formation of oxygen vacancies on the surface of nano-size grains of polycrystalline sputtered film. Progressive decrease of the oxygen vacancy concentration in top part of the deposit with deposit thickness can be explain by an increase of average grain size with film thickness which was observed by atomic force microscope and scanning electron microscopy.

Fig. 5.4.3 shows an evolution of the *Si 2s* peaks with thickness of the cerium oxide layer deposited on the *b-SiO₂* substrate. The only one peak that can be seen on all spectra corresponds to Si^{4+} (SiO_2) specie (BE= 154.4 eV). This peak is very strong even in case of 3 nm thick CeO_2 film on the *b-SiO₂* substrate due to high analyzing depth of HAXPES. The *O-Si-Ce* mixed-oxide state is not seen on the both ceria covered samples, however, as it will be shown below this peak should be seen somewhere at energy of 156 eV and its intensity supposed to be quite low so that it can be hidden by the Si^{4+} peak.

In the second part of the experiment the cerium oxide films, 1 and 3 nm thick as in the case of the *b-SiO₂* sample, deposited on the silicon wafers covered by native oxides (*n-SiO₂*) were investigated. Identical character of the ceria films were ensured by simultaneous deposition on both types of substrates, i.e. thin films have been grown exactly at same conditions for the same time.

In *Fig. 5.4.4* the *Si 2s* peaks obtained for both cerium oxide deposits and for the bare substrate are compared. The main peak at BE of 151.1 eV belongs to bulk *Si* (Si^0) which is now detectable because of very thin oxide overlayer. The Si^0 peak intensity is bigger for the bare substrate and decreases with increasing ceria thickness. The *Si 2s* peaks at 154.4 eV correspond to silicon native oxide. The peak is at the same position as the main peak in *Fig. 5.4.3* showing that native oxide also has SiO_2 stoichiometry. The third peak develops at 155.8 eV at higher BE than that of SiO_2 which signifies that a new strong bond is formed which should be that of *Si-Ce*. Therefore we can associate this state to some cerium silicate. In *Fig. 5.4.4* a zoomed figure is inset for better resolving the peaks at higher binding energies.

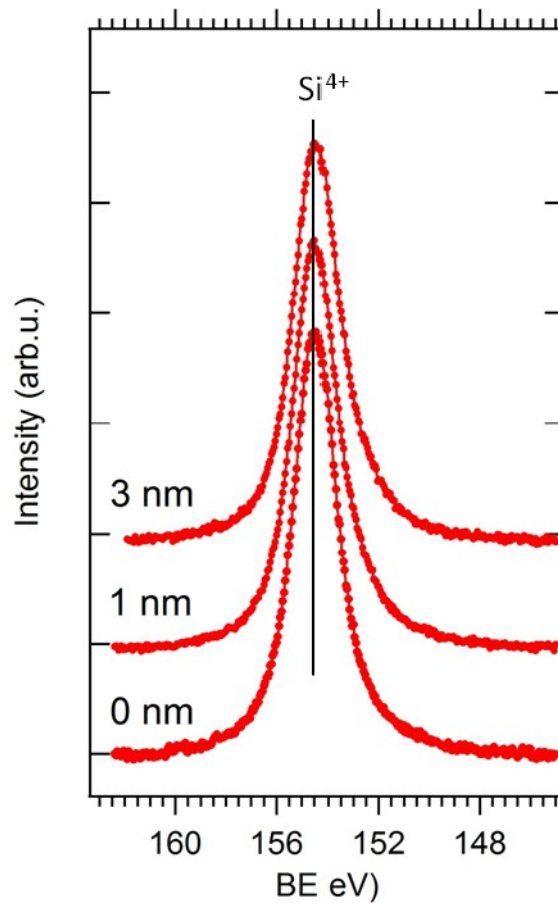


Figure 5.4.3. HAXPES *Si 2s* spectra of the 3 and 1 nm thick cerium oxide thin films grown on *b-SiO₂* substrate.

O 1s spectra of bare and cerium oxide covered *n-SiO₂* substrate in Fig. 5.4.5 can be fitted using exactly the same fitting parameters (BE, width, shape) as used above for *O-Ce⁴⁺*, *O-Ce³⁺*, *O-Si⁴⁺* and *O-Si-Ce* oxygen states in Fig. 5.4.2, and adding one more peak at 532.1 eV. Therefore, we can conclude that *CeO₂*, *Ce₂O₃*, *SiO₂* and silicate species are formed for both *n-SiO₂* and *b-SiO₂* substrates. In Fig. 5.4.5 we can see that *O-Ce⁴⁺* peak area increases with the cerium oxide film thickness relative to that one of *O-Ce³⁺* showing that thicker film was mostly composed of *CeO₂* in the same way as in the case of the *b-SiO₂* substrate in Fig. 5.4.2. Similarly to the *b-SiO₂* sample case, the *O-Si-Ce* intensity, marked (O-Si-Ce)A in Fig. 5.4.5, reveals net decrease with increasing film thickness due to its

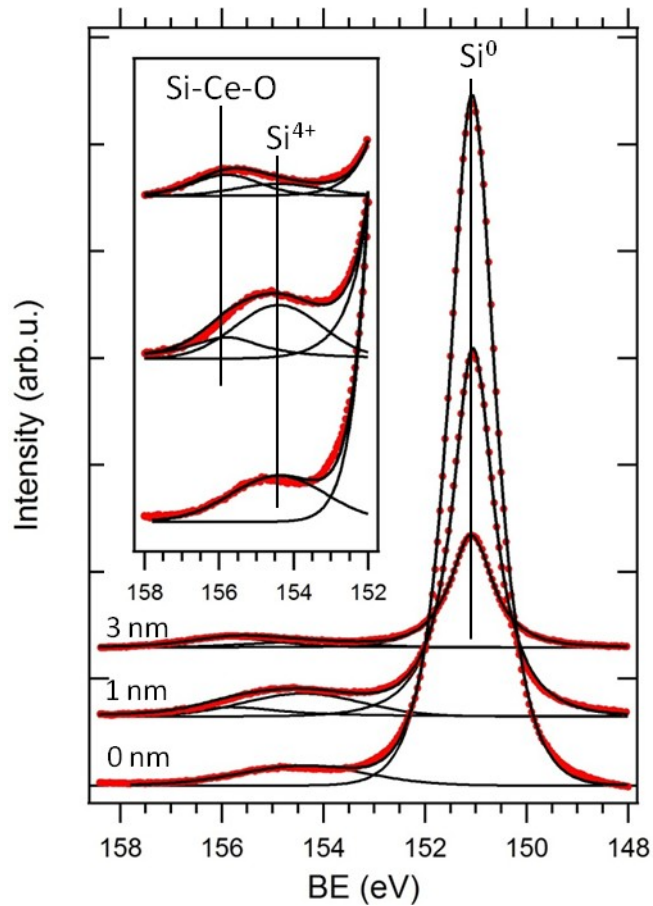


Figure 5.4.4. HAXPES Si 2s spectra of the 3 and 1 nm thick cerium oxide thin films grown on the n-SiO₂ substrate.

interfacial character. The new feature at 532.1 eV is the most intense for 1 nm deposit relative to all other oxygen species. This feature can be associated with formation of another silicate, marked as $(O-Si-Ce)B$. A relative slow decrease of intensity of this peak with the deposit thickness indicates that these species are not located at the interface. This oxygen chemical state can be associated with formation of new phase formed by the Si atoms diffusing from Si through very thin and partially reduced SiO₂ barrier into the growing cerium oxide film (not observed in the case of the b-SiO₂ sample). Fig. 5.4.5 shows that for 1 nm ceria film substantial part of oxygen atoms is contained in silicate species. With increasing thickness of the cerium oxide film the relative intensity of this peak decreases in profit of $O-Ce^{4+}$ showing that the thicker layer cerium oxide become more stoichiometric with silicate located in deeper part of the film. It can be well explained by limited diffusion length

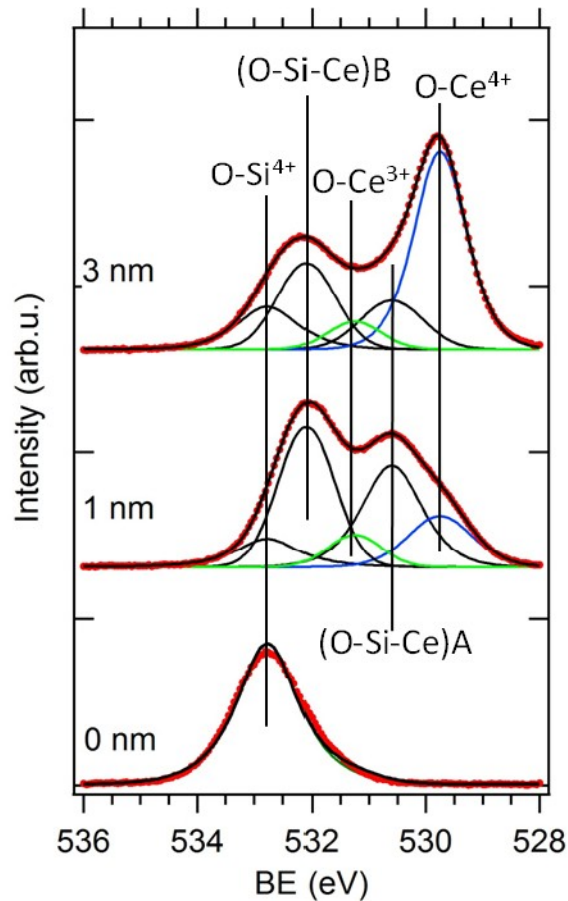


Figure 5.4.5. HAXPES O 1s spectra of the 3 and 1 nm thick cerium oxide thin films grown on the n-SiO₂ substrate. 0 nm denotes spectrum obtained for the non-coated substrate.

of Si in the growing cerium oxide film. Fig. 5.4.5 also shows a decrease of the O 1s intensity of SiO₂ for 3 nm relative to the 1 nm thick film. This is due to the location of SiO₂ species in form of thin layer of native oxide at the interface only. Areas of all oxygen peaks discussed above together with areas of the Ce⁴⁺, Ce³⁺ doublets of the Ce 3d spectra determined for the n-SiO₂ samples are reported in Table 5.4.2.

Ce 3d spectra of cerium oxide films grown on n-SiO₂ substrates are presented in Fig. 5.4.6. The spectra were fitted in the same way as those of Fig. 5.4.1. Decomposition in Ce⁴⁺ and Ce³⁺ components shows again a partial reduction of cerium oxide in the case of the 3 nm thick film and a strong reduction in the case of the 1 nm ceria film. Concentration ratios Ce³⁺/Ce⁴⁺ determined from Ce 3d spectra

	Ce^{4+}	Ce^{3+}	$O-Si^{4+}$	$(O-Si-Ce)A$	$(O-Si-Ce)B$
1 nm	26895	16144	1748	4213	4823
3 nm	75087	6095	1094	2055	4283

Table 5.4.2. Areas of the Ce^{4+} and Ce^{3+} Ce 3d peaks and $O-Si^{4+}$ and $O-Si-Ce$ O 1s peaks measured on 1 and 3 nm thick CeO_2 films supported by the n- SiO_2 substrate.

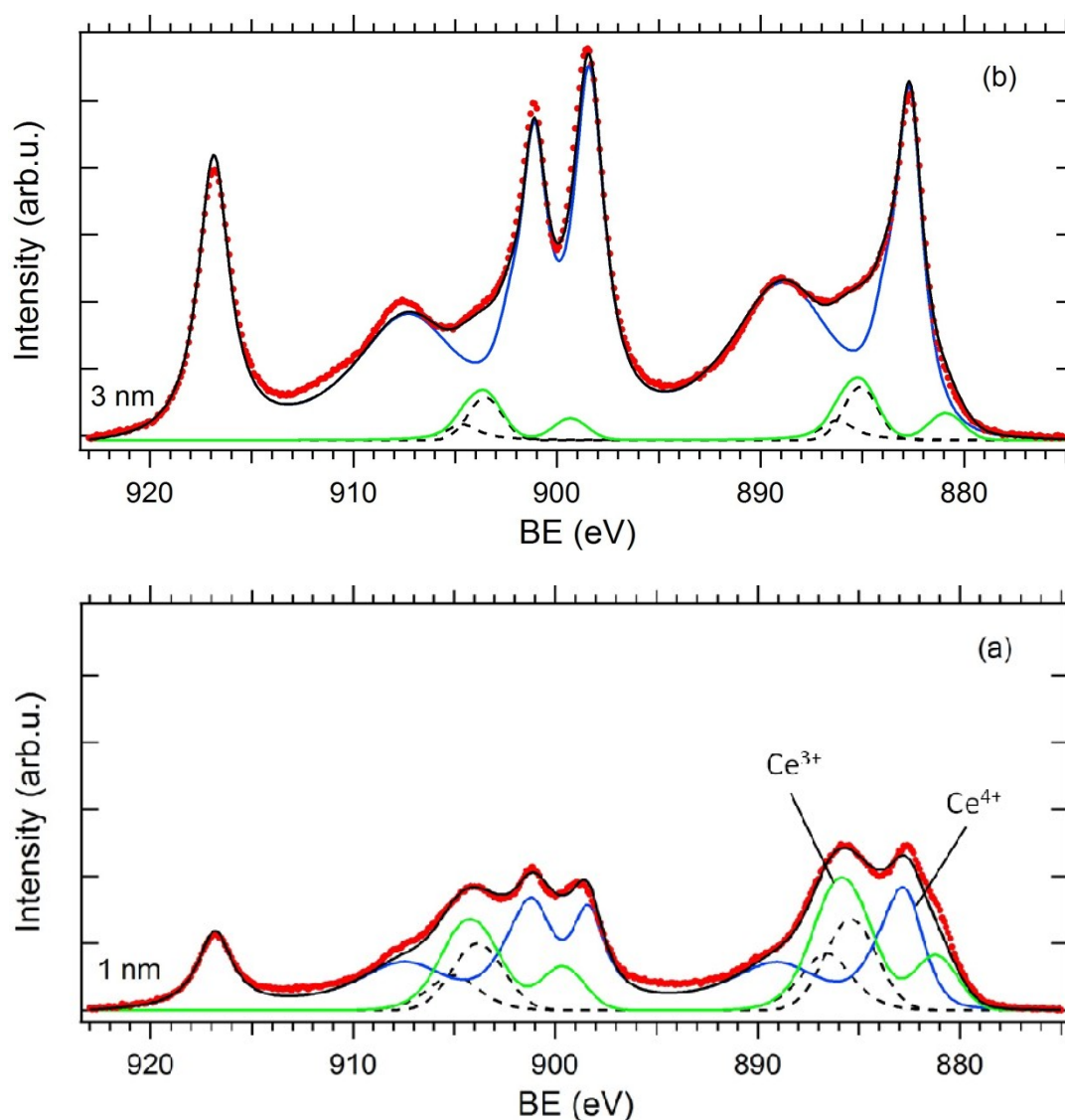


Fig. 5.4.6 HAXPES Ce 3d spectra of the 1 nm thick (a) and 3 nm thick (b) cerium oxide thin films grown on the n- SiO_2 substrate.

areas shown in *Table 5.4.2* can be compared with those of *Table 5.4.1*. We obtain Ce^{3+}/Ce^{4+} decrease from 0.07 \rightarrow to 0.08 (3 nm) and 0.6 \rightarrow to 0.36 (1 nm) for *n-SiO₂* relative to *b-SiO₂*, respectively. It shows clearly that in the case of the *Si* support covered by very thin native silicon oxide, cerium oxide reduction is quite stronger.

We can also identify, as in *Fig. 5.4.1* case, three different Ce^{3+} states f^1 (1), f^1 (2) and f^2 . Similarly to the *b-SiO₂* supported layers we suggest that the Ce^{3+} component f^1 (2) at the highest BE corresponds to ceria silicate located at the support - layer interface. This suggestion is supported by the fact that in the case of pure reduced cerium oxide such peak is not observed, as it was already mentioned above.

Because of similarity of the *Ce 3d Ce³⁺* spectra obtained for *n-SiO₂* and *b-SiO₂* substrates, it is reasonable to expect qualitatively same chemical composition of the CeO_x - SiO_2 interface. But it naturally requests appearance of the same oxygen chemical states in *O 1s* spectra. However, in *Fig. 5.3.2* the (O-Si-Ce)B state seems to be missing, (it can be also hidden by the huge $O-Si^{4+}$ peak making the exact fit impossible) which shows influence of the silicon oxide barrier on the cerium oxide film composition. In case of the thick oxide film (*b-SiO₂*) cerium silicate is produced by *Si* atoms released from SiO_2 while in the case of thin silicon oxide film (*n-SiO₂*) there is additional contribution of *Si* atoms provided by bulk *Si*.

Dependence of (O-Si-Ce)B peak intensity on the film thickness which we associated with silicate states produced by diffusion of the *Si* atoms from the *Si* bulk to the cerium oxide overlayer shows influence of the silicon oxide barrier on the cerium oxide film composition. In case of the thick oxide film (*b-SiO₂*) cerium silicate is produced by *Si* atoms released from SiO_2 while in case of thin silicon oxide film (*n-SiO₂*) there is additional contribution of *Si* atoms provided by bulk *Si*.

The conclusion of this study is that cerium oxide deposited on the *Si* wafer covered by thick and/or native SiO_2 reveals a strong interaction at the deposit-substrate interface. For both systems *Ce 3d* spectra exhibit new Ce^{3+} state (shifted by 1.5 eV to higher binding energy) which we associated to *Ce* atoms bound in cerium silicate. Cerium and silicon oxide also show partial reduction which has interfacial character. Formation of reduced interface can be explained by formation of complex mixture of mixed oxides which inhibits oxidation power of magnetron oxygen plasma during first stages of growth. This work shows clearly that in case of silicon oxide supported cerium based catalyst preparation the catalyst-substrate interaction

must be considered. Thermal oxidation of the silicon surface to SiO_2 makes the deposit - substrate interaction weaker, however surprisingly even generally stable silicon dioxide is reduced upon cerium oxide rf sputtering deposition by forming interfacial silicates and reduced ceria interface.

5.5. Pt-CeO₂ thin films prepared by PLD

The results presented in the previous chapters showed that the *Pt-CeO₂* catalyst films prepared by magnetron sputtering contain mainly ionic *Pt*. It was suggested that the ionic *Pt* can be an active state in PEMFC. It was also shown that the catalyst films grow porous on carbon substrates due to the plasma-substrate and film-substrate interactions. In order to understand better the mechanism of plasma assisted growth of the *Pt* doped ceria films PLD was used as a reference technique to prepare the *Pt-CeO₂* layers. Particularly we wanted to know whether the catalyst layers produced by PLD similarly to the magnetron sputtered films would grow porously on the carbon and contain ionic *Pt*.

The 20 nm thick *Pt-CeO₂* layers were prepared and investigated. The layers were simultaneously deposited on the reference silicon wafer pre-cleaned in the ultrasonic bath and on the carbon foil. The *Pt* mass concentration in the layers was 5% relative to a total amount of *CeO₂*. The deposition rate was around 1 nm/sec and was much higher than in case of magnetron sputtering where it was around 1 nm/min. The SEM images of the prepared PLD films are shown in *Fig. 5.5.1*. It can be seen that the both samples show almost the same smooth surface morphologies without any visible features. Similar surface morphology was seen in the case of the *Pt-CeO₂* thin film deposited by magnetron sputtering at normal angle deposition on the silicon wafer (see *Fig. 5.2.6(a)*). Such smooth surface morphology on both substrates is probably because of the high deposition rate leading to a short time exposition of the bare substrates to the plasma.

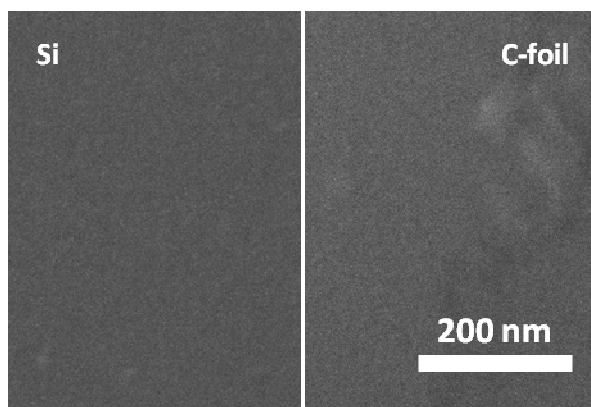


Figure 5.5.1. SEM images of the $Pt-CeO_2$ films deposited on the silicon wafer and the carbon foil.

Fig. 5.5.2 shows the $Ce\ 3d$ spectra of the $Pt-CeO_2$ film deposited on the *Si* and carbon foil substrate, respectively. The spectra are presented and fitted in the same way as in the previous sections. It can be seen that the high-resolution $Ce\ 3d$ core level HAXPES spectra in the both cases are almost the same and consist of three $3d_{5/2}-3d_{3/2}$ spin-orbit-split doublets $f^0(Ce^{4+})$, $f^1(Ce^{4+})$ and $f^2(Ce^{4+})$ that belong to stoichiometric CeO_2 and two doublets $f^1(Ce^{3+})$ and $f^2(Ce^{3+})$ of reduced ceria (dotted lines). The catalyst film is strongly reduced even in case of the reference silicon substrate. The non-porous character of the film indicates that the catalyst reduction is not due to the surface vacancies as it was in case of the porous magnetron sputtered films on the carbon substrates but probably due to overall non stoichiometric growth.

In *Fig. 5.5.3* are plotted corresponding $O\ 1s$ core level HAXPES spectra of the PLD layers. An intensive peak at 529.6 eV which corresponds to the oxygen from CeO_2 ($O-Ce^{4+}$) is well seen on the both spectra. As in case of the magnetron sputtered films a small peak at 530.5 eV can be assigned to the “ $Pt-Ce-O$ ” mixed oxide, while the peak appearing at 531.5 eV (marked $O-Ce^{3+}$) corresponds to hydroxyl groups OH that are formed by water dissociation on oxygen vacancies on the $Pt-CeO_2$ surface. It can be seen that intensity of the peak at 531.5 eV is relatively low supporting the suggestion about the formation of bulk vacancies that cannot be involved in such formation of OH groups.

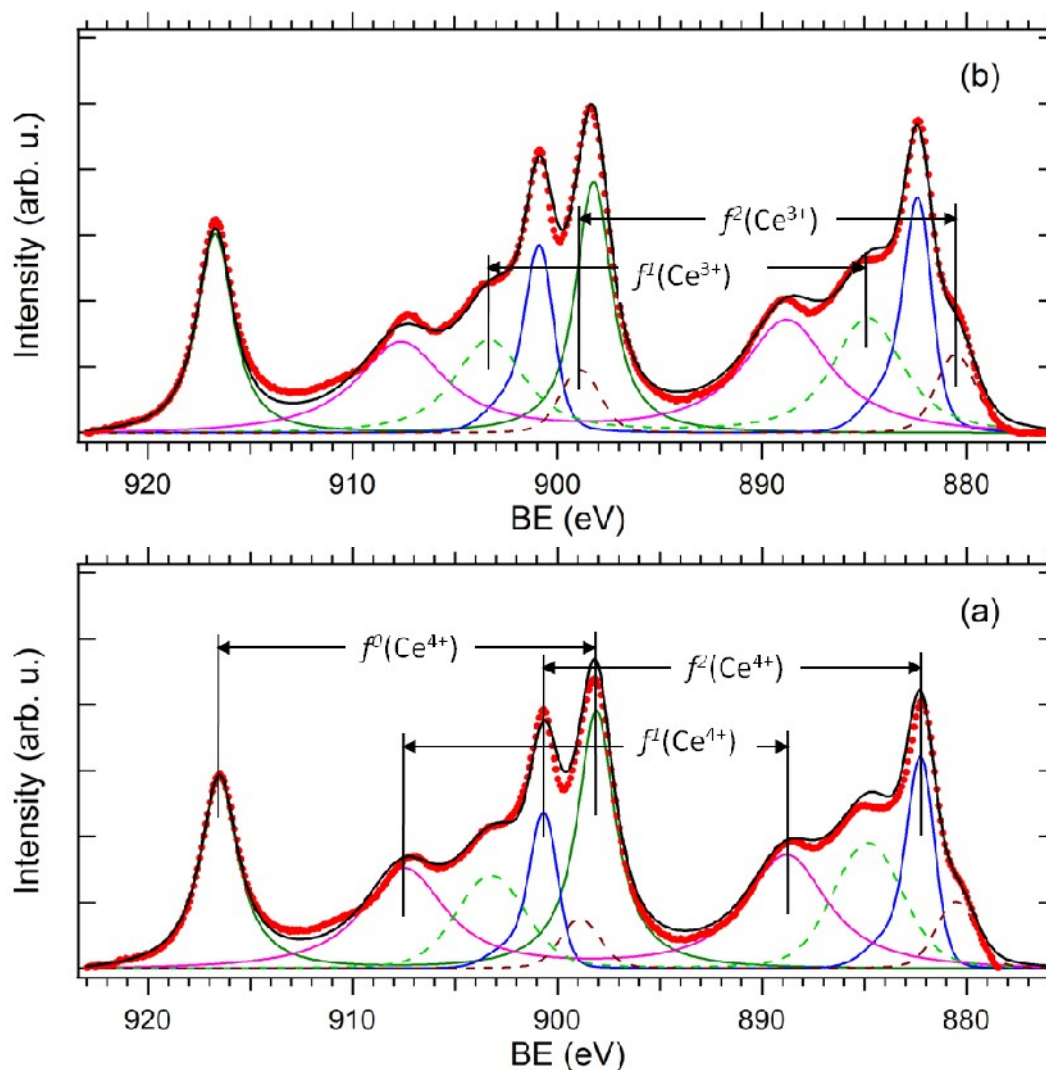


Figure 5.5.2. *Ce 3d* HAXPES spectra of the *Pt-CeO₂* films deposited on the silicon wafer (a) and the carbon foil (b).

In Fig. 5.5.4 the *Pt 4f* core level HAXPES spectra of the *Pt-CeO₂* film prepared by PLD on the reference silicon substrate and carbon foil are plotted. The both spectra exhibit two doublets at 71.1-74.4 eV and 72.6-75.9 eV. The first doublet corresponds to metallic *Pt*, while the second one according to its energy can be assigned to ionic platinum Pt^{2+} . It can be seen that the catalyst does not contain Pt^{4+} states.

According to presented results the *Pt-CeO₂* films prepared by PLD on both the reference silicon substrate and the carbon foil are non-porous, strongly reduced and contains mainly Pt^{2+} and no Pt^{4+} ions. Despite the fact that the films prepared by

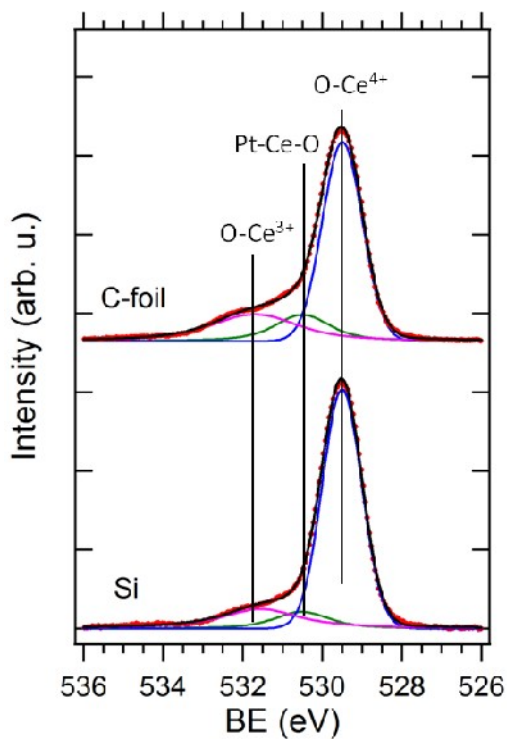


Figure 5.5.3. *O 1s* HAXPES spectra of the *Pt-CeO₂* films deposited on the silicon wafer (a) and the carbon foil (b).

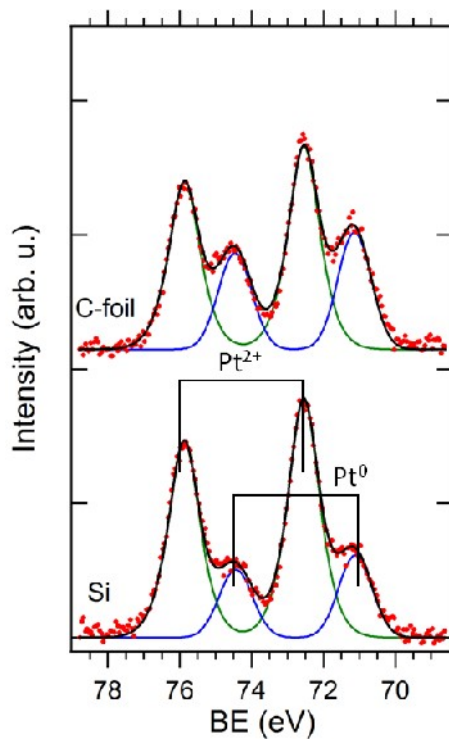


Figure 5.5.4. *Pt 4f* HAXPES spectra of the *Pt-CeO₂* films deposited on the silicon wafer (a) and the carbon foil (b).

PLD are non-porous even in case of the carbon substrate the presence of the ionic platinum makes them interesting for investigation in PEMFC. The testing of the PLD prepared *Pt-CeO₂* catalyst in PEMFC is the next possible step of its investigation. However, it should be noticed that a big disadvantage of PLD compared with magnetron sputtering is a small deposition area that makes impossible its wide use in industrial applications.

6. Summary and conclusions

This work began as a search for an explanation of the high activity of the magnetron sputtered $Pt-CeO_2$ thin film catalyst in PEMFC. At the beginning a relatively thick (around 30 nm) CeO_2 layers doped with two different concentrations of Pt were prepared and investigated on silicon substrates. It was found that in both cases Pt is uniformly dispersed inside the film mostly in Pt^{4+} ionic state forming the “ $Pt-Ce-O$ ” mixed oxide. The very small Pt^{2+} state seen in the spectra at lower BE was assigned to $Pt-Ce$ alloy accordingly to the TEM measurements. It is suggested that uniformly dispersed Pt ions increase reducibility of ceria improving its catalytic activity.

After investigation of the catalyst on the reference silicon substrate the $Pt-CeO_2$ thin films were prepared on different types of CNTs: commercial MWCNTs and CVD grown CNTs. It was expected that the catalyst would show the same properties as in case of the silicon substrate. To our surprise SEM revealed highly porous surface structure of the catalyst deposited on the CNTs unlike relatively smooth catalyst surface morphology on the silicon substrate. Photoelectron spectroscopy of the $Pt\ 4f$ core level showed that $Pt-CeO_2$ on the CNTs revealed around 60% platinum atoms in Pt^{2+} cationic state, 30% was in Pt^0 state (metallic), and only 10% in Pt^{4+} (in case of the Si wafer the catalyst exhibited 100% Pt atoms in Pt^{4+} state). The $Ce\ 3d$ HAXPES core level spectra revealed strong reduction of the catalyst due to deposition on the CNTs (around 30% Ce atoms were in Ce^{3+} state). The Pt^{2+} phase and ceria reduction were also observed in case when the catalyst was prepared in GLAD conditions on the Si wafer. Moreover the $Pt-CeO_2$ thin film prepared in GLAD conditions showed some porosity as well. It was concluded that different angles of deposition make influence on the morphology and stoichiometry of the film, especially on the CNTs due to round shape of the CNTs. By comparing

chemical composition of the $Pt-CeO_2$ deposited on the Si wafer at normal and glancing angle directions with that of the CNT supported film we concluded that the Ce^{3+} , Pt^{2+} -rich “ $Pt-Ce-O$ ” solid solution could be formed in the case of porous structures. The formation of Pt^{n+} states together with a porous character of the catalyst films were used to explain high activity of the $Pt-CeO_2$ catalyst in PEMFCs.

In order to exclude the deposition angle influence the catalyst was deposited on different flat carbon substrates. The $HOPG$, GC and pressed graphite foil were chosen as substrates. The $Pt-CeO_2$ catalyst thin films were deposited at normal deposition angle and investigated by means of PES and SEM. The main conclusions of this part are: 1) the catalyst sputtered on the carbon substrates shows the same highly porous surface morphology as in case of $CNTs$; 2) the porosity is enhanced in case of thinner films; 3) the porous films are partially reduced; 4) the Ce^{3+}/Ce and Pt^{2+}/Pt ratios show that the films are more reduced in deeper parts, i.e. closer to the interface. It was concluded that angle of deposition is not the key factor that influences morphology and stoichiometry of the catalyst when depositing on a carbon substrate. It was shown that the carbon surface can be etched by oxygen plasma generated by the magnetron that, in turn, leads to carbon surface roughening. The high active oxygen atoms and radicals sputtered from the CeO_2 target interact with the carbon surface forming CO or CO_2 molecules with further desorption from the surface. The oxygen reaction with carbon is also responsible for formation of oxygen deficient cerium oxide layer near the interface leading to the catalyst reduction.

After the comprehensive investigation of the high active $Pt-CeO_2$ thin film catalyst prepared on different substrates it was realized that the catalyst can be successfully exploit in the recently developing silicon based μFCs . The standard wet-process techniques for powder catalysts are incompatible with this μFC . Magnetron sputtering is technologically the most suitable method of preparation of such systems. It was important to investigate an interface between the catalyst and silicon substrate. Therefore in the fourth experiment, 1 and 3 nm thick CeO_2 layers deposited on the two different silicon substrates (silicon covered by thick and thin SiO_2 layers) were investigated by HAXPES. This study revealed a strong interaction at the deposit-substrate interface. In the case of both systems the $Ce 3d$ spectra exhibit new Ce^{3+} state shifted by 1.5 eV to higher binding energy, which was associated to Ce atoms bound in cerium silicate. It was shown that stoichiometry of

cerium oxide changes with deposited thickness leading to more stoichiometric oxide in the case of thicker layer. Formation of reduced interface is explained by formation of complex mixture of mixed oxides which inhibits oxidation power of magnetron oxygen plasma during first stages of growth. Thermal oxidation of the silicon surface to SiO_2 makes the deposit - substrate interaction weaker, however surprisingly even generally stable silicon dioxide is reduced upon cerium oxide RF sputtering deposition by forming interfacial silicates and reduced ceria interface. This study showed clearly that in the case of silicon oxide supported cerium based catalyst preparation the catalyst-substrate interaction must be considered.

In the last study PLD was used as a reference technique to prepare the *Pt-CeO₂* layers for better understanding of the mechanisms of plasma assisted growth of the *Pt* doped ceria films. It was shown that structure and stoichiometry of the catalyst film prepared by PLD does not depend on the type of substrates. The catalyst films on both the reference silicon substrate and carbon foil showed non-porous surface morphology and strong reduction. It was found that similarly to the magnetron sputtered *Pt-CeO₂* layers the PLD layers contain platinum mostly in Pt^{2+} state. However, PLD was considered to be less efficient in comparison with magnetron sputtering because its deposition area is a relatively small and not homogenous.

Bibliography

- [1] J. Spendelow, J. Marcinkoski, Record #12020: Fuel Cell System Cost - 2012, U.S. Department of Energy (Hydrogen Program), 2012.
- [2] M. Vaclavu, I. Matolinova, J. Myslivecek, R. Fiala, V. Matolin, *Journal of the Electrochemical Society* 156 (2009) B938-B942.
- [3] S. Motokawa, M. Mohamedi, T. Momma, S. Shoji, T. Osaka, *Electrochemistry Communications* 6 (2004) 562-565.
- [4] P.J. Kelly, R.D. Arnell, *Vacuum* 56 (2000) 159-172.
- [5] J.D. Morse, A.F. Jankowski, R.T. Graff, J.P. Hayes, *Journal of Vacuum Science & Technology a-Vacuum Surfaces and Films* 18 (2000) 2003-2005.
- [6] W.Z. Li, C.H. Liang, J.S. Qiu, W.J. Zhou, H.M. Han, Z.B. Wei, G.Q. Sun, Q. Xin, *Carbon* 40 (2002) 791-794.
- [7] Z.L. Liu, X.H. Lin, J.Y. Lee, W. Zhang, M. Han, L.M. Gan, *Langmuir* 18 (2002) 4054-4060.
- [8] C. Wang, M. Waje, X. Wang, J.M. Tang, R.C. Haddon, Y.S. Yan, *Nano Letters* 4 (2004) 345-348.
- [9] M. Watanabe, S. Motoo, *Denki Kagaku* 44 (1976) 602-607.
- [10] S.Y. Wang, D.S. Yu, L.M. Dai, *Journal of the American Chemical Society* 133 (2011) 5182-5185.
- [11] T. Frelink, W. Visscher, J.A.R. Vanveen, *Journal of Electroanalytical Chemistry* 382 (1995) 65-72.
- [12] N. Tian, Z.Y. Zhou, S.G. Sun, Y. Ding, Z.L. Wang, *Science* 316 (2007) 732-735.
- [13] V.R. Stamenkovic, B. Fowler, B.S. Mun, G.F. Wang, P.N. Ross, C.A. Lucas, N.M. Markovic, *Science* 315 (2007) 493-497.
- [14] T. Toda, H. Igarashi, H. Uchida, M. Watanabe, *Journal of the Electrochemical Society* 146 (1999) 3750-3756.

- [15] G.N. Vayssilov, Y. Lykhach, A. Migani, T. Staudt, G.P. Petrova, N. Tsud, T. Skala, A. Bruix, F. Illas, K.C. Prince, V. Matolin, K.M. Neyman, J. Libuda, *Nature Materials* 10 (2011) 310-315.
- [16] L. Jiang, L. Colmenares, Z. Jusys, G.Q. Sun, R.J. Behm, *Electrochimica Acta* 53 (2007) 377-389.
- [17] J. Shim, C.R. Lee, H.K. Lee, J.S. Lee, E.J. Cairns, *Journal of Power Sources* 102 (2001) 172-177.
- [18] N. Witkowski, F. Bertran, T. Gourieux, B. Kierren, D. Malterre, G. Panaccione, *Physical Review B* 56 (1997) 12054-12057.
- [19] K.C. Taylor, *Catalysis Reviews-Science and Engineering* 35 (1993) 457-481.
- [20] M. Ozawa, M. Kimura, H. Sobukawa, K. Yaokota, *Toyota Technical Review* 27 (1992) 43.
- [21] I. Manuel, C. Thomas, H. Colas, N. Matthes, G. Djega-Mariadassou, *Topics in Catalysis* 30-1 (2004) 311-317.
- [22] D. Pierre, W.L. Deng, M. Flytzani-Stephanopoulos, *Topics in Catalysis* 46 (2007) 363-373.
- [23] X.L. Tang, B.C. Zhang, Y. Li, Y. Xu, Q. Xin, W.J. Shen, *Journal of Molecular Catalysis a-Chemical* 235 (2005) 122-129.
- [24] S. Imamura, T. Hagashihara, Y. Saito, H. Aritani, H. Kanai, Y. Matsumura, N. Tsuda, *Catalysis Today* 50 (1999) 369-380.
- [25] T. Bunluesin, R.J. Gorte, G.W. Graham, *Applied Catalysis B-Environmental* 15 (1998) 107-114.
- [26] C.W. Xu, R. Zeng, P.K. Shen, Z.D. Wei, *Electrochimica Acta* 51 (2005) 1031-1035.
- [27] P. Bera, K.C. Patil, V. Jayaram, G.N. Subbanna, M.S. Hegde, *Journal of Catalysis* 196 (2000) 293-301.
- [28] C.L. Campos, C. Roldan, M. Aponte, Y. Ishikawa, C.R. Cabrera, *Journal of Electroanalytical Chemistry* 581 (2005) 206-215.
- [29] M. Takahashi, T. Mori, F. Ye, A. Vinu, H. Kobayashi, J. Drennan, *Journal of the American Ceramic Society* 90 (2007) 1291-1294.
- [30] D.H. Lim, W.D. Lee, D.H. Choi, H.I. Lee, *Applied Catalysis B-Environmental* 94 (2010) 85-96.

- [31] R. Fiala, I. Khalakhan, I. Matolinova, M. Vaclavu, M. Vorokhta, Z. Sofer, S. Huber, V. Potin, V. Matolin, *Journal of Nanoscience and Nanotechnology* 11 (2011) 5062-5067.
- [32] T. Mori, D.R. Ou, J. Zou, J. Drennan, *Progress in Natural Science-Materials International* 22 (2012) 561-571.
- [33] P.J. Hay, R.L. Martin, J. Uddin, G.E. Scuseria, *Journal of Chemical Physics* 125 (2006) 034712 (1-8).
- [34] H. Ogasawara, A. Kotani, K. Okada, B.T. Thole, *Physical Review B* 43 (1991) 854-859.
- [35] A. Kotani, H. Ogasawara, *Journal of Electron Spectroscopy and Related Phenomena* 60 (1992) 257-299.
- [36] T.K. Sham, R.A. Gordon, S.M. Heald, *Physical Review B* 72 (2005) 034712 (034711-034716).
- [37] T. Skala, F. Sutara, K.C. Prince, V. Matolin, *Journal of Electron Spectroscopy and Related Phenomena* 169 (2009) 20-25.
- [38] V. Matolin, M. Cabala, V. Chab, I. Matolinova, K.C. Prince, M. Skoda, F. Sutara, T. Skala, K. Veltruska, *Surface and Interface Analysis* 40 (2008) 225-230.
- [39] W.D. Sproul, *Opportunities for Innovation: Advanced Surface Engineering*, Technomic Publ., 1994.
- [40] D.B. Chrisey, G.K. Hubler, *Pulsed Laser Deposition of Thin Films*, John Wiley & Sons, New York, 1994.
- [41] H.M. Christen, G. Eres, *Journal of Physics-Condensed Matter* 20 (2008) 1-16.
- [42] S. Hufner, *Photoelectron Spectroscopy: Principles and Applications*, Springer, 2003.
- [43] D. Briggs, in: D. Briggs, J.T. Grant (Eds.), *Surface Analysis by Auger and X-ray Photoelectron Spectroscopy*, IM Publications and SurfaceSpectra Limited, Chichester, 2003, pp. 31-56.
- [44] D. Briggs, M.P. Sea, *Practical Surface Analysis*, John Willey & sons, New York, 1990.
- [45] D.H. Tombouliau, P.L. Hartman, *Physical Review* 102 (1956) 1423-1447.
- [46] R.Z. Bachrach, *Synchrotron Radiation Research*, Plenum Press, New York, 1992.
- [47] www.vgscienta.com, Official website of VG Scienta.

- [48] <http://www.kolibrik.net>, Official website.
- [49] M.B. Watkins, A.S. Foster, A.L. Shluger, *Journal of Physical Chemistry C* 111 (2007) 15337-15341.
- [50] M.A. Henderson, C.L. Perkins, M.H. Engelhard, S. Thevuthasan, C.H.F. Peden, *Surface Science* 526 (2003) 1-18.
- [51] S. Gritschneider, M. Reichling, *Nanotechnology* 18 (2007) 1-6.
- [52] U. Berner, K.D. Schierbaum, *Physical Review B* 65 (2002) 235404 (1-10).
- [53] K. Andersson, A. Gomez, C. Glover, D. Nordlund, H. Ostrom, T. Schiros, O. Takahashi, H. Ogasawara, L.G.M. Pettersson, A. Nilsson, *Surface Science* 585 (2005) L183-L189.
- [54] T. Schiros, K.J. Andersson, L.G.M. Pettersson, A. Nilsson, H. Ogasawara, *Journal of Electron Spectroscopy and Related Phenomena* 177 (2010) 85-98.
- [55] S. Yamamoto, H. Bluhm, K. Andersson, G. Ketteler, H. Ogasawara, M. Salmeron, A. Nilsson, *Journal of Physics-Condensed Matter* 20 (2008) 1-14.
- [56] L. Kundakovic, D.R. Mullins, S.H. Overbury, *Surface Science* 457 (2000) 51-62.
- [57] M. Hecq, A. Hecq, J.P. Delrue, T. Robert, *Journal of the Less-Common Metals* 64 (1979) P25-P37.
- [58] B. Stéphanie, A. Cacucci, V. Potin, I. Matolinova, M. Vorokhta, V. Matolin, *Surface and Coating Technology*, DOI: 10.1016/j.surfcoat.2012.08.036 (2012).
- [59] J. Tang, J.M. Lawrence, J.C. Hemminger, *Physical Review B* 48 (1993) 15342-15352.
- [60] S. Bernal, J.J. Calvino, M.A. Cauqui, J.M. Gatica, C.L. Cartes, J.A.P. Omil, J.M. Pintado, *Catalysis Today* 77 (2003) 385-406.
- [61] Z.X. Yang, G.X. Luo, Z.S. Lu, T.K. Woo, K. Hermansson, *Journal of Physics-Condensed Matter* 20 (2008) 035210 (1-7).
- [62] L. Osterlund, S. Kielbassa, C. Werdinius, B. Kasemo, *Journal of Catalysis* 215 (2003) 94-107.
- [63] V. Matolin, J. Libra, M. Skoda, N. Tsud, K.C. Prince, T. Skala, *Surface Science* 603 (2009) 1087-1092.
- [64] K. Robbie, M.J. Brett, *Journal of Vacuum Science & Technology a-Vacuum Surfaces and Films* 15 (1997) 1460-1465.
- [65] K.M. Beck, M. Henyk, C.M. Wang, P.E. Trevisanutto, P.V. Sushko, W.P. Hess, A.L. Shluger, *Physical Review B* 74 (2006) 045404 (1-5).

- [66] M. Henyk, K.M. Beck, M.H. Engelhard, A.G. Joly, W.P. Hess, J.T. Dickinson, *Surface Science* 593 (2005) 242-247.
- [67] J. Kim, Z. Dohnalek, B.D. Kay, *Surface Science* 586 (2005) 137-145.
- [68] P. Bera, K.R. Priolkar, A. Gayen, P.R. Sarode, M.S. Hegde, S. Emura, R. Kumashiro, V. Jayaram, G.N. Subbanna, *Chemistry of Materials* 15 (2003) 2049-2060.
- [69] M. Hatanaka, N. Takahashi, T. Tanabe, Y. Nagai, A. Suda, H. Shinjoh, *Journal of Catalysis* 266 (2009) 182-190.
- [70] K. Kinoshita, *Carbon Materials. Carbon - Electrochemical and Physicochemical properties*, Wiley, New York, 1988.
- [71] P.J. Hall, M. Mirzaeian, S.I. Fletcher, F.B. Sillars, A.J.R. Rennie, G.O. Shitta-Bey, G. Wilson, A. Cruden, R. Carter, *Energy & Environmental Science* 3 (2010) 1238-1251.
- [72] R.L. McCreery, *Chemical Reviews* 108 (2008) 2646-2687.
- [73] G. Lota, K. Fic, E. Frackowiak, *Energy & Environmental Science* 4 (2011) 1592-1605.
- [74] R.P.U. Karunasiri, R. Bruinsma, J. Rudnick, *Physical Review Letters* 62 (1989) 788-791.
- [75] G.S. Bales, A. Zangwill, *Journal of Vacuum Science & Technology a-Vacuum Surfaces and Films* 9 (1991) 145-149.
- [76] R. Messier, *Journal of Vacuum Science & Technology a-Vacuum Surfaces and Films* 4 (1986) 490-495.
- [77] P.O. Lopez-Montesinos, N. Yossakda, A. Schmidt, F.R. Brushett, W.E. Pelton, P.J.A. Kenis, *Journal of Power Sources* 196 (2011) 4638-4645.
- [78] F. Chen, M.-H. Chang, H.-Y. Lin, *Journal of Power Sources* 178 (2008) 125-131.
- [79] S. Tanuma, C.J. Powell, D.R. Penn, *Surface and Interface Analysis* 21 (1994) 165-176.
- [80] D. Pacile, M. Papagno, T. Skala, V. Matolin, T. Sainsbury, T. Ikuno, D. Okawa, A. Zettl, K.C. Prince, *Journal of Physics-Condensed Matter* 22 (2010) 295301 (295301-295304).
- [81] S. Ogawa, A. Yoshigoe, S. Ishidzuka, Y. Teraoka, Y. Takakuwa, *Japanese Journal of Applied Physics Part 1-Regular Papers Brief Communications & Review Papers* 46 (2007) 3244-3254.

- [82] J.R. Engstrom, D.J. Bonser, T. Engel, *Surface Science* 268 (1992) 238-264.
- [83] J. Finster, D. Schulze, F. Bechstedt, A. Meisel, *Surface Science* 152 (1985) 1063-1070.
- [84] S. Zec, S. Boskovic, *Journal of Materials Science* 39 (2004) 5283-5286.
- [85] H.A.M. Van Hal, H.T. Hintzen, *Journal of Alloys and Compounds* 179 (1992) 77-85.
- [86] F.U. Hillebrecht, M. Ronay, D. Rieger, F.J. Himpsel, *Physical Review B* 34 (1986) 5377-5380.

List of Tables

<i>Table 5.1.1.</i> The $f^0(\text{Ce}^{4+})/f^1(\text{Ce}^{4+})$ and $f^0(\text{Ce}^{4+})/f^2(\text{Ce}^{4+})$ ratios of the catalyst doped with different concentration of Pt.....	31
<i>Table 5.2.1.</i> Ce^{3+}/Ce , Pt^{2+}/Pt and Pt^0/Pt concentration ratios for samples prepared on different types of the support.....	47
<i>Table 5.3.1.</i> Ce^{3+}/Ce , Pt^{2+}/Pt and Pt^0/Pt concentration ratios for samples prepared on different types of the support.....	53
<i>Table 5.3.2.</i> Ce^{3+}/Ce and Pt^{2+}/Pt concentration ratios for 30 nm Pt-CeO ₂ film deposited on C-foil that was calculated using HAXPES and XPS spectra.....	56
<i>Table 5.4.1.</i> Areas of the Ce^{4+} and Ce^{3+} Ce 3d peaks and of the O-Si O 1s peaks measured from 1 and 3 nm thick CeO ₂ film on the b-SiO ₂ substrate.....	61
<i>Table 5.4.2.</i> Areas of the Ce^{4+} and Ce^{3+} Ce 3d peaks and O-Si ⁴⁺ and O-Si-Ce O 1s peaks measured on 1 and 3 nm thick CeO ₂ films supported by the n-SiO ₂ substrate.....	66

List of Abbreviations

AES	Auger Electron Spectroscopy
AFM	Atomic Force Microscopy
BE	Binding Energy
BSE	Backscattered Electron
CCD	Charge-Coupled Device
CNT	Carbon Nanotube
CVD	Chemical Vapor Deposition
DC	Direct Current
DMFC	Direct Methanol Fuel Cell
EDXS	Energy Dispersive X-ray Spectroscopy
ESCA	Electron Spectroscopy for Chemical Analysis
FC	Fuel Cell
GC	Glassy Carbon
GDL	Gas Diffusion Layer
GLAD	Glancing Angle Deposition
HAXPES	Hard X-ray Photoelectron Spectroscopy
HOPG	Highly Ordered Pyrolytic Graphite
HOR	Hydrogen Oxidation Reaction
HRTEM	High Resolution Transmission Electron Microscopy
MEA	Membrane Electrode Assembly
MCP	Multi-Channel Plate
MSI	Metal-Substrate Interaction
MWCNT	Multiwall Carbon Nanotube
ND	Normal Deposition
ORR	Oxygen Reduction Reaction
OSC	Oxygen Storage Capacity

PEM	Proton Electrolyte Membrane
PEMFC	Proton Electrolyte Membrane Fuel Cell
PES	Photoelectron Spectroscopy
PVP	Polyvinylpyrrolidon
RF	Radio Frequency
SE	Secondary Electron
SEM	Scanning Electron Microscopy
SRPES	Synchrotron Radiation Photoelectron Spectroscopy
TEM	Transmission Electron Microscopy
UHV	Ultra High Vacuum
XPS	X-ray Photoelectron Spectroscopy